

The JRA-25 Reanalysis

**Kazutoshi ONOGI¹, Junichi TSUTSUI², Hiroshi KOIDE¹, Masami SAKAMOTO¹,
Shinya KOBAYASHI¹, Hiroaki HATSUSHIKA²⁽⁶⁾, Takanori MATSUMOTO¹⁽⁴⁾,
Nobuo YAMAZAKI³⁽⁵⁾, Hirotaka KAMAHORI³⁽¹⁾, Kiyotoshi TAKAHASHI³,
Shinji KADOKURA², Koji WADA², Koji KATO⁴, Ryo OYAMA⁴, Tomoaki OSE¹⁽³⁾,
Nobutaka MANNOJI¹, and Ryusuke TAIRA⁵**

¹Japan Meteorological Agency, Tokyo, Japan

²Central Research Institute of Electric Power Industry, Abiko, Japan

³Meteorological Research Institute, Japan Meteorological Agency, Tsukuba, Japan

⁴Meteorological Satellite Center, Japan Meteorological Agency, Kiyose, Japan

⁵Meteorological College, Japan Meteorological Agency, Kashiwa, Japan

⁶Toyama Prefectural Environmental Science Research Center, Imizu, Japan

(Manuscript received 8 June 2006, in final form 12 February 2007)

Abstract

A long-term global atmospheric reanalysis, named “Japanese 25-year Reanalysis (JRA-25)” was completed using the Japan Meteorological Agency (JMA) numerical assimilation and forecast system. The analysis covers the period from 1979 to 2004. This is the first long-term reanalysis undertaken in Asia. JMA’s latest numerical assimilation system, and specially collected observational data, were used to generate a consistent and high-quality reanalysis dataset designed for climate research and operational monitoring and forecasts. One of the many purposes of JRA-25 is to enhance the analysis to a high quality in the Asian region.

Six-hourly data assimilation cycles were performed, producing 6-hourly atmospheric analysis and forecast fields of various physical variables. The global model used in JRA-25 has a spectral resolution of T106 (equivalent to a horizontal grid size of around 120 km) and 40 vertical layers with the top level at 0.4 hPa. In addition to conventional surface and upper air observations, atmospheric motion vector (AMV) wind retrieved from geostationary satellites, brightness temperature from TIROS Operational Vertical Sounder (TOVS), precipitable water retrieved from orbital satellite microwave radiometer radiance and other satellite data are assimilated with three-dimensional variational method (3D-Var). JMA produced daily sea surface temperature (SST), sea ice and three-dimensional ozone profiles for JRA-25. A new quality control method for TOVS data was developed and applied in advance.

Many advantages have been found in the JRA-25 reanalysis. Predicted 6-hour global total precipitation distribution and amount are well reproduced both in space and time. The performance of the long time series of the global precipitation is the best among the other reanalyses, with few unrealistic variations from degraded satellite data contaminated by volcanic eruptions. Secondly, JRA-25 is the first reanalysis to assimilate wind profiles around tropical cyclones reconstructed from historical best track information; tropical cyclones were analyzed properly in all the global regions. Additionally, low-level cloud along the subtropical western coast of continents is well simulated and snow depth analysis is also of a good quality. The article also covers material which requires attention when using JRA-25.

Corresponding author: Kazutoshi Onogi, Japan Meteorological Agency, 1-3-4 Otemachi, Chiyoda-ku, Tokyo 100-8122, Japan.

E-mail: konogi@naps.kishou.go.jp

Present affiliations are a number in parentheses.

© 2007, Meteorological Society of Japan

1. Introduction

Global daily atmospheric analysis of more than several past decades are needed for climate research and operations as a basic dataset. Bengtsson and Shukla (1988) and Trenberth and Olson (1988) proposed “Long term Reanalysis” to satisfy this requirement. This need requires producing a consistent and high-quality historical analysis dataset spanning the past several decades using the latest data assimilation system, numerical prediction models, and a high-performance supercomputer, preferably unaltered during the execution of the analysis.

Following the proposal of reanalysis, some numerical prediction centers carried out their reanalysis projects as shown in Table 1. National Center for Environmental Prediction (NCEP) and National Center for Atmospheric Research (NCAR) completed the first reanalysis R1 covering the period 1948 to present with a resolution of T62 (Kalnay et al. 1996; Kistler et al. 2001). European Centre for Medium Range Weather Forecasts (ECMWF) completed the ERA-15 reanalysis from 1979 to 1993 with a higher resolution of T106 (Gibson et al. 1997). Data Assimilation Office (DAO) of National Aeronautics and Space Ad-

ministration (NASA), currently Global Modeling and Assimilation Office (GMAO) of NASA, also completed the GEOS1 reanalysis (Schubert et al. 1993) covering the period of about 16 years.

ECMWF completed their second reanalysis, ERA-40, with greatly improved system from ERA-15, using a higher resolution of TL159L60, covering 45 years from September 1957 to August 2002 (Uppala et al. 2004; Uppala et al. 2005). NCEP and Department of Energy (DOE) completed their NCEP/DOE R2 reanalysis using a corrected data assimilation system of R1 (Kanamitsu et al. 2002). Both R1 and R2 have been continued as Climate Data Assimilation System (CDAS).

While reanalysis datasets were produced with advanced data assimilation systems and worldwide observational data inclusive satellite data, many differences and problems are found (Koide et al. 2000). In particular, location and geometry of the Inter-Tropical Convergence Zone (ITCZ), and distribution and time evolution of divergence in the tropics are different among the reanalyses (Newman et al. 2000). In the latest ECMWF reanalysis ERA-40, in which satellite data were maximally assimilated, excess precipitation appeared in the tropics, which seemed to be caused by problems

Table 1. List of available reanalyses.
Currently available reanalyses are listed together with their specifications.

Name	Organization	Reanalysis period	Resolution	Data assimilation method	
JRA-25	JMA/CRIEPI	1979–2004	T106 L40	3D-Var	completed in Mar. 2006 continued as JCDAS
ERA-15	ECMWF	1979–1993	T106 L31	3D-OI	completed in 1996
ERA-40	ECMWF	1957.9–2002.8	TL159 L60	3D-Var	completed in 2003
NCEP/NCAR R1	NCEP/NCAR	1948–present	T62 L28	3D-Var	operated as CDAS
NCEP/DOE R2 (NCEP-DOE AMIP-II reanalysis)	NCEP/DOE	1979–present	T62 L28	3D-Var	operated as CDAS
GEOS1	NASA DAO	1980–1995	2 × 2.5 L20	3D-OI + IAU	

T and TL mean wave truncation number, L means number of vertical level.

T106 and TL159 are equivalent to grid interval 120 km, T62 is to 200 km

in the assimilation of the satellite data (Bengtsson et al. 2004a; Bengtsson et al. 2004b; Hagemann et al. 2005).

To ameliorate these problems and contribute to climate research and the operational seasonal prediction in Japan and Asia, since 2001 JMA and Central Research Institute of Electric Power Industry (CRIEPI) have been jointly conducting a Japanese 25-year Reanalysis (JRA-25). It covers 26 years from 1979 to 2004. Onogi et al. (2005) reported briefly the JRA-25 progress in an interim report in the first half of 2005.

In this paper, the data assimilation system, features of the reanalysis product, and matters requiring further attention are described.

JRA-25 placed significant emphasis on the following;

- Assimilate data unused in the other reanalyses to produce higher quality analyses, particularly in Eastern Asia and the tropics.
- Produce a consistent analysis dataset which can be used as a basis for JMA's operational climate monitoring services and for validation of the development of seasonal forecast models.
- Enhance the data assimilation research activities within Japan with the collaboration of researchers.

In 1979 the First Global Atmospheric Research Program (GARP) Global Experiment (FGGE) project was conducted. Since then, the radiosonde observational network was systematically improved. Furthermore, sounding data from TOVS onboard orbital satellites and AMV data retrieved from geostationary satellites have become available. Because the quality of observational data was improved in and after 1979 and data sparse ocean areas were filled with satellite data, a consistent reanalysis dataset can be properly produced. Thus, year 1979 was chosen as a starting year of JRA-25.

JRA-25 reanalysis is a basic meteorological grid point dataset with uniform resolution of 120 km in the horizontal and from the surface to about 50 km in the vertical. It provides over 100 kinds of physical atmospheric variables such as temperature, pressure, wind, humidity, cloud amount, ozone, radiation, precipitation, snowfall, marine variables such as SST and sea ice coverage; terrestrial variables such as

land surface temperature, snow depth, evaporation, soil moisture, runoff, and others. Observational data used in JRA-25 were supplied by ECMWF, NCEP, NCAR, National Climate Data Center (NCDC) and many other overseas numerical prediction centers and institutes.

The JRA-25 system was transitioned to the JMA Climate Data Assimilation System (JCDAS) to produce operational analysis products for near real time climate monitoring.

In Section 2, an overview of each type of observational data assimilated in JRA-25 is given. In Section 3, the JRA-25 data assimilation and forecast system are introduced. In Section 4, various aspects of the performance of JRA-25 reanalysis is made in comparison with other reanalyses. Unrealistic changes and discontinuities in time series due to changes in historical observation are discussed. In Section 5, features and findings of JRA-25 are summarized and the future direction for reanalysis is proposed.

2. Observational data and quality control

The list of observational data used in JRA-25 is shown in Fig. 1 together with data source and their available period. Since data in JMA archives were not sufficient for conducting JRA-25 reanalysis, additional observational data were acquired from overseas numerical weather centers. The major data source is ERA-40 observational data supplied by ECMWF as used in their ERA-40 reanalysis, which contains conventional data, wind data retrieved from geostationary satellites, and level 1c TOVS and ATOVS radiance temperature data. ERA-40 observational data also contains Meteorological Satellite (METEOSAT)-2 AMV data reprocessed by EUMETSAT. Special Sensor of Microwave Imager (SSM/I) radiance temperature data were supplied by NCDC. Wind profile retrievals surrounding tropical cyclones (hereafter TCR) data were supplied by Dr. M. Fiorino of the Program for Climate Model and Diagnostics Intercomparison/Laurence Livermore National Laboratory (PCMDI/LLNL) (currently at the National Hurricane Center (NHC), Miami). The JMA Meteorological Satellite Center (MSC) reprocessed Geostationary Meteorological Satellite (GMS) AMV data and JMA Meteorological Research Institute (MRI) digitized

Name	Data Supplier	Available Period	Assimilated Period	Assimilated Period (Year)				
				1980	1985	1990	1995	2000
Conventional (JMA archives)	JMA	1979.01–	1984.05–2004.12					
Conventional (ERA-40 observation)	ECMWF	1957.09–2002.08	1979.01–2002.08					
Digitized Chinese Snow	MRI/JMA	1979.01–2003.12	1979.01–2003.12					
TCR wind data	Dr.M. Fiorino	1979.01–	1979.01–2004.12					
Indonesia radiosonde data	Dr.M. Yamanaka	1991.11–1999.05	1991.11–1999.05					
GAME enhanced observation	JMA	1998.04–1998.10	1998.04–1998.10					
wind profiler	JMA	1993.07–	1993.07–2004.12					
operational CMV/AMV (not GMS)	JMA	1979.01–	1979.01–2004.12					
operational CMV/AMV (GMS)	JMA	1979.01–	1979.01–1987.02, 1994.01–1996.12, 2002.02–2002.09, 2003.05–2004.12(GOES9)					
GMS reprocessed AMV	MSC/JMA	1987.03–2003.05	1987.03–1993.12, 1997.01–2002.01, 2002.10–2003.05					
METEOSAT reprocessed AMV	EUMETSAT	1982.05–1988.05	1982.05–1988.05					
TOVS 1c (ERA-40 observation)	ECMWF	1979.01–2002.08	1979.01–1998.10					
ATOVS 1c (ERA-40 observation and JMA archives)	ECMWF and JMA	1998.11–	1998.11–2004.12					
SSM/I PW, snow coverage	NCDC	1987.06.25–	1987.06–2004.12					
ERS-1,2	JMA	1995.04.24–2001.01.17	1995.4.24–2001.1.17					
QuikSCAT	JMA	2001.09.30–	2001.09.30–2004.12					
MODIS polar wind	JMA	2004.06.09–	2004.06.09–2004.12					

Fig. 1. Observational data used in JRA-25.

Observational data used in JRA-25 are shown, as well as data supplier, available periods, and assimilated periods. A bold large font indicates data supplied by JMA for JRA-25, or data that have not been used previously in a reanalysis.

Chinese daily snow depth data from “Monthly Surface Meteorological Data in China.” For those observational data, the file format was unified and preliminary quality control was performed to utilize the data consistently for long reanalysis years. Subsequently, the major observational data are described individually.

2.1 Conventional data

a. Conventional data

In this paper, conventional data is defined as directly observed data such as land and marine surface, upper air, and aviation data which are neither satellite observations nor remote sensing data from the ground. Meteorological variables such as pressure, temperature, wind, and humidity are observed directly with generally high quality. Conventional data are fundamental observations often used as reference data

for validating the quality of satellite data and as a basis for their bias correction. Many conventional data are distributed over land. Marine data are distributed unevenly along the ship tracks, mostly in the northern hemisphere. Many drifting buoys are put into the areas of the tropical and southern hemisphere ocean where marine data are scarce. Upper air observations in the ocean from ships are limited both in number and distribution. Aviation data can be classified between in-flight data and data at the time of take off and landing. In global data assimilation, in-flight aviation data are mainly assimilated. Aviation data are distributed unevenly along their tracks similar to the ship data.

The ERA-40 observational dataset contains not only their original merged dataset between ECMWF and NCEP/NCAR archives, but also

conventional data supplied additionally from NCAR and NCEP. It has the highest amount of historical observational data available at present. Separate JMA archives are also available throughout the period of the JRA-25 reanalysis years and the data from May 1984, which were in time for JRA-25 production, were also added. The original NCEP/NCAR archives were also supplied but not used, because most of data in their archives were included in the ERA-40 observational data. The file format of the archives had been converted JMA unified format in parallel with the production of the JRA-25 project.

In addition, for the limited period and domain, upper air observation in Indonesia from 1991 to 1999 (Okamoto et al. 2003) and enhanced observational data of Global Energy and Water Cycle Experiment (GEWEX) Asia Monsoon Experiment (GAME) for the summer of 1998 were available and used. While part of the GEWEX dataset was also reported via the Global Telecommunication System (GTS), the original data can supplement the online data with higher resolution and frequency.

b. Wind profile retrievals surrounding tropical cyclones (TCR)

In the JMA's operational global analysis, idealized tropical cyclone (hereafter TC) structure, called "typhoon bogus," is embedded into a first guess field for the analysis of typhoons and tropical depressions in the Western North Pacific (JMA 2002). Instead of this procedure, wind speed profiles around tropical cyclones were reconstructed based on the historical best track and tropical cyclone intensity information and then assimilated into JRA-25. While both methods were somewhat artificial, the latter approach is more natural because the reconstructed data are used together with other real observations. This approach was applied not only for the Western North Pacific but also for all the tropical storms (wind speed over 17.2 m s^{-1}). JRA-25 is the first reanalysis using this method; other reanalyses have never applied special treatment of TCs. The method was developed by Fiorino (2002), who reconstructed the TC wind data independently and provided it to JRA-25. Reconstructed wind speed fields around TCs are computed from 6-hourly positions, intensity, and speed of motion

based on best track data (Neumann 1993) with some assumptions. The data consist of winds on standard pressure levels from 1000 hPa to 400 hPa at the center and at 2 degrees away from the center of TCs in four cardinal directions. In the data assimilation, the data are treated as PILOT observations.

c. Chinese snow data

Chinese daily snow depth data in "Monthly Surface Meteorological Data in China" published by the Chinese Meteorological Administration were digitized and assimilated into the JRA-25 snow depth analysis. While snow depth data are exchanged internationally via the GTS as a part of SYNOP reports, very few Chinese snow depth data were received. Consequently the digitized data were used first in the reanalysis. Area of sparse snow depth data over China were then filled with the Chinese data, which contributed to improved snow depth analysis, as will be described in 4.10.

2.2 Satellite and remote sensing data

a. TOVS and ATOVS

TOVS are a set of sensors aimed at observing vertical profiles of temperature, moisture, and other radiation and surface variables (Werbowski 1981). The TOVS observations had been available from 9 satellites: TIROS-N to NOAA-14. TOVS consists of 3 cross-track instruments: High resolution Infrared Radiation Sounder-2 (HIRS/2), Microwave Sounding Unit (MSU), and Stratospheric Sounding Unit (SSU). HIRS/2 has 20 channels and provides vertical profiles of temperature and moisture, ranging from near surface to the lower stratosphere. Surface skin temperature, ozone concentration, and solar albedo can be observed. Four channels of MSU aimed to observe surface emissivity and temperature profiles up to the tropopause. Three channels of SSU aimed to observe the thermal profile of the upper stratosphere.

Advanced TOVS (ATOVS) has been on board after the NOAA 15 satellite, replacing the former TOVS. ATOVS consists of an infrared radiance sounder HIRS/3 and a microwave sounder Advanced MSU (AMSU). While HIRS/3 remains a partial improvement from HIRS/2, AMSU was a substantial improvement from MSU and consists of AMSU-A aimed to observe vertical temperature profiles and AMSU-B aimed to observe vertical moisture profiles.

b. SSM/I precipitable water

Microwave radiometer sensor Special Sensor of Microwave Imager (SSM/I) on board the Defense Meteorological Satellite Program (DMSP) satellites operated by the US defense force observes microwave heat radiance. Radiance of microwave varies with absorption and scattering by water vapor, snow cloud, and variance of land surface status. Snow coverage, sea ice coverage, precipitable water content, precipitation, sea surface wind speed and other variables can be retrieved (Hollinger et al. 1989, 1991).

Brightness temperature data of DMSP series satellites F08, F10, F11, F13, F14, and F15 were acquired from NOAA/NCDC and Comprehensive Large Array-data Stewardship System (CLASS) since 1987. Precipitable water and GPVs of snow coverage (as referred in 3.4.b) were retrieved from the data. Precipitable water was retrieved using the method described by Takeuchi (2002). Bias correction between the satellites was based on “decode 4” software (Wentz 1991, 1993).

c. AMV

As a special contribution to JRA-25, MSC/JMA reprocessed High-density Atmospheric Motion Vector (AMV) data from GMS-3 to GMS-5 for the period from 1987 to 2003. These were processed using the MSC operational AMV extraction method (Kumabe 2004). A Quality Indicator (QI) was assigned to each vector according to Holmlund (1998).

As for the AMVs from geostationary satellites other than GMS, EUMETSAT reprocessed AMVs of METEOSAT-2 for the period May 1982 to May 1988 for ERA-40 and these data were also used in JRA-25. For other periods, operationally available SATOB and BUFR-AMV were used.

d. Other satellites and remote sensing data

Two additional sources of microwave scatterometer observations are available for JRA-25; the Active Microwave Instrument (AMI) on board European Remote-sensing Satellite (ERS)-1 and ERS-2, and SeaWinds on board the NASA's Quick Scatterometer (QuikSCAT) satellite. Sea surface wind vectors are retrieved from microwave back scattering strength. ERS series satellites are launched by the European Space Agency (ESA). In JRA-25, only ERS data

archived at JMA were assimilated (24 April 1995 to 17 January 2001). U.S. QuikSCAT data have been assimilated since 30 September 2001, but there are occasional missing data in JMA archives prior to 13 February 2002. While ERSs data are in narrow orbital bands of about 500 km width and there are wide data-empty areas between orbits, QuikSCAT covers wider orbital bands of about 1800 km, with very small data gap between orbits. Consequently QuikSCAT has a significant advantage in uniformly covering large part of the ocean.

Wind profiler data is a remote sensing observation from the earth's surface; vertical wind profiles are observed using Doppler shift of scattering radio waves. Detailed wind profiles can be obtained with high vertical resolution and high frequency. The U.S. wind profiler data have been assimilated since the end of July in 1993. Japanese data available from 2001 and European data available from 2002 were assimilated. These data are available in limited areas only.

Moderate Resolution Imaging Spectroradiometer (MODIS) polar wind data have been assimilated since 9 June 2004 but the available period is very short, near the end of the JRA-25 reanalysis years. MODIS wind data are retrieved from infrared and moisture images of MODIS on board polar orbital earth observation satellites Terra and Aqua. MODIS provides very valuable upper winds in the polar region, where previously no data had been available. Assimilating these data contributed to a remarkable improvement in numerical forecasts (Kazumori et al. 2005).

2.3 Quality control and use of data

A six hourly global data assimilation cycle was carried out in JRA-25. The data assimilation method is a 3D-Var which was operational in JMA from September 2001 to February 2005. Quality control and the use of observational data in the data assimilation system are described in this subsection.

a. General quality control of observational data

There are many types of low-quality observational data due to human and other rough errors. The data also suffer from large systematic biases. Quality of the analysis will be greatly degraded if single low-quality observation is

unexpectedly accepted and assimilated. To prevent such a problem, erroneous data must be excluded through quality control as the first step of data assimilation. It is an essential and important process, necessary to maintain high quality in the subsequent analysis.

The JRA-25 quality control (QC) method is almost the same as that of the JMA operational method. QC is applied for each type of observation using appropriate techniques, which are listed in Table 2. Basic QCs such as climatological checks are applied to most of the data types. In the JMA's operational system, complex QC is applied to upper air radiosonde observations. In addition, track checks are applied to moving observational stations such as ships, drifting buoys, and aircraft. These QC systems also try to automatically correct erroneous data when possible. JMA originally developed "Dynamic QC" techniques (Onogi 1998) based on departure statistics for most types of data. The separate "Group QC" (Nomura and Tahara 1997) is also developed and applied for

sea surface winds from scatterometer data to fix the problem of wind direction ambiguity. For satellite data, especially for orbital satellite data, specialized QC methods are required for each individual satellite type as described in the following paragraphs. Since JMA operations never assimilated TOVS radiance data from TIROS-N through NOAA-14, we developed QC and assimilating methods by ourselves.

A problem peculiar to JRA-25 is duplication in observational data. The observational data used in JRA-25 were acquired from many data sources. There are many duplicates in ERA-40 and the JMA observational database because both datasets are accumulations of reports from the GTS. Duplicate data were combined by excluding data with the same type, observation time, and position, then quality controlled in the data assimilation system. In cases where an unequal number of reports are found in what would otherwise be duplicate observations, the data with more reports are given priority for selection. In cases where such dupli-

Table 2. General Quality Control (QC) procedures for observational data.

Major QC processes	Target data type
Blacklist	conventional and satellite wind
TOVS/ATOVS blacklist	TOVS/ATOVS
Climatological check	All data
Track check	SHIP, drifting buoy, aviation
Consistency between parameters	SYNOP, SHIP
Wind speed correction depends on elevation of instrument	SHIP
Radiosonde bias correction	radiosonde
vertical consistency of temperature	radiosonde
vertical consistency of wind	radiosonde
TOVS/ATOVS bias correction	TOVS/ATOVS
TOVS/ATOVS 1D-Var	TOVS/ATOVS
Gross error check (dynamic QC)	conventional and satellite wind
Space consistency check (dynamic QC)	conventional and satellite wind
Group QC	sea surface wind of scatterometer
SSM/I quality check	SSM/I
Reassignment of vertical levels	satellite wind data of a part of satellites

Table 3. TOVS and ATOVS channels used in JRA-25.

	Channel	center of weighting function	Acceptable condition	Absorption material
HIRS	2	60 hPa		CO ₂
	3	100 hPa		CO ₂
	4	400 hPa	clear, over sea	CO ₂
	5	600 hPa	clear, over sea	CO ₂
	6	800 hPa	clear, over sea	CO ₂
	7	950 hPa	clear, over sea	CO ₂
	10	900 hPa	clear, over sea	H ₂ O
	11	700 hPa	clear, over sea	H ₂ O
	12	500 hPa	clear, over sea	H ₂ O
	15	700 hPa	clear, over sea	CO ₂ /N ₂ O
MSU	2	700 hPa	clear, over sea	O ₂
	3	300 hPa	clear, over sea	O ₂
	4	90 hPa		O ₂
SSU	1	15.0 hPa		CO ₂
	2	4.0 hPa		CO ₂
	3	1.5 hPa		CO ₂

(a) Channels used in JRA-25 TOVS assimilation

cated data cannot be unified, unification is left to the successive quality control procedures and decisions are left to the QCs.

The observation feedback files produced from the QC procedure are archived at every data assimilation cycle. The file is called CDA (Comprehensive Database for Assimilation), and the format is the same as the file operationally archived. The CDA has many kinds of information; not only observed values, but also interpolated first guess, departure from guess, analysis, results of QC, thresholds of QC, and other information.

b. Assimilation of TOVS

TOVS Equivalent black body temperatures (TBB) were assimilated for the period from January 1979 to October 1998. Because JMA had no previous experience with the assimilation of TOVS TBB, an assimilation and QC system was independently developed for JRA-25 based on the JMA operational ATOVS assimilation system (Okamoto et al. 2005). Since the

tropospheric channels can have dominant impact on the climate signal, we took a conservative approach, selecting only those channels requiring a simple QC procedure.

HIRS and MSU observations were assimilated as level-1d and SSU observation assimilated as level-1c. RTTOV version 6 (Saunders et al. 1999) was used for the radiative transfer calculations. Procedures especially developed for JRA-25 are described in Sakamoto et al. (2005). Here we give a brief outline.

(1) Cloud detection and channel selection

Channels used in JRA-25 TOVS assimilation are shown in Table 3 (a). The tropospheric channels were used only over the cloud free ocean. Cloud detection was implemented by a comparison of HIRS window channels using the thresholds of McMillin and Dean (1982). To exclude contaminations by thin cirrus and/or thick aerosol, the clear spot rate was readjusted to be less than 25% by comparing SST and the window channel TBB.

Table 3 (continued)

Condition Channel	sea clear/cloudy	sea thick cloud	sea rain	sea ice clear/cloudy	land clear/cloudy
AMSUA1					
AMSUA2					
AMSUA3					
AMSUA4	○				
AMSUA5	○				
AMSUA6	○			>1,500 m	>1,500 m
AMSUA7	○	○	○	>2,500 m	>2,500 m
AMSUA8	○	○	○	○	○
AMSUA9	○	○	○	○	○
AMSUA10	○	○	○	○	○
AMSUA11	○	○	○	○	○
AMSUA12	○	○	○	○	○
AMSUA13	○	○	○	○	○
AMSUA14					
AMSUA15					
AMSUB1					
AMSUB2					
AMSUB3	○	○			
AMSUB4	○	○			
AMSUB5	○	○			

(b) Channels used in JRA-25 ATOVS assimilation

For AMSUA ch6 and ch7, the values are restriction of elevation

(2) Bias correction

Because the optimized solution of 1D-Var can be regarded as the best estimate of the true atmospheric profile, the mean departure of observation from the optimal solution was considered as a bias and used as a correction. The bias was automatically updated using statistics renewed each cycle.

(3) Time window and thinning

In the upper stratosphere there were very few observations other than TOVS. Because a NOAA satellite takes about 12 hours to cover the whole globe, the unobserved region is quite extensive during a 6-hourly assimilation time

window. Due to the large spatial correlation length used in 3D-Var, the TBB observations affect the unobserved areas as well. The unfavorable large impact over the data-sparse regions should be reduced to prevent unstable analysis in the stratosphere. For this reason, the assimilation time window for the stratospheric channels was extended to 12 hours. Data spots outside of original 6-hour time window were thinned twice as much as those inside. The time window extension was introduced for HIRS channel-2 and all three SSU channels. During periods of single satellite observation, the window extension was also adopted for HIRS channel-3 and MSU channel-

4. In some cases, TOVS observation was thinned more sparsely to weaken adverse effects of the non-uniform data distribution (see Fig. 26).

Despite these efforts, temperatures in the stratosphere and the upper troposphere suffered from discontinuities in analysis when changes of the observation system took place because of discrepancy between the forecast equilibrium state and the observations.

c. Assimilation of ATOVS

Radiances from ATOVS were assimilated following the scheme implemented into operations in March 2005 for ATOVS level 1c brightness temperature data (Kazumori et al. 2005). The scheme is based on the ATOVS 1d brightness temperature data assimilation scheme (Okamoto et al. 2005), and the replacement of the RTTOV-6 (Saunders 2000) radiative transfer model by RTTOV-7 (Saunders 2002) resulted in some improvements. Channels assimilated in JRA-25 are listed in Table 3 (b). Among the three ATOVS sensors, only data from AMSU-A and AMSU-B were assimilated. Radiances from HIRS/3 are sensitive to clouds, and cloud detection is required prior to assimilation. We were unable to develop a satisfactory cloud detection scheme that improved analysis when HIRS/3 is used in addition to AMSU. Therefore a decision was made not to use data from HIRS/3. Nevertheless, as described in 4.11, 500 hPa geopotential height forecast scores in the Southern Hemisphere are better in the ATOVS period than in the TOVS period. Radiances from AMSU are not as sensitive to clouds as those from HIRS/3, so there are more data from AMSU available in cloudy regions. In addition, the number of channels has been increased from 4 in MSU to 20 in AMSU (15 in AMSU-A and 5 in AMSU-B). It is believed that these factors contributed to the improvement of the forecast scores.

For the ATOVS radiances, a fixed bias correction was applied throughout the lifetime of the satellite. Radiosonde measurements were used to calculate regression coefficients for air-mass dependent bias corrections. In the upper stratosphere where few radiosonde observation are available, first guess fields were used as supplementary information to estimate vertical temperature profiles. TOVS data were switched to

ATOVS data in November 1998 without an overlap in the assimilation. Because of the difference in the bias correction methods between TOVS and ATOVS, an artificial discontinuity occurred in the stratospheric temperatures.

d. Assimilation of AMV

Since 1979, AMV data have been produced continuously from successive images of a geostationary satellite over the tropics and middle latitudes. In the utilization of AMV data, besides the application of the common QC method explained in 2.3.a, the data are automatically thinned by 50 km interval if they are spatially too dense. Furthermore, AMV observational error adjustments are applied in the assimilation.

The Quality Indicator (QI) associated with AMVs are directly used by the QC system to select high-quality vectors. This procedure is applied to the reprocessed GMS and METEOSAT-2 AMVs (described in 2.1.b), and to METEOSAT AMVs after September of 1998 (Rattenborg 1998).

AMV data could effectively contribute to the improvement of analysis wind and other variables due to the high spatial and temporal distribution. In the period from 1982 to 1988, and in the southern middle latitude where METEOSAT-2 reprocessed AMV data are used, the JRA-25 upper tropospheric (above 400 hPa height) westerly winds are weaker than those of ERA-40 by about 2.0 m s^{-1} . This suggests that the slow bias of the upper tropospheric westerly wind seems to affect JRA-25 more conspicuously than ERA-40 because of the AMV application method difference. In the AMV data impact test performed separately for July of 2002 and 2003, some impacts are found in the tropical Indian Ocean, where the upper tropospheric easterly winds are intensified, and the precipitation fields are effectively modified when AMV data are used (Oyama 2007).

e. Bias correction of radiosonde temperature

Upper air radiosonde observation is a basic direct observation, and the data quality is generally good. However, instruments are different for different countries and they were often exchanged with newer or different instruments even within a country over periods of time. Historically, radiosonde radiation correction also was applied differently in different countries. Thus, since the quality of historical

radiosonde observations is so varied, a bias correction of radiosonde observations is essential in a reanalysis.

In JRA-25, the method of Andrae et al. (2004) was applied to correct temperature bias. Other variables such as wind and humidity were not corrected. The method was developed using the historical performance of radiosondes (Onogi 2000). In the method, statistics are calculated from the differences between observed and interpolated background values. The statistics are taken for each country or region, assuming that they use a similar type of radiosonde. The solar radiative heating in and above the upper troposphere combined with the emitted long wave radiation from the sensor produce a bias that is a function of the solar elevation. The bias is therefore calculated for four different classes of solar elevation. There are three types of corrections: no correction, correcting radiation bias only, correcting systematic bias as well as radiation bias. The selection of the type of bias correction is different for different months and is determined based on the result from Onogi (2000).

Bias correction coefficients are based on the departures, defined as observation minus first guess values, averaged over the latest 12 months. The correction coefficients are adjusted to reduce the corrections derived from the mean departures because the departure includes not only observation bias but also model bias. Since separating model bias and instrument bias is difficult, several experiments with different coefficients were performed to estimate the appropriate magnitude of correction. The coefficients were adjusted based on results of preliminary experiments. The method of Andrae et al. was originally developed for ERA-40, but in JRA-25 the renewal of the correction coefficients is more frequent than in ERA-40; in JRA-25, the coefficients are renewed every month by using departure statistics of the latest 12 months, whereas in ERA-40, the coefficients are renewed at a determined time in advance. An example of bias statistics is shown in Fig. 2.

f. Blacklist

There are stations reporting extremely anomalous observational values. Since analysis degrade greatly if such problematic data are as-

simulated, those stations should be blacklisted and excluded in advance. In particular, a drifting buoy is an unmanned observation station released into an ocean that goes through conditions more difficult for stable measurements than other types of observations. These buoys are usually released into data-sparse oceans, hence their influence on the resulting analysis is quite large. So it is essential to blacklist such a problematic station as soon as possible after it occurs.

In the operational system, an operator can manually check observations and blacklist erroneous stations, but such manual operation is impossible during the reanalysis because the data assimilation cycle progresses for over 10 days per real day. In the past, operational blacklists were not archived (except during recent years). Consequently, an automatic blacklist renewal system has been introduced for drifting buoys, which is based on departure statistics of the surface pressure measurements during the latest 14 days of observation. Stations whose departures exceed a certain threshold are blacklisted, while stations are removed from the blacklist when the departure becomes smaller than the threshold. A threshold value was tuned with reference to thresholds used in the operational system. For other conventional observations, an automatic blacklist system was not introduced. A problematic station is manually blacklisted if we can detect a problem. For TOVS and ATOVS data, individual detailed blacklists were created in advance by preliminary quality checks.

3. Data assimilation and forecast models

In JRA-25, a six hourly global data assimilation cycle was carried out for 26 years. In the data assimilation cycle, 6-hour forecast from an initialized analysis and data assimilation using the 6-hour forecast as a first guess are repeated. A data assimilation cycle is a very powerful method of providing physically consistent atmospheric analysis and time variations and of providing initial conditions for a numerical forecast. The forecast model used in JRA-25 is a low-resolution version of the model used in the JMA operational data assimilation system (JMA 2002).

This section describes each step involved in

198207-198306 43N-50N,130W- 50W USA (NORTH)

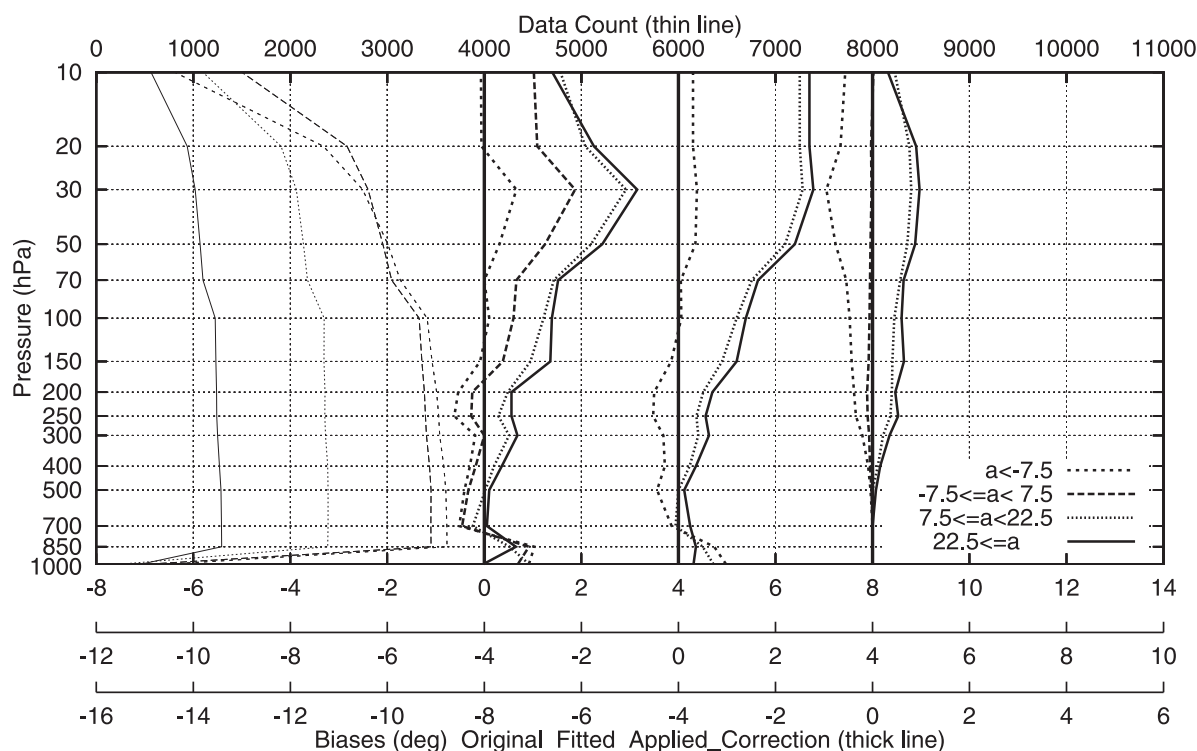


Fig. 2. An example of monitoring radiosonde bias correction.

The graphs from left to right indicate the number of observations, first guess departures, fitted profiles after smoothing, and suggested correction values. Different line marks correspond to different solar elevations (degree).

JRA-25 data assimilation system and forecast model. In addition to the data assimilation cycle, an 8-day forecast was carried out every 5-days from 12UTC to validate the quality of reanalysis fields.

3.1 Data assimilation system

The JRA-25 data assimilation (DA) system employs a 3-dimensional variational analysis method (3D-Var) with 6-hourly data assimilation cycles (JMA 2002, Takeuchi and Tsuyuki 2002). The 3D-Var analysis was used in JMA operations prior to February 2005. The specifications of the DA system are listed in Table 4.

In the 3D-Var, a 6-hour forecast from GSM (T106L40) is used as a first guess (background). All observational data within 3 hours (−180 to +179 minutes) of the analysis time are considered valid at the analysis time. The standard incremental approach (Courtier et al.

1994) is adopted, in which the variational problem is first linearized about the model background and then solved to obtain the analysis increment, which is the change to the background that results in the best fit to observations. In JRA-25, the analysis increment has the same resolution (T106L40) as the model, in contrast with the operational system at JMA, which has a higher horizontal model resolution (T213). To minimize the cost function, the limited memory Broyden Fletcher Goldfarb Shannon (L-BFGS) algorithm (Liu and Nocedal 1989) is used.

The analysis variables are relative vorticity, divergence, temperature, model surface pressure, and logarithm of specific humidity, represented in spectral space on the model layers in a hybrid sigma-pressure coordinate. Temperature instead of geopotential height is assimilated from radiosonde observations.

Table 4. Specifications of the 3D-Var data assimilation system used in JRA-25.

Horizontal coordinate	Gaussian grid
Horizontal resolution	1.125 degrees
Number of horizontal grid	320×160
Vertical coordinate	hybrid sigma-pressure coordinate
Number of vertical layer	40 layers
Pressure of model top level	0.4 hPa
Data assimilation method	3D-Var
Assimilated variables	Temperature, wind, relative humidity, surface pressure at model surface, radiative brightness temperature (TOVS/ATOVS), and precipitable water (SSM/I)
Background error statistics	Statistics in 2003
Surface analysis	2D-OI (temperature, wind and relative humidity)
TOVS data	HIRS + MSU level 1d, SSU level 1c
ATOVS data	AMSU-A, AMSU-B level 1c (HIRS not used)

For the background term of the 3D-Var, multivariate coupling is primarily based on linear geostrophic balance between mass and wind error fields. Additional statistical relations are included to reduce geostrophic balance in the smaller horizontal and vertical scales, to decouple wind and mass variables near the equator, to allow for a dependency of the degree of geostrophy on the vertical level, and to impose a weak coupling between divergence and vorticity. The correlation structures do not depend on geographical location, but vertical correlations depend on horizontal scale. The regression coefficients and background error correlations are computed statistically using the NMC method (Parrish and Derber 1992). The background error statistics were obtained from 24 and 48-hour forecast differences of 2003 operational analyses, which were the latest available at the time JRA-25 production started.

An adjustment method introduced by Fujita (2004) improved the analysis by reducing strong correlations of low wave number components in the background error covariances, which caused unrealistic analysis increments in an early version of the JMA 3D-Var.

Observation errors are specified individually for each observation type and variable. Vertical error correlations of radiosonde data and

sounder data such as TOVS/ATOVS are explicitly accounted for. To compensate for horizontal error correlations of satellite data, the observation error is modified according to the horizontal density of observations.

Reported surface pressure data at station height, as well as sea surface pressure observations, are converted to surface pressures on the model surface prior to assimilation. Surface pressure is assimilated simultaneously with upper air data in the 3D-Var; the other surface observations (temperature, wind and relative humidity), however, are used separately in a univariate two-dimensional optimal interpolation surface analysis (2D-OI). Consequently, there can be some inconsistency between the upper air and surface fields in the analysis.

If a scheme was not implemented in the operational system, or was still in the development stage, experiments were carried out to check the impact of the scheme for JRA-25. The schemes giving positive impacts were accepted into the JRA-25 system. In particular, assimilating SSM/I precipitable water (PW) (Tauchi et al. 2004) significantly improved precipitation. The retrieved SSM/I PW data performed well in JRA-25 with very small biases, as mentioned in 4.1.

3.2 Global forecast model

a. Framework, dynamics and numerics

The model used in JRA-25 is a low-resolution version of the operational JMA Global Spectral Model (GSM) (JMA 2002). It has a spectral resolution of T106, which is equivalent to a horizontal grid size of approximately 120 km, and has 40 vertical layers in hybrid sigma-pressure coordinates with the top level at 0.4 hPa. The equations are solved in Eulerian form (replaced by a semi-Lagrangian scheme in JMA operations in February 2005). The model topography was created from the very fine mesh land global digital elevation database GTOPO30, which

was developed in a collaborative effort with several institutes led by the United States Geological Survey (USGS). Most of the specifications for the GSM used in JRA-25 are described in JMA (2002). The specifications for both the dynamical and physical processes of the model are listed in Table 5.

The prognostic variables for describing the dry atmosphere are vorticity, divergence, temperature, and surface pressure (rather than the logarithm of surface pressure). Moist variables are specific humidity and cloud water content, but advection is not taken into account to predict the latter. The vertical finite difference scheme follows Simmons and Burridge

Table 5. Specifications of the forecast model used in JRA-25: the Global Spectral Model (GSM).

Equation	Primitive equation with hydrostatic
Forecast variables	vorticity, divergence, temperature, specific humidity, cloud water and surface pressure
Time integration method	Euler, semi-implicit, leap-frog (3 time levels)
Horizontal discretization	Spectral method
Horizontal coordinate	Gaussian grid
Horizontal resolution	1.125 degrees
Number of horizontal grid	320×160
Basis function	spherical harmonics
truncation wave number	triangular 106
Vertical discretization	calculus of finite difference
Vertical coordinate	hybrid sigma-pressure coordinate
Number of vertical layer	40 layers
Pressure of model top level	0.4 hPa
Topography	defined from GTOPO 30
Land and sea data	USGS (US Geological Survey)
Initialization	Non-linear normal mode initialization
Precipitation process	Prognostic Arakawa-Shubert convection
Surface boundary layer	Monin-Obkhov similarity
Planetary boundary layer	Level 2 closure model
Land surface	Simple Biosphere (SiB)
Long wave radiation	Wide band model (3 hourly)
Short wave radiation	18 wavelength band, 2-direction approximation (hourly)
Gravity wave drag	Long and short wave drag

(1981). The prognostic variables are defined for each level, while the advections are diagnosed at each interface between adjacent levels.

A trapezoidal semi-implicit time integration scheme is applied to the linearized gravity wave terms. Vorticity and moisture advection by the mean zonal wind are also treated implicitly (Jarraud et al. 1982). Time integration of nonlinear terms is done with a leap-frog scheme and an Asselin time filter (Asselin 1972).

b. Convection and precipitation

A prognostic mass-flux type Arakawa-Schubert scheme (Arakawa and Schubert 1974) was adopted for cumulus parameterization.

For computational efficiency, two simplifications are introduced. First, the vertical profile of the upward mass flux is assumed to be a linear function of height as proposed by Moorthi and Suarez (1992). Second, the mass flux at the cloud base is determined by solving a prognostic equation (Randall and Pan 1993), rather than by applying the quasi-equilibrium assumption. The cloud base level is fixed near 900 hPa in the model. Thermodynamic properties of the upward mass flux at the cloud base are given by the vertical means of the grid-scale values below the cloud base. An excess energy proportional to the mixing length of the planetary boundary layer is added to the moist static energy at the cloud base in order to take the turbulence effect into account. Further details of the scheme are described in Aonashi, Kuma and Matsushita (1997). The scheme was updated by Nakagawa and Shimpo (2004) by considering the effect of detrainment due to downdraft instead of simply re-evaporating the precipitation. This more realistically represents convective downdraft, which cools and moistens the lower troposphere.

c. Cloud and cloud ice

After the publication of JMA (2002), the following two new schemes were implemented.

A new stratocumulus parameterization by Kawai and Inoue (2006) was introduced, in which cloud fraction is diagnosed mainly as a function of inversion strength. The global distribution of marine stratocumulus clouds off the west coast of continents is improved remarkably with this new scheme. With the im-

proved cloud amount, the radiation fields are also improved.

A new cloud ice scheme by Kawai (2003) that treats descent of ice more accurately was implemented. The numerical treatment of ice descent is based on an analytically integrated solution, which replaced the previous simple scheme in which cloud ice descends to the next lower layer or immediately to the ground. This scheme removed the unphysical dependency of cloud ice fall distance to time step.

d. Radiation

The basic framework for the computation of long wave fluxes and cooling rates follows Sugi et al. (1990). Longwave radiation is treated by a broad-band flux emissivity method for four spectral bands. Shortwave scattering and absorption are modeled by a two-stream formulation using the delta-Eddington approximation (Joseph et al. 1976; Coakley et al. 1983), where the spectrum is divided into eighteen bands as described by Briegleb (1992).

Radiatively active gases are prognostic water vapor, 3-dimensional daily ozone (see 3.4.a), and constant globally uniform carbon dioxide (375 ppmv) and oxygen (209,490 ppmv). Concentration and optical properties of aerosols are specified as the continental and maritime types of background values without seasonal variation. Cloud fraction and water content are provided by the cloud scheme. An effective radius of cloud liquid droplets is fixed at 15 microns, while that of ice crystals varies in the range 20–150 microns according to temperature.

The model used in JRA-25 has a systematic large negative temperature bias up to 2 degrees (maximum around at 30 hPa level) in the lower and middle stratosphere and a large positive temperature bias up to 5 degrees (maximum around at 2 and 3 hPa level) in the upper stratosphere. The major problems in radiation fluxes are the shortage of clear sky downward long wave flux at the surface and large planetary albedo. These biases are significantly reduced in a new radiation scheme (Murai et al. 2005) which was implemented in December 2004; regrettably it was not available in time for the start of JRA-25 production. The temperature biases in the stratosphere generate inconsistencies between satellite radiance obser-

vations and the model background fields in the data assimilation. This may cause time discontinuities in the analyzed temperatures in the stratosphere when changes or gaps in satellite data coverage occur, as described in 2.3.b and 4.8.

e. Surface turbulent flux and vertical diffusion

Surface turbulent fluxes are formulated as bulk formulae following Monin-Obukhov similarity theory. Over land, surface roughness lengths are determined from the vegetation type and are altered by snow cover. Over the ocean, surface wind stress depends on oceanic waves excited by surface wind, and the roughness length and wind-induced stress are iteratively calculated in the model. Following Beljaars (1995), surface roughness lengths over ice-free ocean are obtained using the Charnock (1955) relation. The level 2 turbulence closure scheme of Mellor and Yamada (1974) is used to represent vertical diffusion of momentum, heat, and moisture.

f. Gravity wave drag

The parameterization of orographic gravity wave drag consists of two components; one for long waves (wavelengths over 100 km) and one for short waves (wavelengths around 10 km). Long waves are assumed to propagate upward until reaching wave-breaking levels, mainly in the stratosphere, where they exert drag (type A scheme). Short waves are always regarded as trapped and dissipating within the troposphere (type B scheme). Therefore the fundamental difference between the two schemes appears in the vertical distribution of the momentum deposit. The type A scheme is based on Palmer et al. (1986) with some modifications; see Iwasaki et al. (1989a, 1989b) for details.

g. Land surface process

For land surface processes, a Simple Biosphere (SiB; Sellers et al. 1986; Sato et al. 1989) scheme is employed. Soil moisture is predicted in three layers. Vegetation types are obtained from Dorman and Sellers (1989). Long term vegetation change is not considered.

The SiB is connected to the surface boundary layer scheme through the temperature and specific humidity of canopy space. Vegetation types

in the SiB scheme determine the surface roughness lengths.

Snow depth provided by the snow depth analysis (see 3.3) is used as an initial value for snow water. Snow mass is not represented explicitly and is regarded as frozen water on bare ground with an assumption of constant snow density, 200 kg m^{-3} .

A problem related to snow is melting. According to the result of a long term model integration experiment, snow melts earlier in general than observed. However, the problem does not appear in JRA-25 because observed snow data were used.

h. Initialization

Although the 3D-Var provides dynamically well-balanced atmospheric fields for the GSM, small imbalances caused by the incremental method in 3D-Var are not negligible. Therefore an initialization procedure is still needed. A nonlinear normal mode initialization which includes all physical processes is performed in order to suppress high frequency gravitational oscillations. A physical initialization (Aonashi et al. 1997) is not used.

3.3 Land surface analysis and snow depth analysis

For land surface analysis, the Tokuhiro (2002) scheme, which is used to create a land initial condition for the JMA operational seasonal forecast, was adopted. The scheme is a modified version of the SiB, which provides a realistic land surface evolution in long term seasonal integrations. The land surface situation is evaluated by inverting the SiB scheme equation using atmospheric forcing fields. The 10-year "off-line" integration of land model, using ERA-15 reanalysis as a forcing, demonstrated that the simulated soil moisture showed good agreement with long term soil data observed in the State of Illinois in the United States. The atmospheric forcing to the land model are pressure, temperature, specific humidity, winds at the lowest level of the model, as well as the surface pressure, large scale precipitation, convective precipitation, downward short and long wave radiance fluxes and total cloud amount. In JRA-25, Tokuhiro's scheme was implemented into the data assimilation cycle as shown in Fig. 3. The obtained

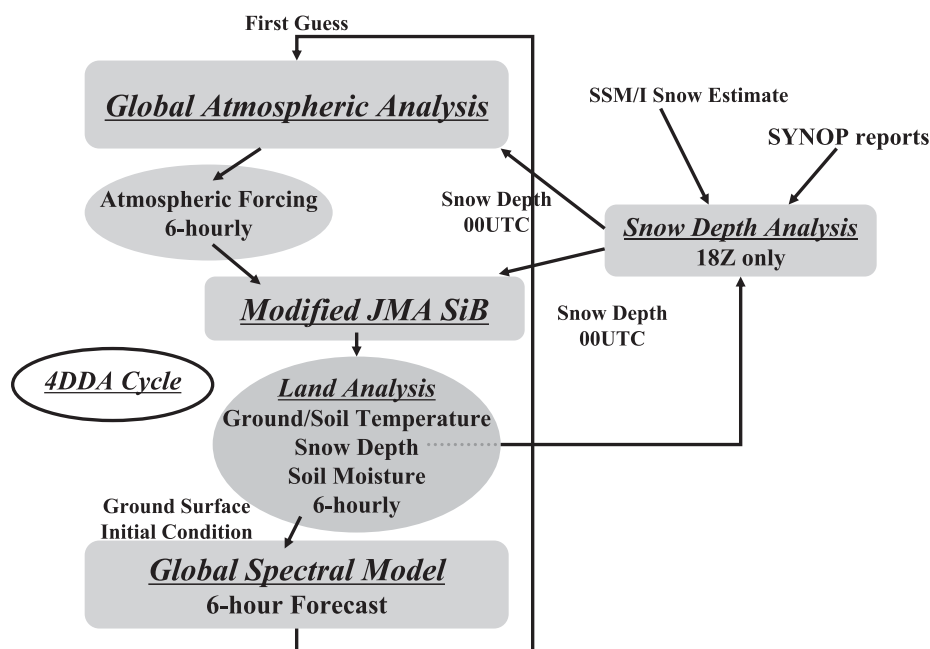


Fig. 3. Land surface analysis in JRA-25.

Land surface status is estimated every 6 hours by using atmospheric fields during the data assimilation cycle to force the SiB (Simple Biosphere model). Snow analysis is performed once a day to give the latest snow analysis to the cycle.

land states are updated at the next analysis time using the atmospheric forcing from the forecast model.

The latest snow depth observation is taken into the land surface analysis cycle once a day. Snow depth analysis was performed once a day on a T106 Gaussian grid using a 2D-OI scheme. Observational data used are snow depth data from surface synoptic observations (SYNOP) reports, including the digitized Chinese snow depth data. Since July 1987 when the SSM/I data became available, the snow cover obtained from SSM/I was used. An observation error of snow depth data is specified depending on the snow coverage rate. Distribution and data count of SYNOP snow data varies largely by day and/or by year. Daily SSM/I snow coverage data come with very few missing periods, resulting in a snow analysis without significant discontinuities.

3.4 Boundary data

The next three sets of data are given to the model as boundary data. They are not assimilated in the data assimilation system.

a. SST and sea ice

For SST, Centennial in-situ Observation-Based Estimates of variability of SST and marine meteorological variables (COBE) (Ishii et al. 2005) daily data produced by JMA were used. COBE was produced for the purpose of making a consistent centennial marine dataset throughout 20th century. A long term consistent dataset of past marine observations, the International Comprehensive Ocean-Atmosphere Data Set (ICOADS) (Woodruff et al. 1998), and the Kobe collection (Komura and Uwai 1992; Manabe 1999) were used to produce the COBE dataset. No satellite data were used.

In the ECMWF and NCEP Reanalyses, United Kingdom Meteorological Office (UKMO) and NCEP SST data were used. However, the former was replaced by the latter in the middle of the reanalysis years; furthermore, available satellite observations may vary year-to-year. COBE SST was compared with the UKMO and NCEP SSTs; a slightly large difference found in the Antarctic Ocean seemed to be due to a difference of sea ice distribution, and was not con-

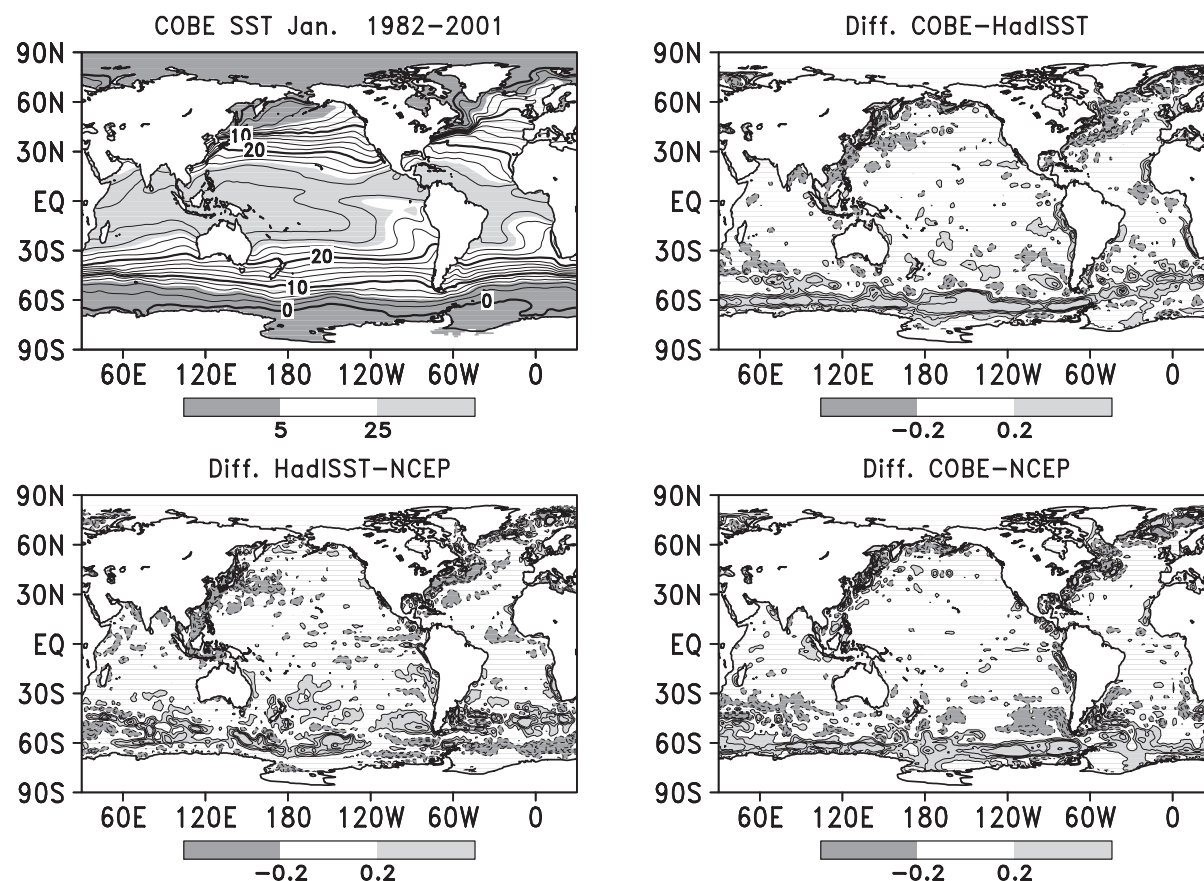


Fig. 4. Comparison of SST long-term averages in January (1982 to 1998).

SST [$^{\circ}\text{C}$] distribution (top left), differences between COBE and Hadley SST (top right), difference between Hadley SST and NCEP oiv2 SST (bottom left), and difference between COBE and NCEP oiv2 SST (bottom right) are shown.

sidered a problem. Differences are very small in most of the regions and COBE SST is compatible with those SSTs (Fig. 4). Ishii et al. (2005) compared the variability of COBE SST with that of NCEP SST. They found less variability in COBE SST than in NCEP SST because no satellite data were used in COBE. They also compared ENSO indices with HadISST (Rayner et al. 2003) and showed good agreement between them after the 1960s.

Daily sea ice distribution was obtained using the NASA team algorithm (Cavarieli et al. 1984) based on SSM/I brightness temperature and Scanning Multichannel Microwave Radiometer (SMMR) on board the NIMBUS-7 satellite (Matsumoto et al. 2006). Bias between SMMR and SSM/I were corrected with the Cavarieli (1999) method.

The daily SST and sea ice analyses were used in the JRA-25.

b. Snow coverage grid data

Grid point snow coverage dataset retrieved from SSM/I brightness temperature were available since July 1987 (Kurino 2001a; Kurino 2001b). It is 2 degree latitude-longitude resolution. This dataset was used to improve the quality of snow analysis in data-sparse regions. JRA-25 is the first reanalysis to use the snow coverage distribution retrieved from SSM/I brightness temperature. NOAA's weekly snow coverage analysis (Robinson et al. 1993) was used prior to June 1987 when no SSM/I data were available. The snow cover data was interpolated to daily values on a 1×1 degree grid. Since these data are available throughout

the JRA-25 reanalysis period, they were used whenever SSM/I data were not available. The NOAA snow coverage data has better quality in North America than in Siberia. Generally, the snow coverage data only provide a boundary condition for the snow depth analysis. Snow depth information is only given by SYNOP observations. Analysis parameters such as observation error are defined differently according to snow coverage rate.

c. Ozone

Ozone concentrations varied significantly during the JRA-25 reanalysis period as the ozone hole extended. Ozone observations were not assimilated directly in the JRA-25 data assimilation system. Instead a three-dimensional daily vertical ozone profile was separately produced in advance and provided to the forecast model, while the JMA operational model is using 3-dimensional monthly climate values. The daily profile was produced by a chemical transport model developed by MRI/JMA (Shibata et al. 2005) with “nudging” applied towards total ozone data observed by Total Ozone Mapping Spectrometer (TOMS) on board NIMBUS and other satellites. Thus, long term change of ozone concentration is taken into account in JRA-25.

4. Performance of JRA-25

Advantages and deficiencies of JRA-25 are discussed in this section. Good quality 6-hour total precipitation, good TC analysis owing to the assimilation of TCR data, and good reproduction of low-level cloud along the subtropical western coast of continents are some of the advantages found in JRA-25. At the end of the section, a history of the changes in the observation system is described.

4.1 Precipitation and precipitable water in tropics

Precipitation is a very important output variable since it provides an integrated measure of the performances of the data assimilation system. For the comparison, monthly averaged precipitations from NCEP/NCAR R1, NCEP/DOE R2, ERA-15, ERA-40 and JRA-25 on a common 2.5-degree latitudinal/longitudinal grid are compared with two observation-based

estimations of precipitation: Global Precipitation Climate Project Version 2 (hereafter GPCP) (Adler et al. 2003), and Climate Prediction Center (CPC) Merged Analysis of Precipitation combined with NCEP/NCAR R1 reanalysis (hereafter CMAP) (Xie and Arkin 1997).

Time series of the global area-weighted spatial correlations of monthly averaged precipitations with GPCP are shown in Fig. 5. Because of the area extent of the tropics and the large amount of precipitation there, the good global correlation implies good tropical correlation. In most of the month, the skill of the JRA-25 precipitation is the highest. In addition, after the introduction of the SSM/I precipitable water (PW) retrieval into assimilation, the skill increased even further. JRA-25 also has the best correlation with CMAP. The anomaly correlation of precipitation also showed the excellent performance of JRA-25 (not shown).

Monthly-averaged 850-hPa specific humidity increments are shown in Fig. 6. This figure is made for the purpose of checking the correction of moisture fields in the data assimilation before and after introducing the SSM/I PW in 1987. A slightly positive increment spread over the ocean, with small areas of negative increments over in situ observations on islands, is found in the middle and lower latitudes without SSM/I PW. The SSM/I assimilation decreased the positive increment over ocean and negative increment over islands.

To elucidate the long-term variability, global-averaged precipitation time series are plotted in Fig. 7. All the reanalyses overestimate precipitation compared to GPCP. The introduction of SSM/I did not cause discontinuity in the JRA-25 global-averaged precipitation. In addition, unlike ERA-40, JRA-25 precipitation does not show any unrealistic influence of aerosol from the Pinatubo (from Jun. 1991) and El Chichon (from Mar. 1982) volcanic eruptions. However, there is a positive drift in global precipitation in the 1990's, which is also observed in the NCEP/DOE R2. We suspect that the change in data, from TOVS to ATOVS in November 1998, and their data handling may have affected the precipitation.

The following are the possible reasons for the improved performance of the precipitation in JRA-25:

Monthly Precipitation Correlation with GPCPv2

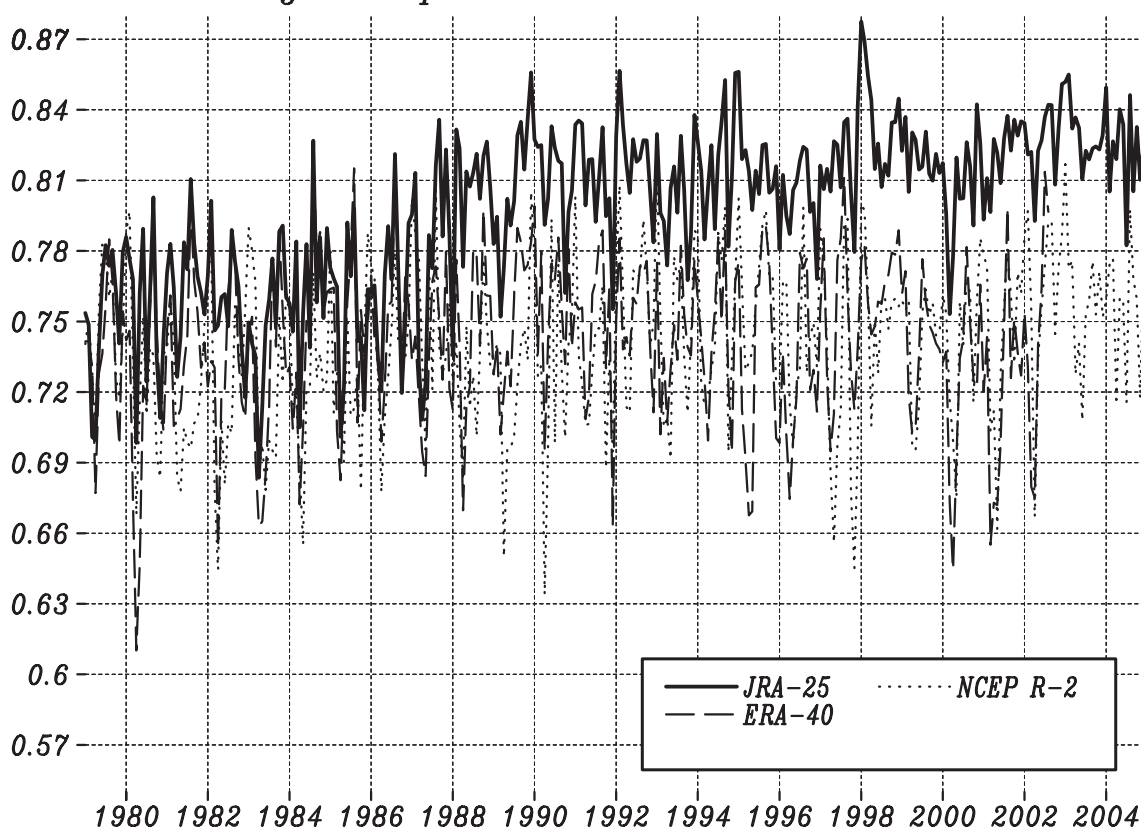


Fig. 5. Correlation of precipitation with GPCP.

Time series of the spatial correlation of monthly mean precipitation of each reanalysis and the GPCP ver.2 are shown. JRA-25 has the best correlation, especially during the period after 1987 when SSM/I PW was assimilated.

- 1) Before the production of JRA-25 began, the convection scheme in the global atmospheric model had been significantly improved for the simulation of tropical precipitation (see 3.2).
- 2) More conservative use of the TOVS sounder visible and infrared channels (Sakamoto et al. 2005) prevented ill effects of satellite data gaps and shifts in JRA-25, particularly in the middle and low latitude troposphere.
- 3) The introduction of SSM/I significantly improved precipitation over the tropical ocean. The retrieved SSM/I PW were originally much larger than the first guess, but with a careful adjustment to better fit the guess (Tauchi et al. 2004), the degradation of pre-

cipitation due to model spin-up was prevented. This adjustment also minimized the discontinuity that may arise from the introduction of the SSM/I data.

Takahashi et al. (2006) showed that geographical distributions of the occurrence of daily heavy rains in JRA-25 is similar to the GPCP over the tropical western Pacific, suggesting that the JRA-25 may be useful for the analysis of extreme precipitation events. Local performance of precipitation is discussed in the following Subsections 4.2 and 4.5. More detailed analysis and description of the JRA-25 precipitation will be made in future.

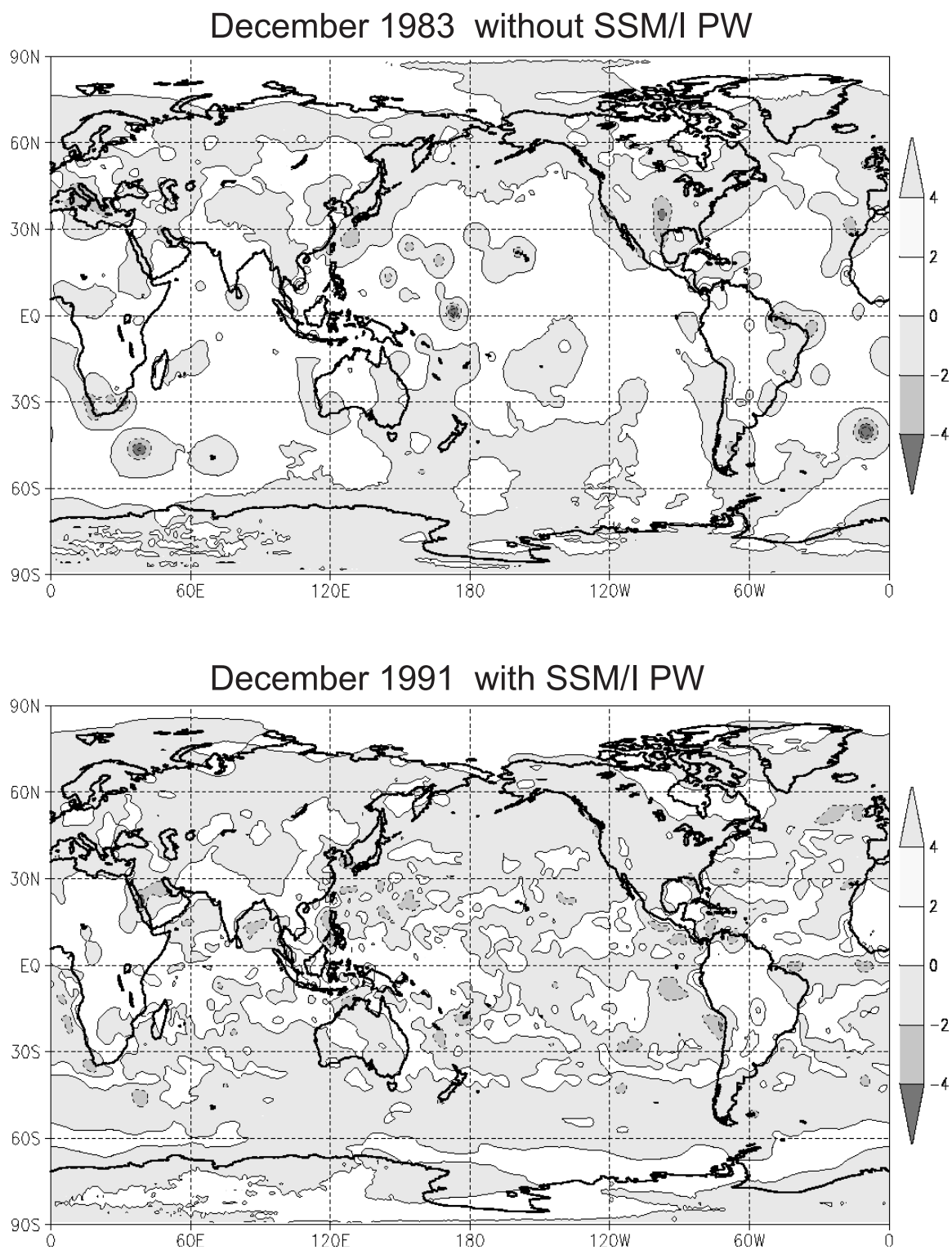


Fig. 6. Monthly-averaged increments of total column water vapor (converted to precipitation [mm]).
Top: Dec. 1983 (without SSM/I PW), Bottom: Dec. 1991 (with SSM/I PW).

Global-averaged Monthly Precipitation

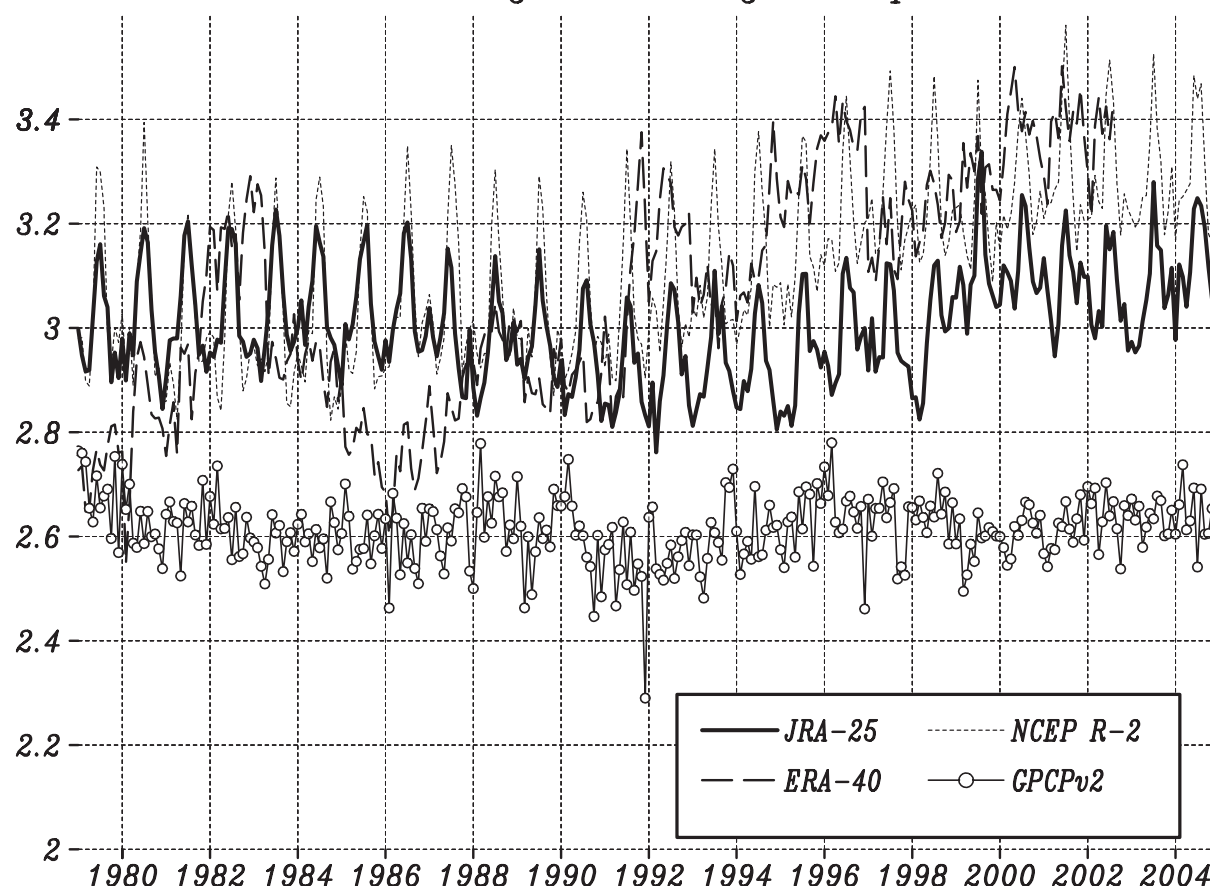


Fig. 7. Global mean precipitation [mm].

Time series of reanalyzed global mean precipitation and independent precipitation datasets are shown.

4.2 Asian Summer Monsoon (ASM)

The purpose of this subsection is to compare precipitations associated with the Asian Summer Monsoon (ASM) among several reanalysis products.

The rainfall amounts over two regions specified by Wang and Fan (1999) are compared with GPCP and CMAP data. The first is the region covering India and the Bay of Bengal (CN1: 70 E–100 E, 10 N–25 N), which represents the area of the South Asian Monsoon activity; the second is off the east coast of the Philippines (CN2: 115 E–140 E, 10 N–20 N), representing the East and Southeast Asian Monsoon activity. These two regions are selected based on outgoing long wave radiation (OLR) and CMAP precipitation as centers of

the large-scale convection associated with monsoon activity.

Figure 8a shows the interannual variations of averaged rainfall rates (mm/d) over CN1 for the 30th–48th pentads (26 May to 28 Aug). The rainfall rate of JRA-25 is larger than ERA-40, NCEP/NCAR R1, GPCP and CMAP, but slightly less than NCEP-R2. The interannual variation is generally as well reproduced as in other reanalyses, except around 1998 in JRA-25 and ERA-40. Over CN2, JRA-25 follows very closely the CMAP and GPCP rainfall rate and its interannual variations, except for a peak in 1986 (Fig. 8b). ERA-40 also reproduced the interannual variations over CN2 well.

Climatological seasonal variation associated with the ASM is also reproduced well in the in-

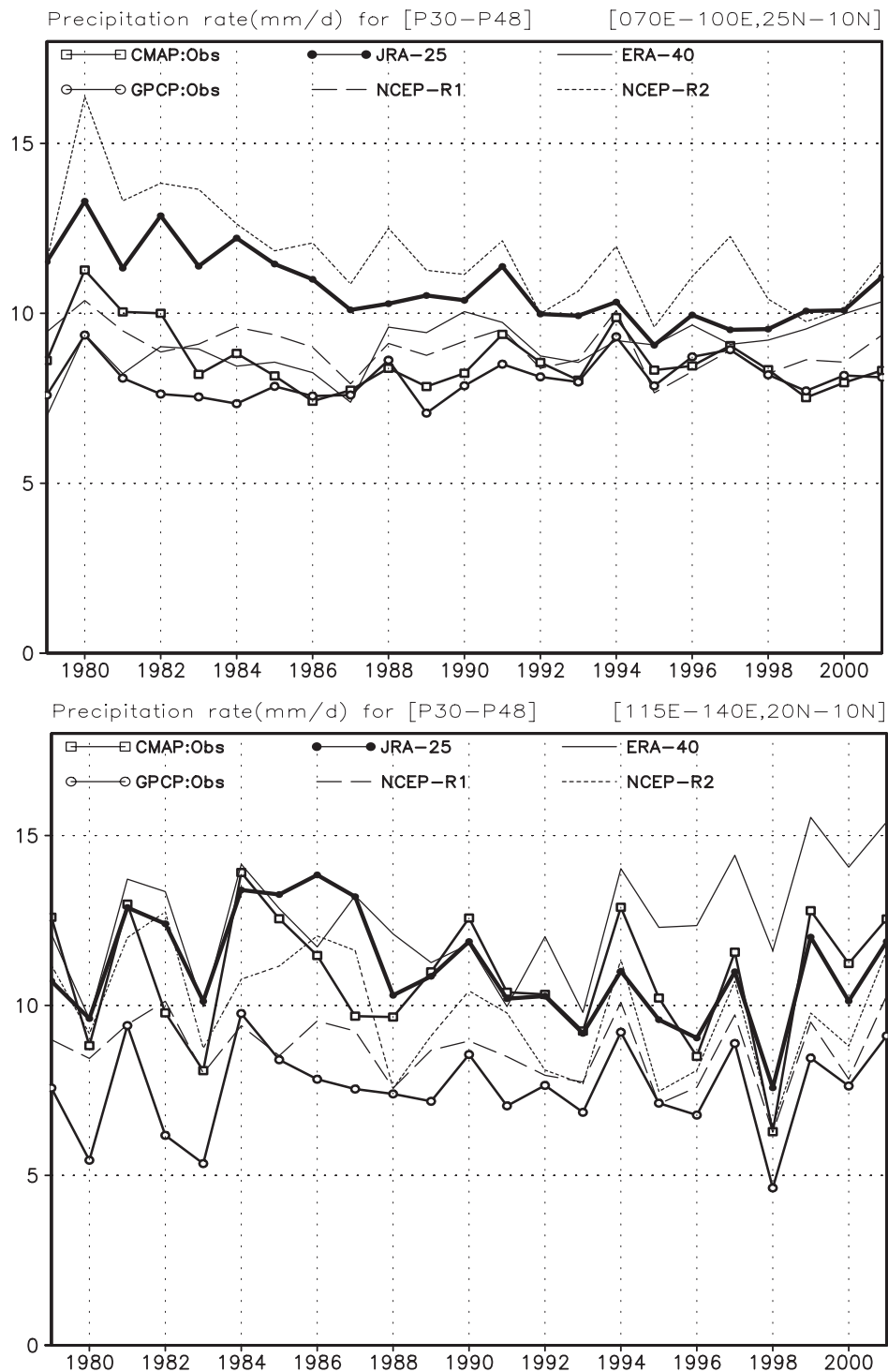


Fig. 8. Interannual variability of precipitation rates.

Interannual variability of precipitation rates [mm/day] averaged for 30th–48th pentad over the two center regions of monsoon convective activity: the India-Bay of Bengal region (70 E–100 E, 10 N–25 N: CN1) (top), and the region off the east coast of the Philippines (115 E–140 E, 10 N–20 N: CN2) (bottom).

dices in JRA-25, as well as in the other reanalyses. For instance, the seasonally phase-locked intra-seasonal variation and the onset and retrieval of monsoon are both well presented (not shown).

In summary, JRA-25 reproduces the inter-annual time scale variations reasonably well, although it overestimates the magnitude of precipitation. More effort is necessary to improve the quality.

4.3 Subtropical marine stratocumulus

Subtropical marine stratus located off the west coasts of continents is important for the radiation budget over the region. This cloud has been difficult to simulate with global atmospheric models because of their coarse vertical resolution and complex physical processes, which cannot be well reproduced by simple parameterization schemes (Sundqvist 1988; Teixeira and Hogan 2002). In the JRA-25 model, newly developed stratocumulus parameterization (Kawai and Inoue 2006), made the simulation of the subtropical marine much better. Figures 9a–c show the July climatology of low cloud from International Satellite Cloud Climatology Project (ISCCP) (Rossow et al. 1996), JRA-25 and ERA-40, respectively. The low cloud distribution in JRA-25 is very realistic, with large coverage, fitting just along the shoreline over and off the subtropical western coasts of California, Peru, Mauritania, and Angola. In these regions, JRA-25 surface insolation agrees better with the Surface Radiation Budget (SRB) (Darnell et al. 1988) as shown in Fig. 9d.

4.4 Tropical cyclones

TCR data is effective in reproducing tropical cyclones and surrounding atmospheric conditions (Hatsushika et al. 2006). Figure 10 shows examples of sea level pressures analysis around TC with observed TC locations in September 1990 in the JRA-25. Those from a control experiment that excludes the TCR data from the JRA-25 system are shown for comparison. In the eastern North Pacific (ENP) basin, qualities of TC analysis in terms of location and intensity in the JRA-25 are better compared to the control experiment. On the other hand, in the western North Pacific (WNP), the impact of the TCR data is limited. This is probably due

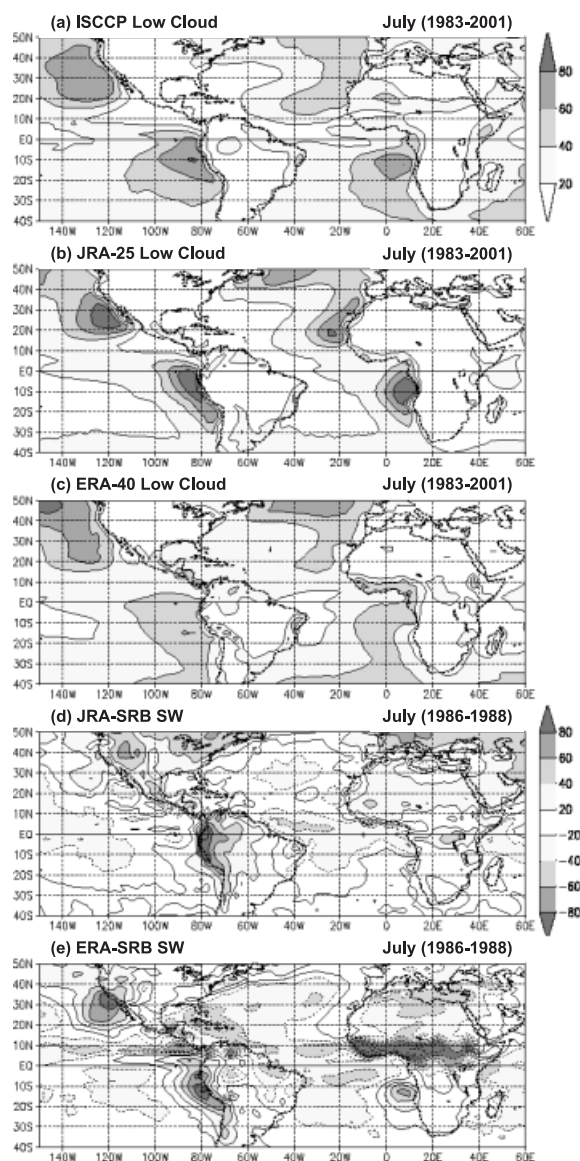


Fig. 9. Climatology of low cloud in July and the bias of short wave radiation flux at the surface.

July climatology of low cloud for a) VIS-IR low cloud by ISCCP-D2, b) JRA-25, c) ERA-40, averages for 1983–2001, respectively (in %). Difference of surface insolation from SRB for d) JRA-25, e) ERA-40, averages for 1986–1988 (in W/m^2). Accumulated values in 6-hour forecasts are used for reanalyses.

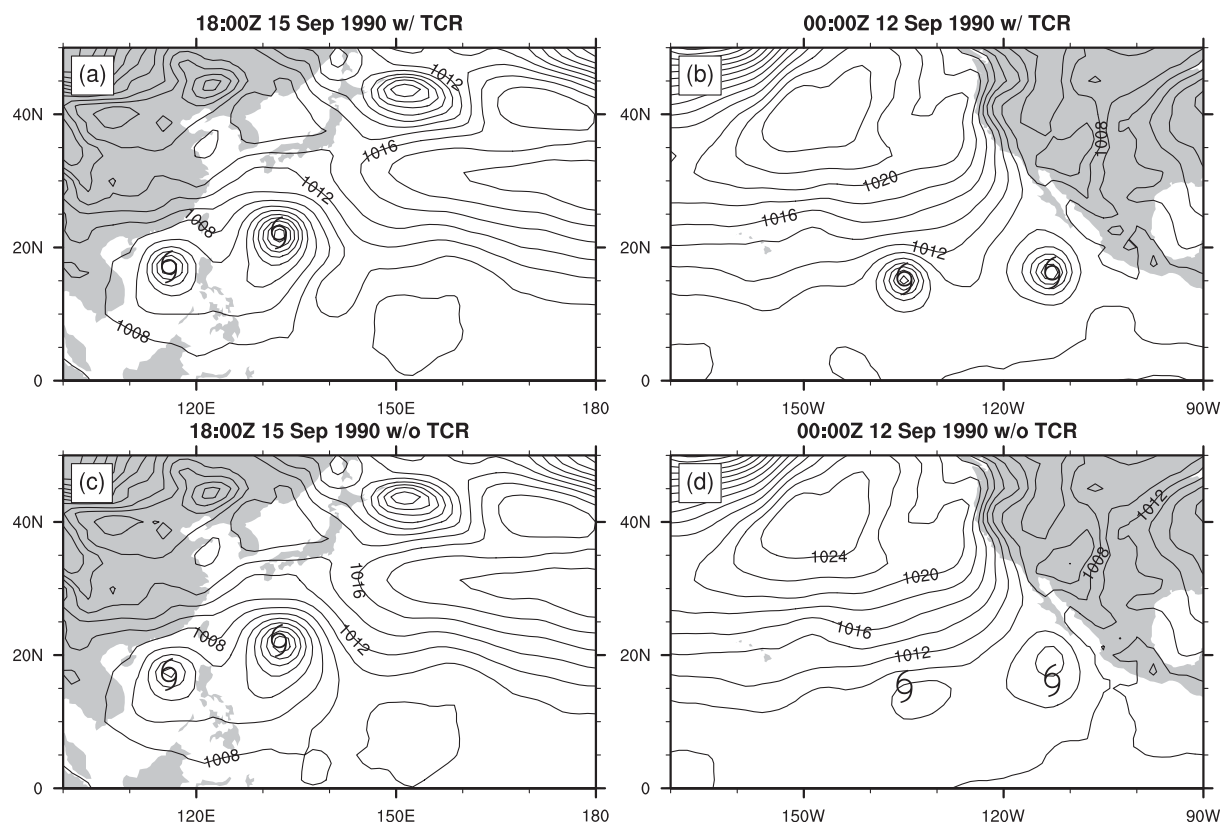


Fig. 10. Sea level pressure analyses with/without TCR data.

Sea level pressure [hPa] analyses in the western North Pacific (a, c) at 1800 UTC 15 September, 1990 and in the eastern North Pacific (b, d) at 0000 UTC 12 September, 1990 are shown. Upper and lower panels show results obtained with and without TC wind data, respectively. Contours intervals are 2 hPa. The maps include marked TC positions of Ed and Flo in (a, c) and Marie and Norbert in (b, d).

to the difference in the density of other observations in the different basins.

Figure 11 shows the TC detection rates in the WNP, ENP, and North Atlantic (ATL) basins in the JRA-25 and the ERA-40. The detection rate used in this analysis is defined as the percentage frequency of TCs analyzed in each reanalysis against the best track information. A detailed description of this detection method is given in Hatsushika et al. (2006). Although the rates depend on the variables used for detection and their criteria, JRA-25 marks much higher detection rates than ERA-40 in any basin. In fact, the detection rate in JRA-25 is close to 100% throughout the analysis period, while that for ERA-40 varies and is lower over the years.

The TCR data plays a key role in improving the analysis of the vertical structure of tropical cyclones. A vertical cross section of temperature anomaly around TC centers for each of the JRA-25 and the ERA-40 analyses is shown in a composite map (Fig. 12). In these analyses, TC centers are determined using the best track information in the tropical zone of 40S and 40N. The temperature anomaly is defined as the deviation from the zonal mean. Each TC is selected only when a cyclone has a local minimum of geopotential height at 1000 hPa within 7.5 degrees from the observed TC center. In the WNP, the characteristic warm core structure over the TC center is reproduced in both reanalyses (cf., Fig. 9 of Hawkins and Rubsam 1968). On the contrary, in the ENP the warm

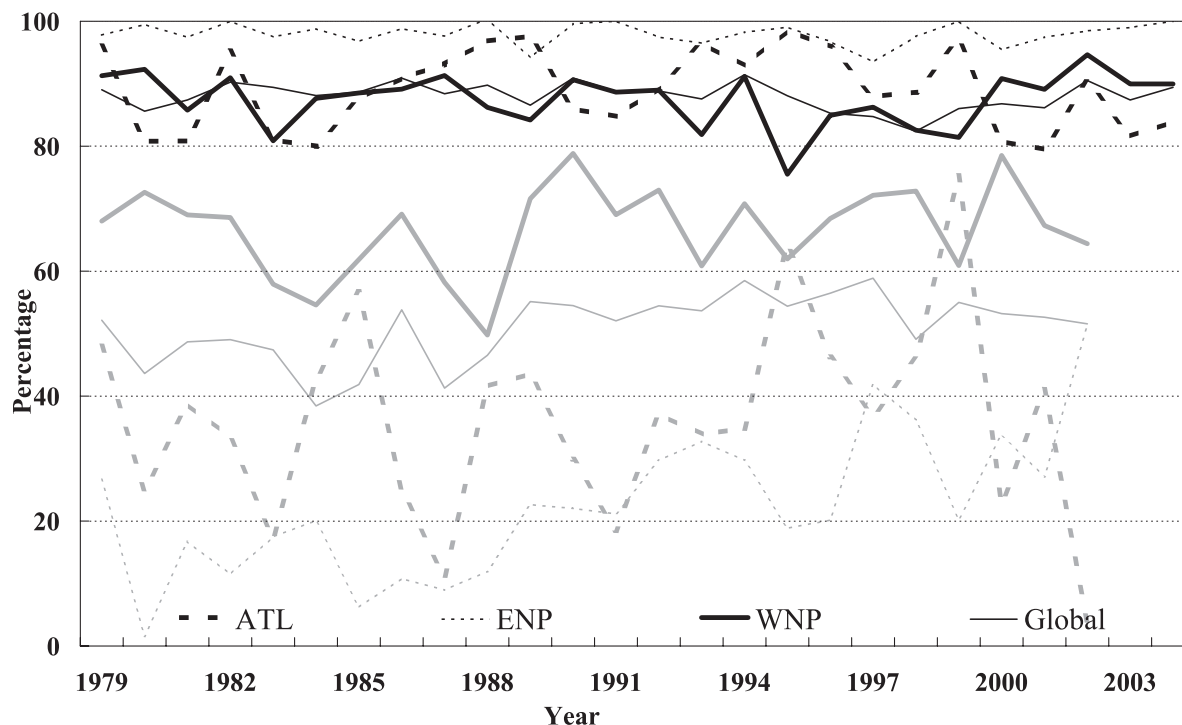


Fig. 11. TC representation rates [%] for JRA-25 (black) and ERA-40 (gray).

Only TCs located near the best track positions that have typical TC structures are selected.

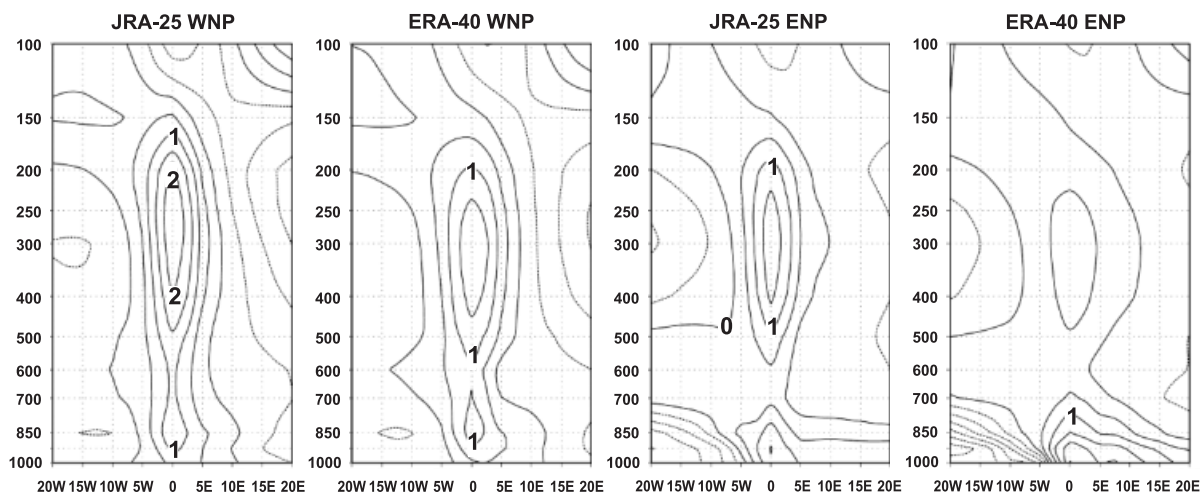


Fig. 12. Vertical cross section of the composite temperature anomaly [K] from the zonal average.

Included are all TCs analyzed between the equator and 40N for which the geopotential height minimum is located within 7.5 degrees from the best-track TC center on the 1000 hPa surface.

core is weak in the ERA-40 compared to the JRA-25. The peak level and horizontal scale of the warm core is reproduced well in JRA-25, as expected from the statistical TC structure.

4.5 Soil moisture

Soil moisture climatology in the JRA-25 land system (see 3.3) is described.

In the middle latitudes, soil moisture clima-

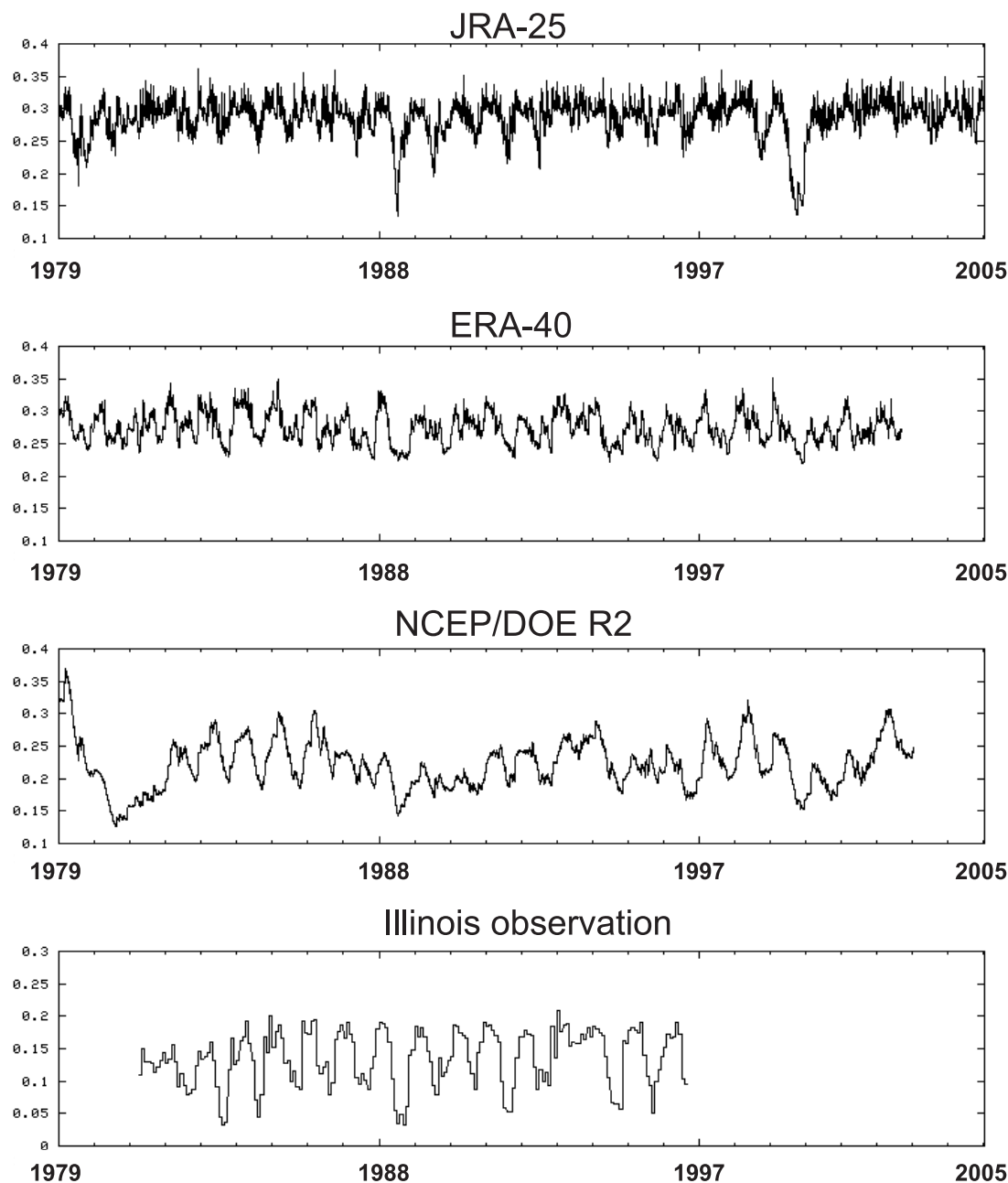


Fig. 13. Intercomparison of Illinois reanalyzed root-depth soil wetness and observations [fraction]. From top panel to bottom, JRA-25, ERA-40, NCEP-R2, and monthly observations (Hollinger et al. 1994) are shown. The serious dryness in 1988 is well reproduced in JRA-25.

tology is realistically represented. A comparison is made between soil moisture observation and reanalysis averaged over the state of Illinois in the United States, where some good observation is available from the Water and Atmospheric Resources Monitoring Program

(WARM) (Hollinger and Isard 1994). Intercomparison of Illinois root-depth soil wetness of reanalyses and observations is shown in Fig. 13. The dry soil associated with the draught in 1988 is well reproduced in JRA-25.

In an earlier stage of the JRA-25 operation,

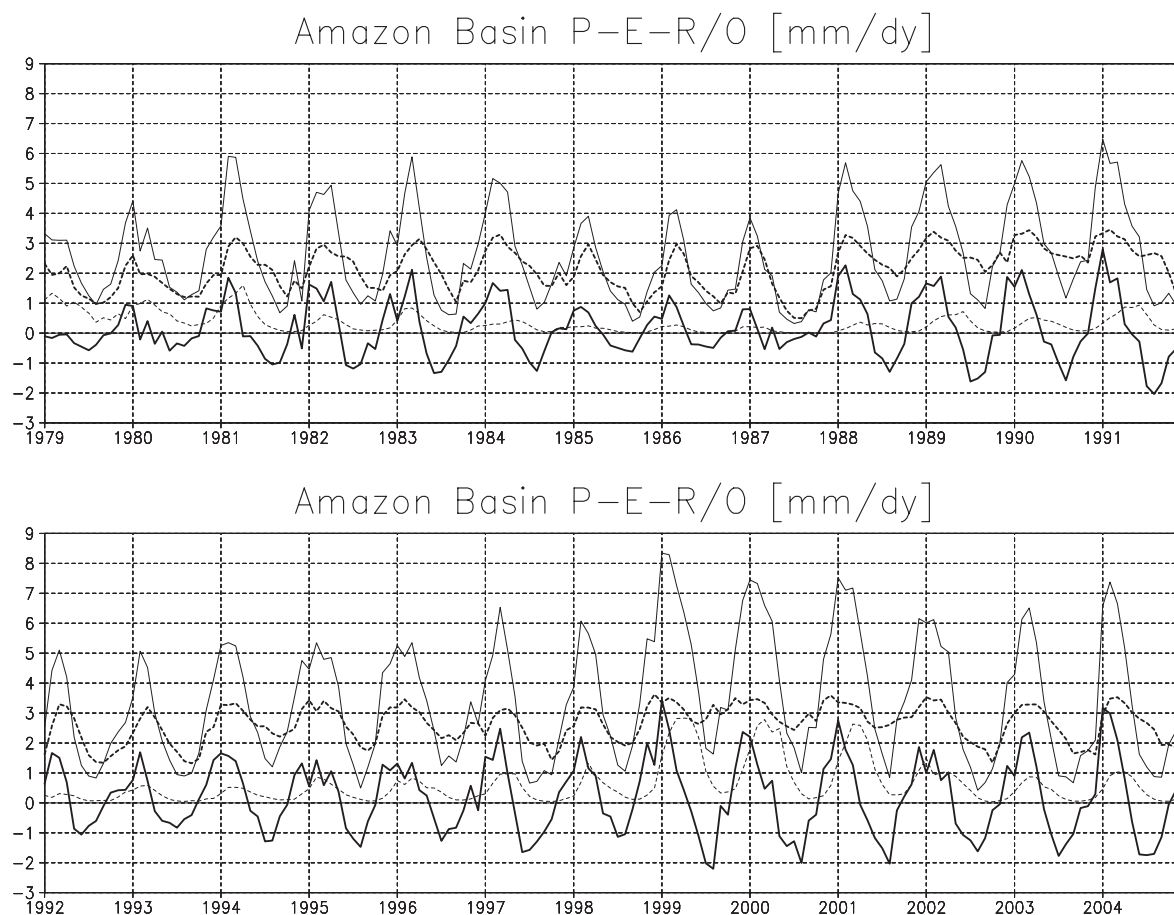


Fig. 14. Water Budget over Amazon Basin.

Precipitation (P: thin solid line), Evaporation (E: thick broken line), Surface Runoff (R/O: thin broken line), and their budget (P-E-R/O: thick solid line) over the Amazon Basin produced by JRA-25, all in [mm/day]. After the rainy season subsequent to the removal of two discrepant conventional station observations from 1987 to 1991 and 1998 onward, the Amazon water budget significantly improved.

unrealistic drying of soil moisture occurred over the Amazon River basin (Fig. 14). It was found that the local positive surface pressure analysis increment from a small number of station reports and an associated change in lower atmospheric circulation triggered the drift. The erroneous 83208 (Vilhena airport) station altitude of 652 m (correctly 612 m) before June 1996 enhanced the surface pressure departure. We successfully prevented the drying by discarding some surface pressure reports shown in Table 6. However another drying event occurred in the 2001–2002 rainy season, due to a large positive surface pressure increment caused by

other surface stations over the Amazon. These drying events might have been prevented by well-organized quality control on input surface pressure observations. Additionally, unrealistic weak dryness occurred in equatorial Africa in May 1998 and overestimation of precipitation and water vapor convergence in northern subtropical Africa (Sahel zone) are found in the first 3 years from 1979 to 1981. Regrettably, the drifts of land and atmospheric variables over the Amazon basin remain in the products. The Amazon River basin, as a vast inland tropical rain forest, is characterized by a strong land-atmosphere coupling. The difficulty of re-

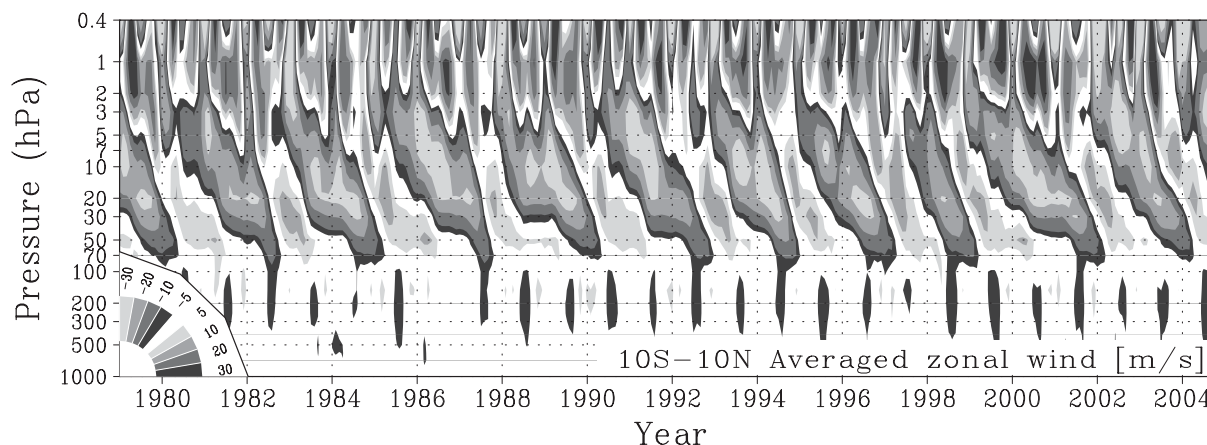


Fig. 15. Monthly mean zonal wind [m/s] in the tropical band 10S–10N as a function of pressure [hPa].

The wind speed range is shown in the bottom-left corner.

producing past realistic soil moisture and surface analysis over the Amazon in reanalyses was pointed out by Betts et al. (2004) and Betts et al. (2005). Improving soil moisture climate over the Amazon is a future task.

The drying problem in the Amazonian area might have affected large scale circulation in the tropics, such as Walker circulation and related phenomena. Further investigation is required to find out the extent of the problem.

4.6 Stratosphere

The vertical resolution of the JRA-25 analysis is as high around the tropopause and lower stratosphere as that in the ERA-40 analysis, and we expect that the stratospheric analysis of temperature and zonal wind is of good quality. Figure 15 shows zonal mean zonal wind averaged between 10S and 10N. The quasi-biennial oscillation (QBO) in the middle-to-lower stratosphere and the semi-annual oscillation (SAO) in the upper stratosphere are apparent in this figure and in a power spectrum density analysis (not shown). The phase and amplitude of the QBO and the SAO is almost the same as those represented by ERA-40 (cf., Fig. 22 of Uppala et al. 2004).

Annual variability of temperature at 20 hPa in the northern and southern polar regions is superimposed with their average and shown in Fig. 16. Features of the observed annual cycle

(cf., SPARC, 2002) are well represented at both poles.

The large-scale sudden warming events that occur in the winter-to-early springtime polar stratosphere, especially in the Northern Hemisphere, are properly analyzed. The occurrence of the stratospheric sudden warming events (SSWs) is defined as when the 20 hPa temperature averaged over the polar region from 60N to NP increases more than 10 K within one week and the averaged zonal wind there abruptly changes to the easterly wind. By applying this definition, 12 SSWs were detected in the JRA-25 reanalysis during the period between 1979 and 2000. Figure 17 shows zonal-mean temperature anomalies and zonal-mean zonal wind anomalies integrated polewards of 60N during the composite life cycle of these SSWs. The warm and easterly anomalies in the middle stratosphere propagate to the lower stratosphere, and the cold anomaly in the upper stratosphere follows the preceding warm anomaly. This feature is consistent with the theory by Matsuno (1971) and the similar analysis using NCEP/NCAR R1 reanalysis by Limpasuvan et al. (2004).

The value of mass stream function of JRA-25 at 100 hPa in boreal summer and winter is small compared to ERA-40 and more comparable to NCEP/NCAR R1 (Hamada and Iwasaki, personal communications). van Noije et al.

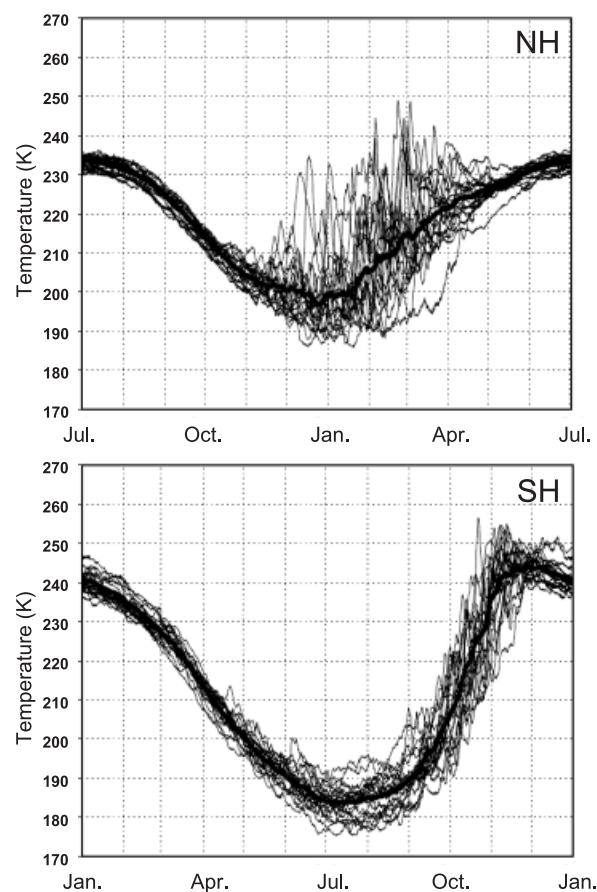


Fig. 16. Annual cycle of zonal mean 20 hPa temperature at 80°N (top) and 80°S (bottom). The black thin line denotes years from 1979 to 2000. The gray thick line denotes the climatological annual cycle for these years.

(2004) and Uppala et al. (2005) have reported a strong bias in the Brewer-Dobson circulation in ERA-40.

Although stratospheric temperature and wind fields in the JRA-25 are of high quality, stratospheric humidity does not compare well with observational data. The humidity estimated in JRA-25 is much drier than observations and decreases with time. The shortage in stratospheric water vapor in JRA-25 is mainly caused by 1) the lack of source due to missing stratospheric photochemistry including methane oxidation, and 2) no assimilation of the stratospheric water vapor. The usage of the Eulerian

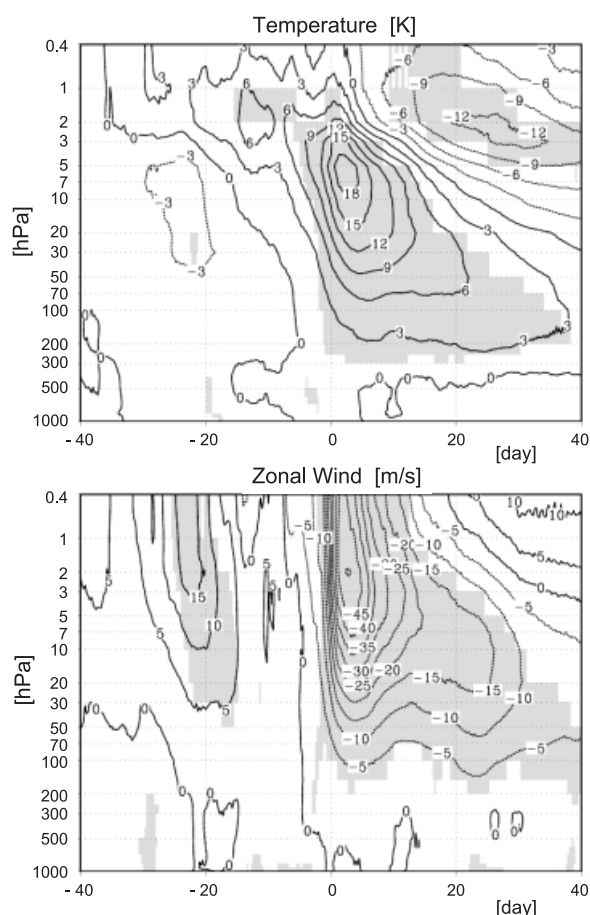


Fig. 17. Anomalous temperature and zonal wind during SSWs. Anomalous temperature (top; K) and zonal wind (bottom; m/s) in the polar region north of 60°N relative to the 22-year climatology during the composite life cycle of SSWs. Shading indicates areas with a 95% confidence level based on Welch's *t*-statistics.

spectral advection scheme may be a factor as well. Note that the low value of water vapor in the stratosphere does not harm radiation calculations in JRA-25, since the mixing ratio is assumed to be constant (2.5 ppm) for radiation process in the JRA-25 forecast model.

4.7 Surface temperature

The JRA-25 includes surface analysis separate from the three-dimensional variational analysis of the atmosphere. This surface analysis employs a two-dimensional optimum in-

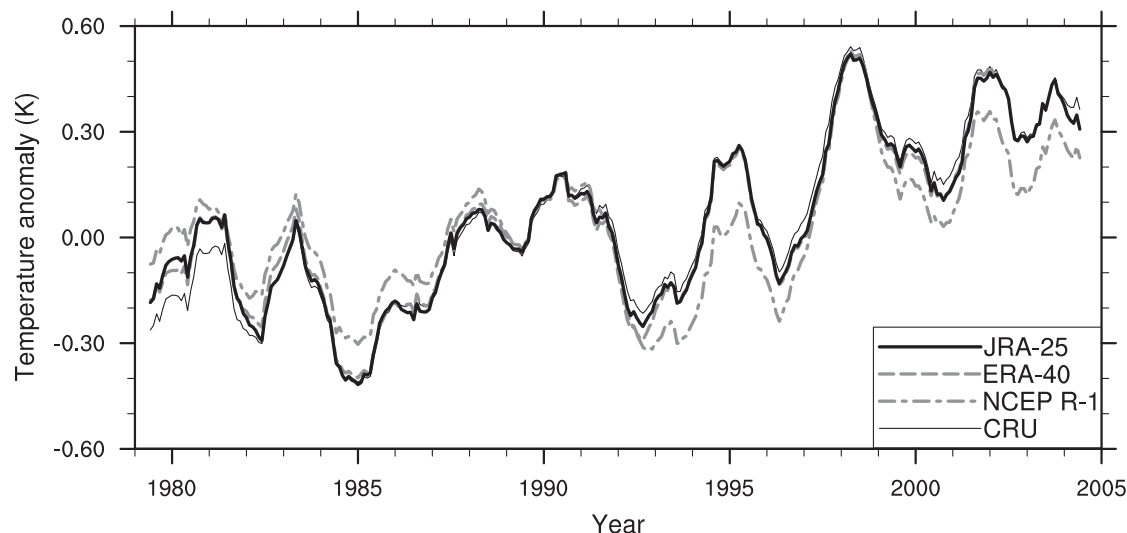


Fig. 18. Time-series of monthly surface air (2-m) temperature anomalies from JRA-25, ERA-40, NCEP-R1 and CRU data.

Anomalies are defined as deviations from the 1979–2001 climatology (1961–1990 for CRU). Gridded data are globally averaged with area weighting, over grid boxes for which CRU data exist, and a 12-month running mean is applied for smoothing. Values are adjusted to have zero mean over the period 1979–2001.

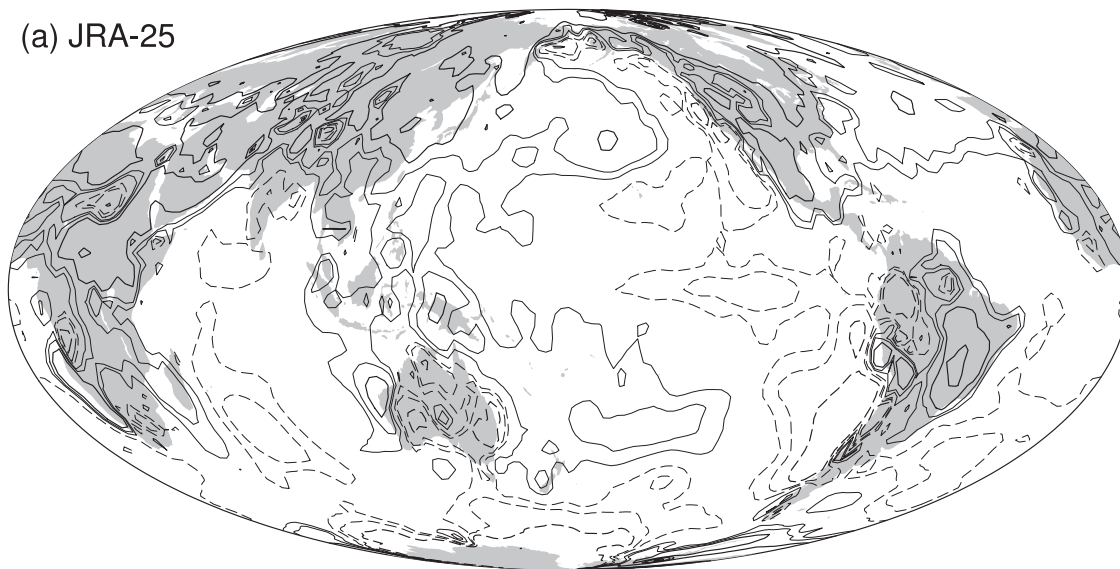
terpolation scheme that assimilates various surface observations with first-guess fields diagnostically obtained from upper-air first-guess fields (Tada 2000). This scheme is similar to that used in ECMWF reanalysis. To demonstrate the quality of the surface analysis, monthly mean 2-meter air temperatures are compared with ERA-40, NCEP/NCAR R1 and CRUTEM2v (hereafter CRU; Jones and Moberg 2003). The CRU dataset, a standard reference for climate change studies, contains temperature anomalies from 1961–1990 climatology in 5-degree grid boxes. Simmons et al. (2004) reported that the ERA-40 and CRU data match well, in particular after 1979, both for variability and trends.

Figure 18 shows time-series of the temperature anomalies averaged over data-existing CRU grid boxes. Anomalies are defined as deviations from 1979–2001 climatology for the re-analyses. The four time-series are almost identical with respect to interannual variability. It is also found that the four datasets have similar spatial distributions in any given year and month. With respect to a long-term warming trend, JRA-25, ERA-40 and CRU are almost

identical but the trend of NCEP/NCAR R1 is slightly smaller than the others. This result is consistent with Simmons et al. (2004). The interannual variations are further discussed in the next subsection. Although the JRA-25 temperatures are about 0.1 K higher than the CRU temperatures for a few years after 1979, differences between the JRA-25 and ERA-40 are negligible throughout the entire period.

When we include areas without CRU observations, there are relatively large differences between JRA-25 and ERA-40 with respect to long-term trend. These differences are mostly observed in mid- and high-latitudes in the Southern Hemisphere. Figure 19 shows geographical distributions of linear trends over the period of 1979–2001. Although the two re-analyses share a similar spatial distribution, some regional trends indicate different tendencies, typically in the Antarctic. On the whole, the surface warming trend is smaller in the JRA-25 than in the ERA-40. Possible factors affecting the differences include QC processes for surface observations, SST and sea ice boundary data, and first-guess fields from upper atmospheric analysis. In this context, further exami-

(a) JRA-25



(b) ERA-40

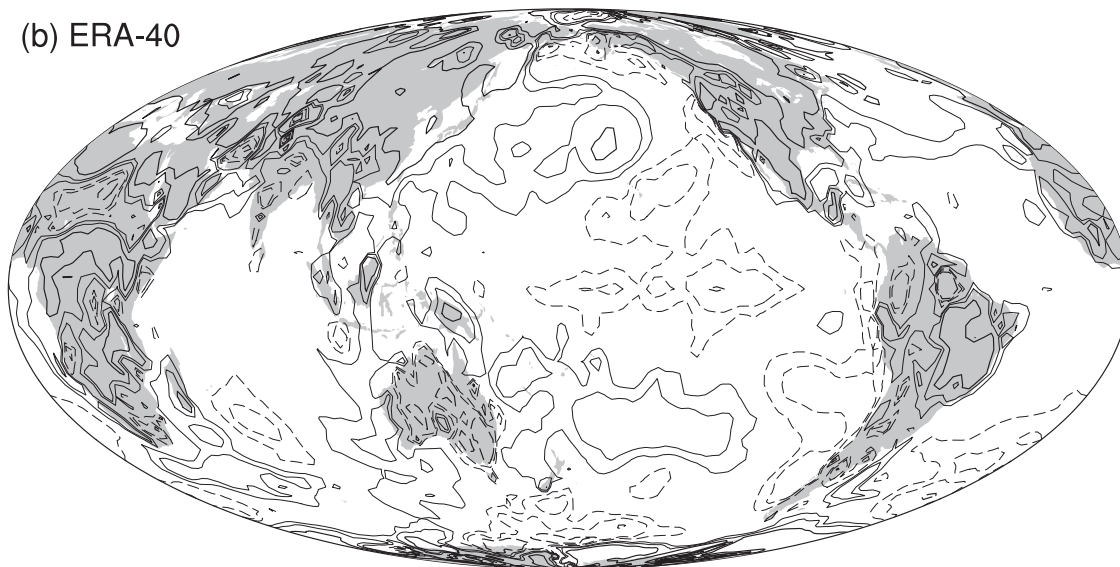


Fig. 19. Geographical distributions of linear trends for surface air temperature.

Geographical distributions of linear trends over the period of 1979–2001 for monthly surface air temperature anomalies from JRA-25 (a) and ERA-40 (b) are shown. Contours are drawn at plus/minus 0.1, 0.2, and 0.4 K/decade. Dashed contours denote negative values, and thick contours denote values of plus/minus 0.4 K/decade.

nation of the trend in COBE SST and its effects are very important.

4.8 Free atmospheric temperature

Figure 20 shows time-series of global-mean monthly temperature anomalies at 70 hPa and 500 hPa from JRA-25 and ERA-40. The time-

series of surface temperature are similar to that shown in Fig. 18. Although the two reanalyses indicate more noticeable differences in long-term tendencies at the upper levels than at the surface, they resemble each other with respect to characteristic interannual variations. The interannual variations at the 500-hPa level

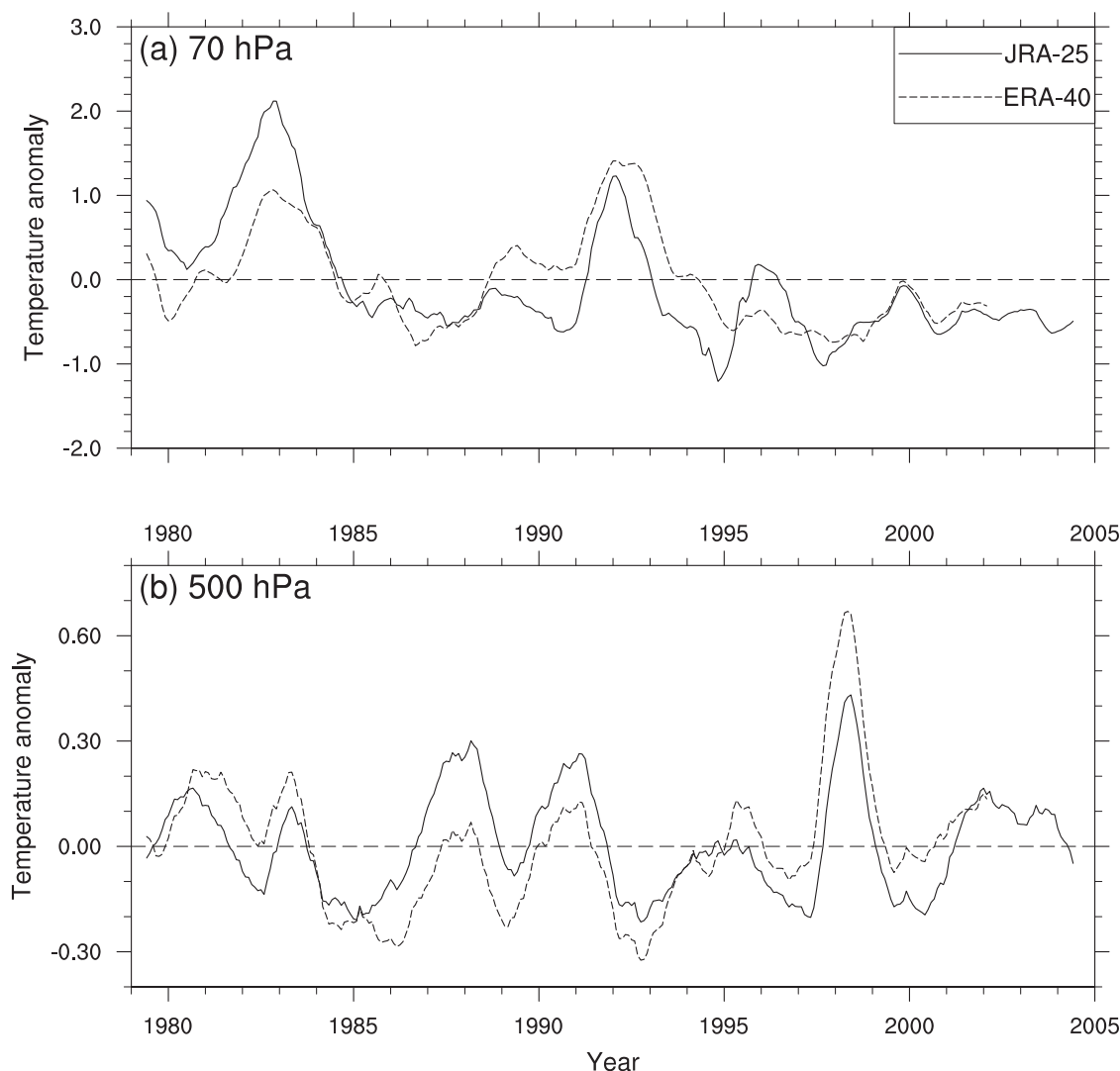


Fig. 20. Time series of global-mean free-atmospheric temperature anomalies [K].

Time series of global-mean monthly temperature anomalies at 70 hPa and 500 hPa from JRA-25 and ERA-40. A 12-month running mean is applied for smoothing. The anomalies are defined relative to 1979–2001 averages.

are similar to those at the surface, including particularly large positive anomalies in the period of the 1997–98 El Niño event. Other relatively large anomalies generally correspond to ENSO events. At the 70-hPa level representing the lower stratosphere, large positive anomalies around 1982 and 1991–92 are most striking. These periods correspond to the volcanic events of Mt. El Chichon and Mt. Pinatubo, respectively. Because volcanic eruptions lead to cooling in the troposphere, it is possible that

warming impacts of El Niño events in 1982–83 and 1991–92 are somewhat reduced in the 500-hPa temperature.

Uncertainties about the reanalysis trends mostly arise from changes in the satellite observing system (e.g., Basist and Chelliah 1997; Bengtsson et al. 2004c). Although Santer et al. (2004) reported that the ERA-40 matches reference data based on the MSU observations relatively well, these reference data also have considerable uncertainties on long-term trends

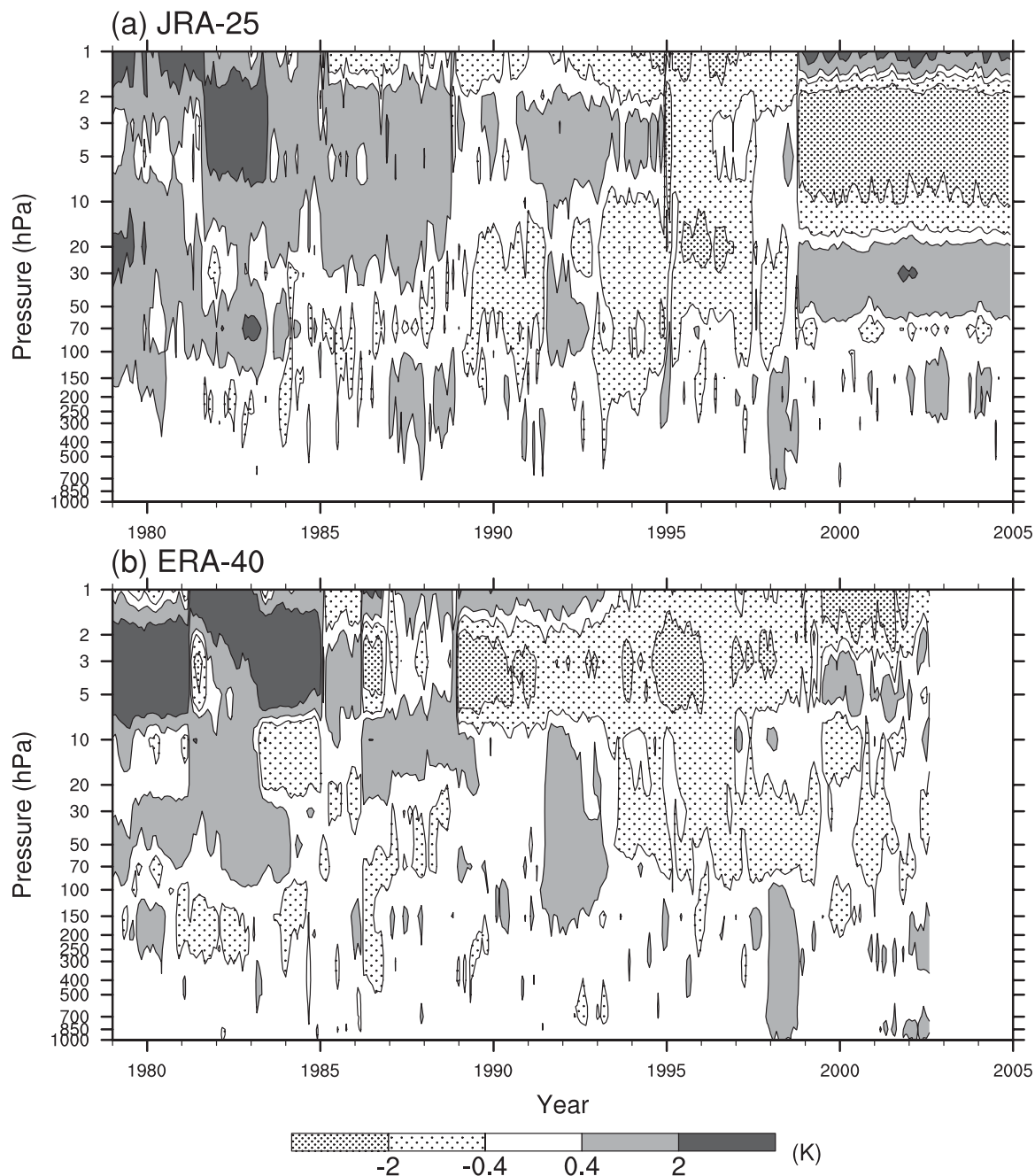


Fig. 21. Pressure-time distributions of global-mean monthly temperature anomalies from (a) JRA-25 and (b) ERA-40.

due to different post-processing (Mears et al. 2003; Christy et al. 2003). It is expected that the surface warming will be amplified in the upper tropical troposphere, under the assumption that a temperature profile follows approximate moist-adiabatic lapse rate (Santer et al.

2005). However, consistent temperature trends at upper troposphere are not observed among multiple reanalyses including the JRA-25.

Transition of satellites causes difficulties in adjusting inter-satellite differences of instrument properties. As shown in Fig. 21, global-

mean monthly temperature anomalies change discontinuously in the stratosphere. Most of such discontinuous changes in the JRA-25 occur at the time of satellite system changes, shown in Fig. 26. In particular, the impacts of TOVS-to-ATOVS transition in 1998 are large. Although similar discontinuous changes are observed in the ERA-40, changes after 1990 seem to be held small.

The JRA-25 QC system employs an adaptive scheme to correct bias by the series of TOVS satellites (TIROS-N to NOAA-14) to reduce their departures from first-guess fields. However, it is difficult to make bias corrections suitable for time-varying combinations of multiple satellites, intermittent missing observations, and temporal variations of the instrument characteristics, which inevitably affect the quality of analyses.

Since the JRA-25 forecast model has a relatively large bias in the stratosphere and upper troposphere as mentioned in 3.2, the background forecast field was not accurate enough to correct the observation bias. With such biases, sporadic missing observations possibly result in unrealistically sudden changes in analysis. This problem is particularly significant in January 1995 when the SSU observations were totally missing. As shown in Fig. 21, large changes prevail throughout the stratosphere in this period.

Further detail on how satellite soundings affect the quality of the JRA-25 is discussed in Sakamoto et al. (2006).

4.9 Comparison with upper air radiosonde observations in Japan

Analyzed temperatures and winds are the most basic in the reanalysis and need to be checked against high-quality independent observations. There are, however, virtually no independent observations. As an alternative verification, we compared reanalysis data with upper air observations in Japan and examine the mean and root mean square (RMS) differences. The mean analysis increments are used to measure the qualities of the observations, and 18 Japanese upper air stations are selected. Data to be compared are temperature and winds with mandatory levels from 1000 hPa to 20 hPa. Four sets of reanalysis data (JRA-25, ERA-40, NCEP/NCAR R1, and

NCEP/DOE R2) are interpolated to the same 2.5 degree horizontal grids and further linearly interpolated to each station location.

Figure 22 shows mean and RMS differences for the four reanalyses averaged from 1981 to 2001. Zonal wind differences below 300 hPa are small for all reanalyses, while they become larger above 300 hPa. JRA-25 has mean and RMS differences similar to ERA-40 in magnitude and smaller differences in radiosonde observations than NCEP/NCAR R1 and R-2 reanalyses. Meridional wind differences are similar to those for zonal wind, and JRA-25 differences are larger than those for ERA-40. JRA-25's temperature has a large negative bias above 100 hPa, close to two degrees at 30 hPa. This is due to the temperature bias of the forecast model in the stratosphere as described in 3.2. Below 100 hPa, mean and RMS temperature differences for JRA-25 are as small as those for ERA-40.

4.10 Snow depth analysis

Land surface processes are quite sensitive to the existence of snow; thus it is important to make consistent snow depth analysis for good land surface analysis. JRA-25 uses the digitized Chinese snow data and the snow coverage GPV data retrieved from SSM/I, which is likely to produce good snow depth analysis. To demonstrate the quality, the JRA-25 snow depth analysis is compared with a control experiment without using the Chinese and SSM/I data.

The digitized Chinese snow depth data contributed to improve snow depth analysis around the snow edges. Figure 23 is an example of analysis with observations. Many Chinese stations report zero snow depth. The difference of snow coverage is apparent around the snow edges. Snow covered areas spread unrealistically southward without the Chinese data. This is an example of midwinter, but when Siberian and Mongolian regions are covered by snow, the southward spread of the snow covered area occurs in other months.

Snow coverage was also improved by using the snow coverage GPV data retrieved from SSM/I over the SYNOP data-sparse areas, particularly during the snow accumulation and melting stages (spring and autumn). Even in data-sparse areas, land surface is covered by

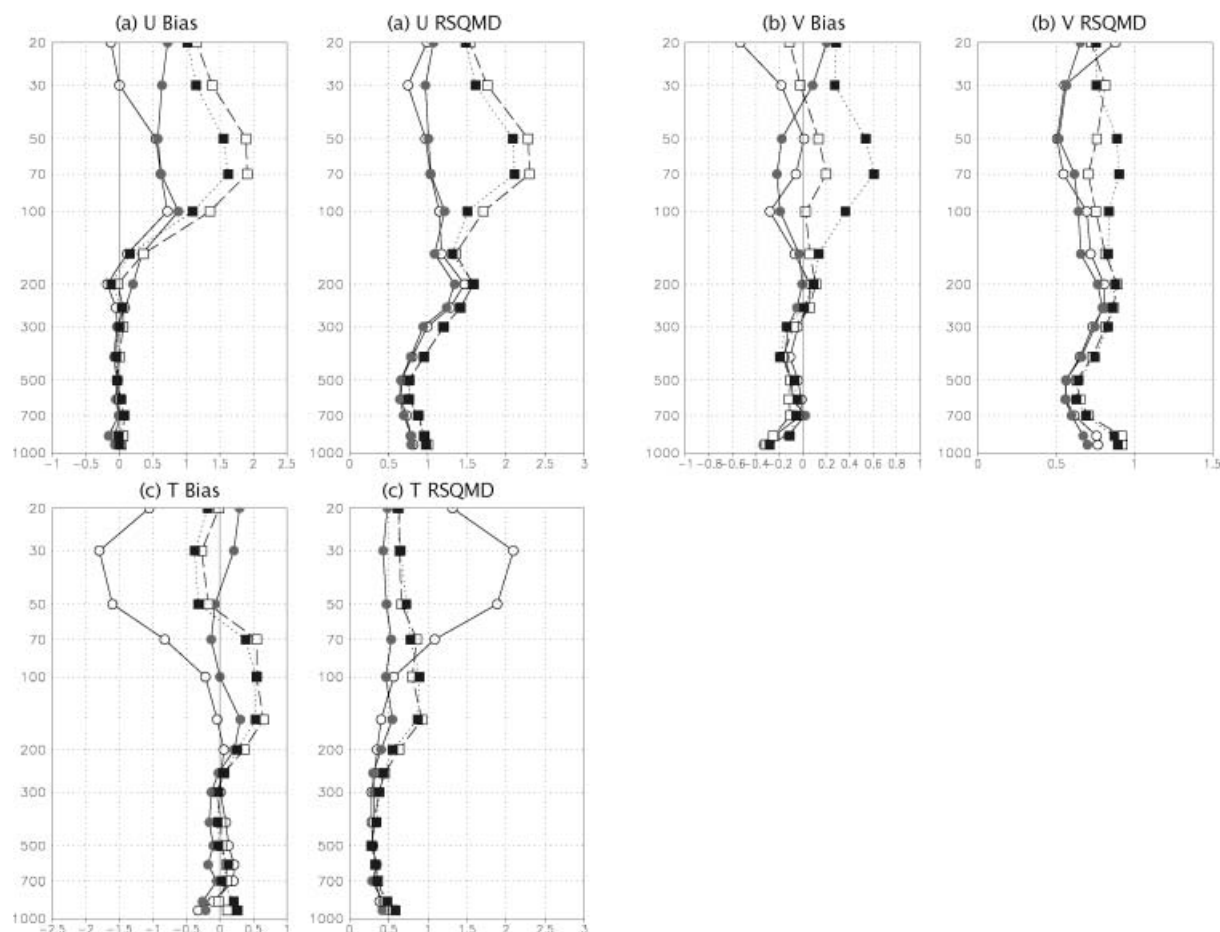


Fig. 22. Vertical profiles of mean and RMS differences from radiosonde observations.

Vertical profiles of mean and RMS differences from Japanese radiosonde observations for u -component wind [m/s] (a, b), v -component wind [m/s] (c, d) and temperature [K] (e, f) for JRA-25 (open circle), ERA-40 (closed circle), NCEP-R1 (open square) and NCEP-R2 (closed square) are shown.

snow throughout midwinter after the first snowfall in autumn.

4.11 Forecast score

The quality of reanalysis can be measured by the accuracy of a forecast made from a reanalysis as an initial condition. In JRA-25, 8-day forecasts were carried out every 5 days at 12UTC. Here root mean square error (RMSE) of geopotential height at 500 hPa (Z500) is taken as a forecast score. Scores of JRA-25 and the historical JMA operational models are compared. The JMA global model (GSM) has been operational since March 1988, while a northern hemisphere model was operational before then.

The resolution of the first GSM was T63L16. It was increased to T106L21, T213L30, T213L40 and TL319L40 in November 1989, March 1996, March 2001 and February 2005, respectively. The 2.5 latitude-longitude degree GPs are used for calculating the forecast scores throughout the period.

Figure 24 shows the 24-hour forecast scores. While scores of the operational model are worse in the past, scores of JRA-25 are mostly consistent, even though in the 1980s they were slightly worse than after the 1990s. The JRA-25 score in 1979 is equivalent to the operational score around 2000 to 2002 in the northern hemisphere and to the score of 1996

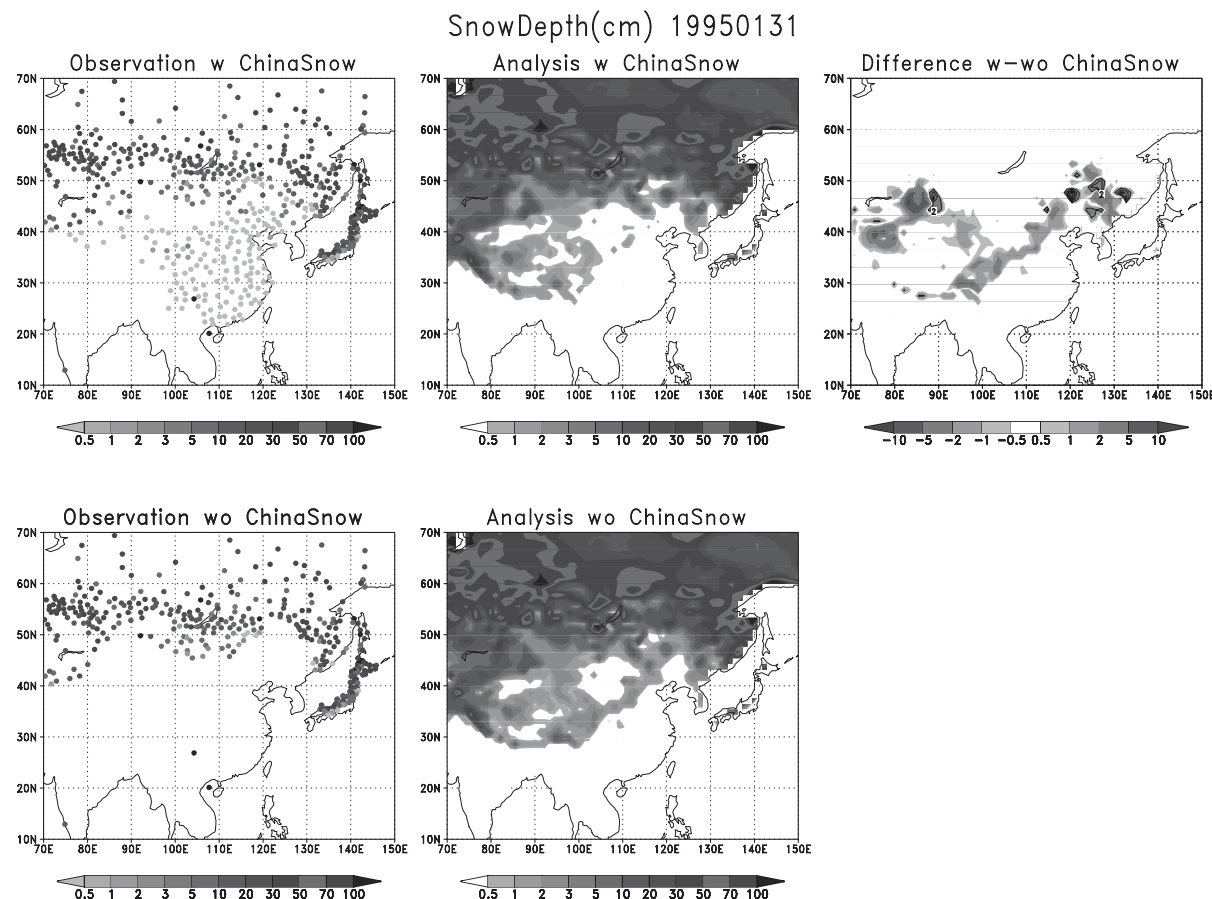


Fig. 23. Impact of digitized Chinese SYNOP snow depth data (Onogi et al. 2005).

Left and middle panels indicate SYNOP snow depth observation and snow depth analysis, respectively. Top panels are for JRA-25, bottom panels for a control experiment without Chinese snow data. Top right panel shows the difference in snow analysis between JRA-25 and the control experiment. Significant differences can be found near the boundary separating snow-covered and no-snow areas.

in the southern hemisphere. The score of the southern hemisphere after 1999 was significantly improved, owing to the assimilation of ATOVS data. For the latest year, 2004, the JRA-25 score is about the same as the operational ones. In JRA-25, the latest statistics of background error for 3D-Var and assimilation of SSM/I PW were implemented in advance, even though these were still being developed at the time. The advance implementation of the developments seemed to contribute to similar forecast scores to the latest operational forecast skill, despite using a lower resolution than that of the operational model. The consistent

forecast scores prove the consistent quality of JRA-25.

4.12 Other deficiencies

In this subsection, other deficiencies found in JRA-25 are described.

The forecast model used in JRA-25 is a spectral model; conversion to and from grid point representation is done by the time integration process. The Gibbs phenomenon due to spectral conversion causes ripple effect in water vapor related variables. This causes unrealistic distribution of cloud amounts in the region of small saturated water vapor pressure under low tem-

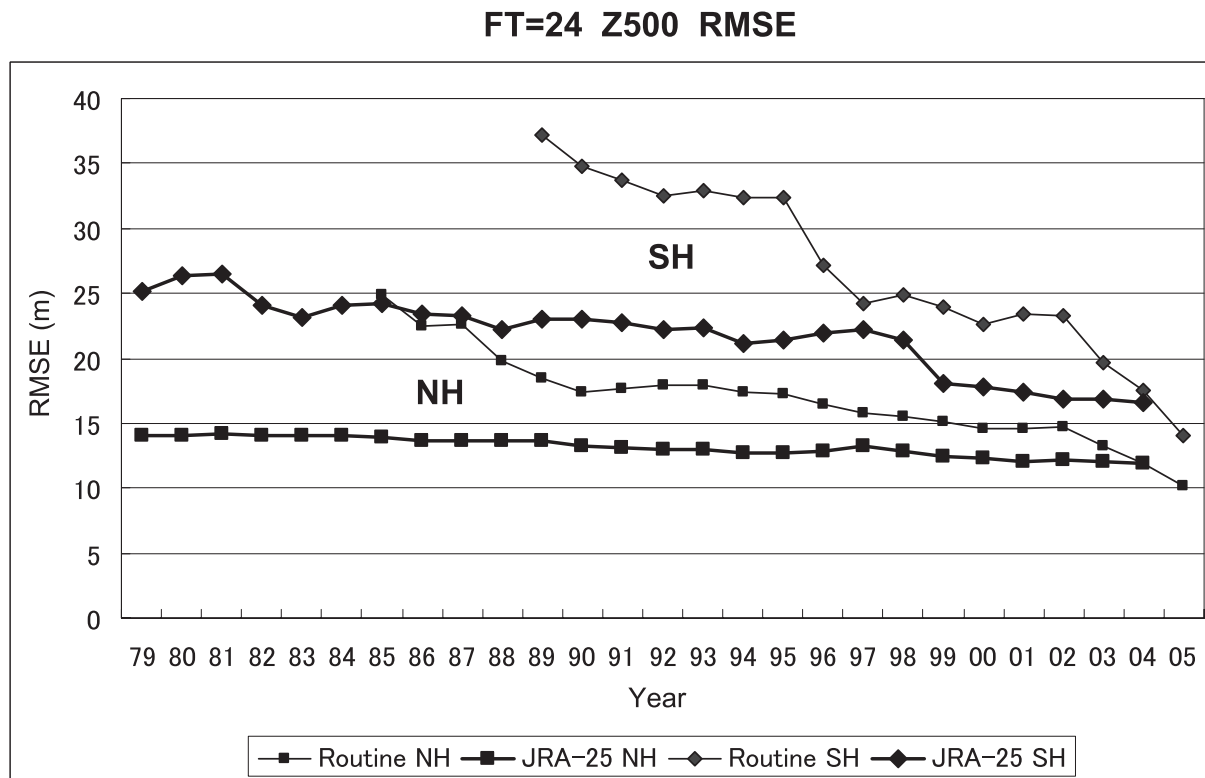


Fig. 24. Forecast scores of JRA-25 and the JMA operational system.

RMSE of geopotential height at 500 hPa (Z500) of 24-hour forecasts for JRA-25 and JMA operations (Routine) are shown.

perature in the polar region. Similar ripple patterns are also found near the Andes mountains in South America.

In addition to the numerical problem in the forecast model, there were several technical problems associated with the sea-ice and snow data. Unexpected erroneous open sea along the coast of the Arctic Ocean was found for the years from 1979 to 1981 and from 1991 to 1993.

Some of the available snow data were inadvertently not used in the snow depth analysis during certain periods. From January 1979 to August 1983, a large number of snow depth data in Siberia were omitted due to a technical problem. As a result, analyzed snow depths in Siberia prior to the winter 1982–1983 are too small. Furthermore, two problems were found in the snow observational data. One is in the region of the former Soviet Union during 1984 to 1990, when the frequency of snow reports

was less than other years, causing snow depths to increase suddenly (every 10 days) in the analysis during the snowfall season in autumn. The other problem is a spot of snow coverage in the mid-latitude due to noise caused by a problem in the SSM/I retrieval method.

4.13 Change of observations and their influences

Since JRA-25 is a reanalysis from 1979, sounder data from polar orbital satellites and wind data from geostationary satellites are available throughout the reanalysis years. Consequently, JRA-25 did not suffer serious observation changes from the no-satellite era to the satellite era. However, historical observational data for the 26 years of JRA-25 varied to a large extent, both in data type and amount, and the discontinuities caused by the observation changes were inevitable. Here discontinuity means sudden changes and gaps of aver-









Table 6. JRA-25 observation history, mainly for conventional data.

Date	Stream	Event	Comment
1979.01.01	STB	Start of Stream B	Less snow depth in Siberia due to the (*1) problem.
		SYNOP snow depth data at 00, 06 and 12UTC were not used because of a technical problem (*1 see 4.10). Small open areas in sea ice along coast of polar region due to a program bug (*2 see 4.12).	
1982.01.01		Bug fix of the sea ice open area problem (*2 fixed)	Sea ice distribution became normal.
1983.09.01		All the SYNOP snow depth data used normally (*1 fixed)	Snow depth analysis became normal.
1984.05.14		JMA archived observational data have been used since this date.	
1986.10.12		Station 83208 in Amazon was blacklisted (*3 see 4.5).	Drying problem in Amazon basin was relaxed.
1986.11.25		Station 83264 in Amazon was blacklisted (*3 see 4.5).	Drying problem in Amazon basin was relaxed.
1990.12.31		End of Stream B	
1991.01.01	STA	Start of Stream A	
		Station 83208 and 83264 in Amazon were not blacklisted (*3 appeared again).	Drying problem in Amazon basin was enhanced again.
		Small open areas in sea ice along coast of polar region (*2 appeared again).	
1994.01.01	STA recalculation-1	Use of reprocessed GMS-AMV was stopped because of defects in the data since this date (*4 see 4.14 and Fig. 27). Operational GMS SATOB wind have been alternatively used since this date.	
		Correction of sea ice interpolation method for the sea ice open area problem. Bug fix of the sea ice open area problem (*2 fixed again).	Sea ice distribution became normal.
1994.01.19		Stations 83208 and 83264 in Amazon were blacklisted (*3 fixed again). Station 63402 in Africa was blacklisted (*5 see 4.5).	Drying problem in Amazon basin was relaxed again.
1995.04.24		ERS scatterometer sea surface wind has been available since this date.	
1997.01.01		Corrected GMS-AMV (ver.2) has been used since this date. Use of GMS-SATOB data were stopped (*4).	

Table 6 (continued)

Date	Stream	Event	Comment
1998.11.01		Change from TOVS to ATOVS from this date.	Apparent temperature discontinuity in the upper stratosphere (see 4.8)
1999.12.31		End of recalculation-1 of Stream A	
2000.01.01	STA recalculation-2	Start of recalculation-2 of Stream A (see 4.14)	
		New version of SST and sea ice using an improved retrieval algorithm have been used since this date.	Little significant changes of SST and sea ice distribution are caused by the improvement.
2002.02.01	STA	Back to STA original calculation (not recalculations, see 4.14).	Small discontinuities are found in some parameters between the recalculation of TCR Y2K and main stream A.

Detailed history of SSM/I, TOVS/ATOVS and GMS-AMV are displayed in Figs. 25, 26 and 27.

Satellite	Assimilated Period	Assimilated period				
		1980	1985	1990	1995	2000
DMSP F08	1987.06.25 - 1993.09.13					
DMSP F10	1991.02.11 - 1997.11.14					
DMSP F11	1991.12.03 - 2000.05.16					
DMSP F13	1995.05.03 - 2004.12.31					
DMSP F14	1997.05.22 - 2004.12.31					
DMSP F15	2000.02.23 - 2004.12.31					
Problem*: Part of data were not used due to array size limitation in the PW assimilation.	1979.01.01-1997.09.10 2002.02.01-2002.07.11					

*If data from more than 3 satellites are available, many of the PW data of the third and fourth satellite datasets were not assimilated.

Fig. 25. History of assimilating SSM/I PW data.

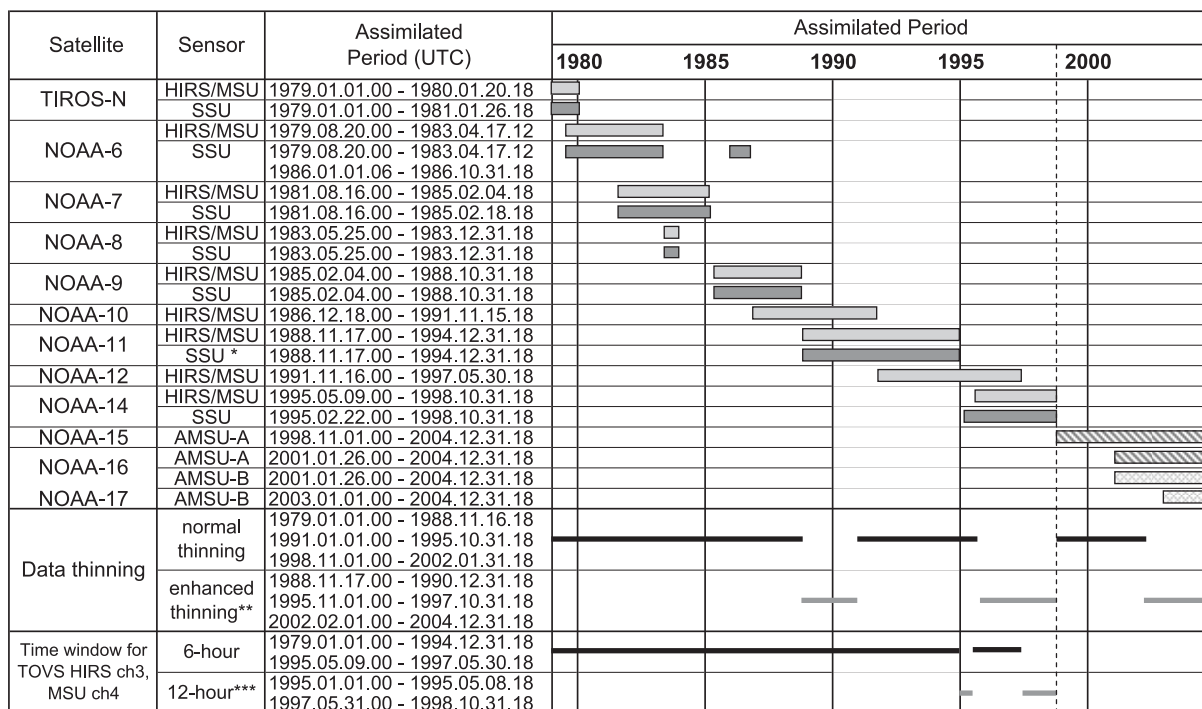
aged field found in time-series monitoring. If a discontinuity occurs at the same time as an observation change, it is probably caused by the observation change. Changes of assimilated observational data in JRA-25 were summarized in Table 6, Figs. 25, 26 and 27.

Significant changes are caused by the changes of satellite data. Character of precipitation changed on 25 June 1987, when SSM/I PW data became available. Temperatures in the stratosphere changed significantly on 1

November 1998 when TOVS data was replaced with ATOVS data. Users should pay attention to the discontinuities caused by these observation changes.

4.14 Unrealistic changes by technical problems

JRA-25 was conducted in two separate streams, one for the first half from 1979 to 1990 (STB) and a second stream for the latter half from 1991 to 2004 (STA). Ideally the pro-



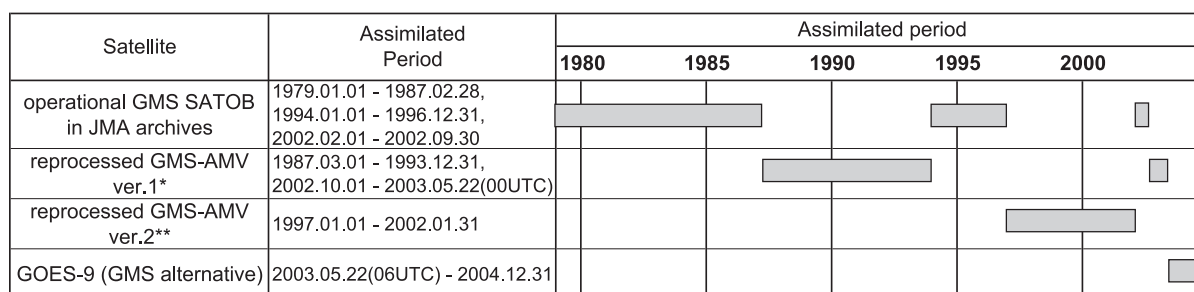
* NOAA-11 SSU ch2 was assimilated from 1991.01.01.00 to 1995.10.31.18

** TOVS (For the stratospheric TOVS channels)

** ATOVS (AMSU-A: data interval from 2.5deg. to 3.0deg., AMSU-B: 1.8deg. to 2.0deg.)

*** Time windows for SSU ch1,2,3 and HIRS ch2 are 12-hour throughout the period.

Fig. 26. History of assimilating TOVS and ATOVS data.



* Many low quality data were included with reprocessed GMS-AMV ver.1 data from 1994.01.01 to 2002.09.30.

** The problem was fixed and reprocessed again as reprocessed GMS-AMV ver.2.

Fig. 27. History of assimilating GMS wind data.

duction should be done with one continuous stream throughout the period, but we had to separate streams because of the limitation of time and computer resources. The streams are summarized in Fig. 28. While most of the variables transition smoothly between the two

streams, some discontinuities are found in some variables as listed in Table 7. Furthermore, two recalculations were performed to fix problems caused by data quality. One is due to the low quality GMS-AMV data from January 1994 to December 1999; the other is due to

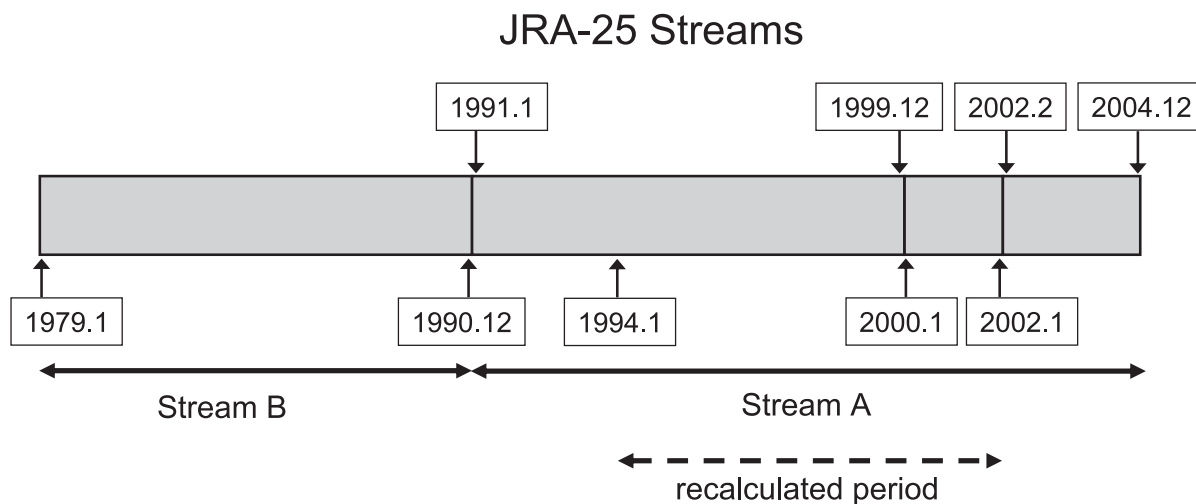


Fig. 28. JRA-25 Streams.

Processing streams for JRA-25 are shown. The first stream covers 1979 to 1990; the final stream covers 1991 to 2004. The periods Jan. 1994 to Dec. 1999 and Jan. 2000 to Jan. 2002 were re-calculated. There may be discontinuities in some variables at the boundaries of the streams.

Table 7. Discontinuities of global averaged variables caused by separated streams between Stream B and Stream A (Dec. 1990–Jan. 1991).

Parameter	level	gaps	comment
Air temperature [K]	1000 to 300 hPa 250 to 150 hPa 100 to 50 hPa 30 to 10 hPa 7 to 3 hPa 2 hPa 1 hPa 0.4 hPa	under 0.1 −0.1 to −0.3 +0.2 to +0.6 −0.1 to −0.6 +0.4 to +0.8 −0.2 +1.0 +0.6	
Geopotential height [m]	1000 to 250 hPa 200 to 150 hPa 100 hPa 70 to 20 hPa 10 to 7 hPa 3 and 2 hPa 1 hPa 0.4 hPa	ignorable −5 −10 ignorable −10 ignorable +10 +40	
Specific humidity (10^{-6} kg/kg)	1000 to 200 hPa 150 hPa 100 hPa stratosphere	ignorable +0.7 +0.9 no product gaps found	depend on regions
Soil wetness at surface Soil wetness [fraction] Soil temperature [K] Water equivalent snow depth [m]		−0.015 +0.1 −0.037	decrease to half of depth

Y2K problem of TCR data from January 2000 to January 2002. There are small discontinuities associated with those restarts at the beginning of January 2000 and February 2002, respectively. Users should also pay attention to these unrealistic changes.

5. Conclusion and future prospect

The JRA-25 reanalysis dataset was produced by the JMA operational assimilation system with modification for historical observational data. The TOVS radiance data assimilation method, the land surface analysis with feedback mechanism, use of SST and sea ice based on the COBE dataset, and use of three-dimensional daily ozone profiles were specially developed for JRA-25. The JRA-25 used data not used in the other reanalyses, such as more comprehensive conventional data archives supplied by overseas organizations, TCR, reprocessed geostationary satellites AMV data, and digitized snow data from historical printed records. In particular, assimilation of TCR is unique and not found in other reanalyses.

JRA-25 has many advantages compared to the other reanalyses: (a) 6-hour forecast total precipitation compares well with observations having the best correlation scores among reanalyses, especially in the tropics. (b) TCs are properly analysed owing to the assimilation of TCR. (c) Low-level cloud along the subtropical western coast of continents is forecast very well. (d) The digitized Chinese SYNOP snow depth data and snow coverage data retrieved from SSM/I improved the snow analysis. On the negative side, the following problems were found: (e) In the Amazonian region, the soil is relatively dryer and the amount of precipitation is less than in the other reanalyses. (f) There are discontinuities in the time series of global mean temperature in the stratosphere.

JRA-25 is expected to be a reliable reference for large scale tropical circulation and climatological tropical cyclone research. JRA-25 also is expected to provide reliable high-quality reference data for research on historical meteorological events, in which long term trend is not essential.

For the operational use of the JRA-25 at JMA, a new climate normal value was created and is being used as a basic reference data for climate monitoring services. Reanalysis data, produced

by the model whose characteristics are the same as the seasonal forecast model, can provide consistent initial fields and verification data for the seasonal forecast and hindcast. Consequently the reanalysis data greatly contributes to the development of the seasonal forecast model.

JRA-25 is transitioned to JCDAS, which takes over JRA-25 after 2005 on a real time basis using the same assimilation system. JCDAS is used in JMA's operational climate services and provides data similar to, and in addition to, JRA-25 data for researchers.

The main purpose of reanalysis is to produce a consistent high-quality long-term analysis dataset using the latest numerical analysis and prediction system. So far, however, the available reanalyses still have many problems due to changes in the observing system. For future reanalysis, it is essential to use feedbacks from a previous reanalyses to overcome these problems. Onogi (2000) investigated the long-term performance of radiosonde observations in ERA-40. Onogi detected histories of radiation correction and suggested that it was impossible to extract small signals from large amplitude daily and annual changes just by investigating raw observational data. Haimberger (2005) and Haimberger (2006) proposed a bias correction method of historical radiosonde observations using feedback information, such as departures and the result of QCs of ERA-40. Detailed signals can be extracted and detected correctly from the feedback information.

Uncertainties about the reanalysis trend mostly arise from changes in the satellite observing system. As shown in Figs. 25, 26 and 27, satellite data changed many times during the reanalysis years both in quality and quantity. Further investigation of data from each satellite and further improvement of assimilation technique is required to produce an analysis that provides good estimate of trend. The most crucial process for better trend analysis is the bias correction of satellite radiance data. Dee (2005) proposed an adaptive bias correction technique taking bias estimation into a variational method. It eliminated discontinuities. Furthermore, it is found to be more effective for historical data than for real time data because changes of data quality can be detected beforehand.

Table 8. Member list of JRA-25 Advisory Committee.

Chairman	Honorary Prof. Tomio Asai Prof. Toshiki Iwasaki Prof. Masahide Kimoto Prof. Toshio Koike Prof. Hisashi Nakamura Prof. Kimio Hanawa Prof. Tetsuzo Yasunari Dr. Koichi Kurihara Dr. Tadashi Tsuyuki Dr. Akira Noda Dr. Koki Maruyama	Tokyo University Tohoku University CCSR, Tokyo University Tokyo University Tokyo University Tohoku University Nagoya University CPD/JMA NPD/JMA CRD/MRI/JMA CRIEPI	(2005.4–) (2003.11–) (2004.4–)
(Former members)	Dr. Shingo Osano Dr. Masato Sugi Dr. Nobuo Sato Dr. Hajime Nakamura Dr. Hiroki Kondo Dr. Takayo Matsuo Dr. Takashi Aoki	CPD/JMA CPD/JMA NPD/JMA NPD/JMA CRD/MRI/JMA CRD/MRI/JMA CRD/MRI/JMA	(2001.4–2002.3) (2002.4–2005.3) (2001.4–2002.3) (2002.4–2003.10) (2001.4–2002.3) (2002.4–2003.3) (2003.4–2004.3)

From the data assimilation system as a whole, more in-depth validation of the performance of the forecast model is required. The forecast model used in JRA-25 has some serious problems, such as large temperature bias in the stratosphere and dry bias in the Amazon basin. We are sure that research using JRA-25 will benefit both users and producers of reanalysis data. We will continue making efforts to improve the models to overcome the problems found in JRA-25.

We also believe that it is essential to improve all the components of the analysis system and also develop a system that enables us to use feedbacks from the previous reanalyses. In this regard, it is important to encourage international collaboration and the exchange of experience and information.

Acknowledgement

JRA-25 operated as a joint research project between JMA and CRIEPI and was supported by many staffs and researchers.

The JRA-25 advisory committee was organized with Dr. Tomio Asai as a chairman, and other authoritative professors listed in Table 8. The advisory committee gave us much appropriate advice at every stage of the project and gave directions for progress.

Research on water circulation using JRA-25 was done under the research project “Establishment of Informatics of Earth Water Circulation,” directed by Dr. Toshio Koike, funded from Special Coordination Funds for Promoting Science and Technology by Ministry of Education and Technology (MEXT).

Dr. Koki Maruyama of CRIEPI monitored the progress and the funding for the project.

The supercomputer Fujitsu VPP5000 of CRIEPI was used as the main computer for JRA-25 calculation. Special thanks are due to Mr. Hisashi Teramoto of Denryoku Computing Center for programming assistance.

Dr. Roy Jenne of NCAR has made a great effort for many years and generated a consistent historical conventional observation dataset. All the producers and users of the reanalysis should appreciate his great contribution. No reanalysis could be done without his efforts. Mr. John Woollen of NCEP supplied the historical observational data in their archives via the Internet at the first stage of JRA-25 project. This made our preparation work smooth. ECMWF supplied ERA-40 observational data as used in their reanalysis project. Mr. Keith Fielding of ECMWF worked hard for several months to prepare the data for our project. Reprocessed AMV data of METEOSAT-2 satellite were sup-

plied by EUMETSAT. SSM/I radiance brightness temperature data were supplied by NCDC. Dr. Michael Fiorino of PCMDI/LLNL (currently at NHC) kindly supplied TCR data and the software for producing the data. Dr. Manabu Yamanaka of Kobe University supplied Indonesian radiosonde data. Chinese snow depth data were digitized under the research project "Water Resource and its Variability in Asia in the 21st Century," funded from Special Coordination Funds for Promoting Science and Technology by MEXT.

Dr. Adrian Simmons, Mr. Sakari Uppala, Dr. Per Kållberg, Ms. Angeles Hernandez, Mr. Sami Saarinen and Mr. John King Gibson (retired) of ECMWF gave us appropriate advice from their experience with ERA at many stages of JRA-25 project.

Dr. Masao Kanamitsu (currently at Scripps Institution of Oceanography) and Dr. Robert Kistler of NCEP (retired) gave us useful advice.

The release of our product was done with the help of GrADS (the Grid Analysis and Display System, Doty and Kinter III(1995)) supported by COLA/IGES and "wgrib" program developed by Dr. Wesley Ebisuzaki of NCEP.

In the JRA-25 projects framework, an "Evaluation Group" was organized and many researchers participated. They gave us useful feedback from the early stage of our project. This information contributed to check and correct the JRA-25 reanalysis system.

Mr. Takashi Maki of JMA produced three-dimensional daily ozone data for JRA-25, and Mr. Hiroto Kitagawa of JMA made experiments to apply the ozone data and adjust the radiation scheme for JRA-25. Mr. Toshiyuki Kurino worked on quality control of SSM/I data in the first half of the project. Many JMA staff from the Climate Prediction Division, Meteorological Satellite Center, Numerical Prediction Division, Atmospheric Environmental Division and Administration Division of Global Environment and Marine Department supported the JRA-25 project in many aspects: obtaining funds for observational data from overseas institutes, preparing observational data, tuning and modification of the operational NWP system for JRA-25, executing experiments, making statistics, and assisting in many other tasks.

We greatly appreciate all the researchers and staffs who supported and advised JRA-25.

Appendix A

JRA-25 standard products

This appendix describes the JRA-25 standard products, which are available through the Internet.

(1) Outline

The JRA-25 archive is categorized as shown in Table A1. Most of the categories are generated directly by each operation of the 4-Dimensional Data Assimilation (4DDA) cycle, which consists of an atmospheric model forecast, 3D-Var data assimilation, and land analysis. Some additional categories are derived subsequent to the assimilation.

The categories named with "anl_" are "analysis" which contain atmospheric, snow, and land analysis. The categories named with "fcst_" are "forecast" which contain atmospheric and land forecast, and many additional forecast variables calculated by physical schemes. Since it is a 6-hour forecast, forecast variables can be affected by spin-up problems in the model integration. The categories named with "ges_" are "first guess" for data assimilation. Basically they include the same variables as those in the 6-hour dynamical forecast, while some variables are converted to fit the assimilation module. The analysis increment, which is modification of a field by data assimilation, can be evaluated easily by comparing the categories "anl_" and "ges_".

In addition to the model spin-up problem, physical conservation laws are not generally satisfied in 4DDA, since new atmospheric information from observational data is regularly supplied to the model through the analysis increments.

The model variables are represented by 8-byte (double precision) floating-point numbers. The outputs are 4-byte reals converted to 12-bit GRIB (WMO GRIdded Binary) format for public use. The time interval of the products is 6 hours. Moisture fields in the stratosphere are excluded for public use due to the lower analysis quality. The total data volume of the 6-hourly GRIB format products is about 8 tera-bytes (TB) for the entire 26-year period. The largest category contains the 3-dimensional atmospheric model diagnostics (fcst_phy3m)

Table A1. Category of the JRA-25 product available through the Internet.

Name	Grid type*	Level**	Field***	Explanation
anl_p	LL125	P23	6h, Mn	pressure level analysis
anl_p25	LL25	P23	6h, Mn	pressure level analysis
anl_chipsi	LL125	P23	6h, Mn	pressure level analysis (additional)
anl_chipsi25	LL25	P23	6h, Mn	pressure level analysis (additional)
anl_mdl	Gaus	M40	Mn	model level analysis
anl_z	LL125	P23	6h, Mn	zonal-averaged pressure level analysis
anl_z25	LL25	P23	6h, Mn	zonal-averaged pressure level analysis
anl_isentrop	Gaus	M40	Mn	Isentropic surface analysis
anl_isentrop25	LL25	T20	6h, Mn	Isentropic surface analysis
anl_land	Gaus(mask)	G3	6h, Mn	land analysis
anl_land25	LL25(mask)	G3	6h, Mn	land analysis
anl_snow106_mdl	Gaus(mask)	—	6h, Mn	snow depth analysis
anl_snow25	LL25(mask)	—	6h, Mn	snow depth analysis
fcst_phy2m	Gaus	—	6h, Mn	2-dimensional diagnostics
fcst_phy2m25	LL25	—	6h, Mn	2-dimensional diagnostics
fcst_phy3m	Gaus	M40	Mn	3-dimensional diagnostics
fcst_phy3m25	LL25	P23	Mn	3-dimensional diagnostics
o3tot_phy3m25	LL25	—	6h	total column ozone
fcst_phyland	Gaus(mask)	G3	6h, Mn	land physics monitor
fcst_phyland25	LL25(mask)	G3	6h, Mn	land physics monitor
fcst_mdl	Gaus	M40	Mn	model level 6-hour forecast
ges_p	LL125	P23	6h, Mn	pressure level first guess
ges_p25	LL25	P23	6h, Mn	pressure level first guess
ges_mdl	Gaus	M40	Mn	model level first guess
lfpl_topo.gr	Gaus	—	Const	topography
typr.dat	Gaus	—	Const	vegetation index
mask25.jma_t106.gr	LL25	—	Const	land sea mask
soil.t106	Gaus	G3	Const	soil variables

* Gaus: T106 Gaussian grid (320×160), LL125: Latitude-Longitude grid in 1.25 degree (288×145), LL25: Latitude-Longitude grid in 2.5 degree (144×73)

** P23: Pressure 23 level, M40: Model 40 level, T20: Isentropic 20 level, G3: Soil 3 level (see description in (2))

*** 6h: 6-hourly field, Mn: monthly field, Const: constant field

Table A2. Level suffixes and symbols attached to variable names.

Level suffix	Explanation	Symbol	Explanation
sfc	surface level	none	Instantaneous value at a given time
prs	mandatory pressure level	*	Averaging during the 6-hour integration
col	total column vertically integrated	+	Accumulation during the 6-hour integration
hbl	hybrid vertical level		
tht	isentropic		

whose total size is 3.3TB. All the available variables are listed in Table A4.

(2) Spatial resolution

Both forecast and assimilation atmospheric output is provided on the model grid using 320 longitudinal and 160 latitudinal Gaussian grid points, corresponding to a triangular wavenumber 106 spectral truncation (T106), and vertically 40 hybrid layers with the top at 0.4 hPa (see Table A3). The variables on the model grid are vertically interpolated to 23 pressure levels (1000, 925, 850, 700, 600, 500, 400, 300, 250, 200, 150, 100, 70, 50, 30, 20, 10, 7, 5, 3, 2, 1, and 0.4 hPa), and horizontally to a 2.5-degree or 1.25-degree latitude-longitude grid. For the primary products a conservative interpolation is adopted only in the horizontal plane. Soil moisture only is provided for three soil layers and the soil layer thickness is not homogeneous, depending on soil depth and type. Isentropic surface fields are derived from the model grid analysis on 20 isentropic levels as 270, 280, 290, 300, 310, 320, 330, 340, 350, 360, 370, 380, 390, 400, 425, 450, 475, 550, 650, and 750(K).

Note that in general, data at and near the uppermost levels around 0.4 and 1 hPa are less reliable than those at lower levels because some adjustments are introduced to suppress reflection of pseudo-energy at the top of the model.

(3) Temporal resolution and file name convention

Since the 4DDA is performed in 6-hourly cycles, the basic temporal resolution is 6 hours. The only exception is the snow analysis (anl_snow_md106), which is updated at 18UTC in daily intervals and is applied to the land anal-

ysis for the next day. No extended forecast products are supplied. There are three types of products related to time averaging: instantaneous fields (snapshot), time-averaged fields, and fields which are accumulated over a 6-hour model integration (see Table A2 for notation). Times appended to file names for analysis and first-guess products correspond to Coordinated Universal Time (UTC), and those for forecast products denote times after 6-hour integration. For example, the file "fcst_phy2m.2004010112" contains instantaneous, averaged, and accumulated forecast variables, which are integrated to 12UTC, averaged and accumulated from 06 to 12UTC on January 1st, 2004, respectively.

(4) Primary products

The following products are generated primarily in each 4DDA cycle.

i) Atmospheric analysis

A limited number of indispensable surface variables are added to the 3-dimensional atmospheric model-grid analysis (anl_md1). After spatial interpolation, pressure level analyses are generated on a 1.25-degree and 2.5-degree latitude-longitude grid (anl_p and anl_p25, respectively).

ii) First guess

From the 6-hour forecast, model-grid first guess (ges_md1) is generated and interpolated to the first-guess pressure levels (ges_p and ges_p25). Most of the variables of the model-grid first guess (ges_md1) are identical to the 6-hour model-grid forecast (fcst_md1).

iii) Land process

The snow depth analysis (anl_snow106_md1), the land forecast (fcst_phyland) and the land analysis (anl_land) are supplied in the T106

Gaussian grid. In the JRA-25 land model, soil moisture only is predicted for three vertical soil layers, while soil temperature is provided for a single total soil layer. The three soil layer thickness and the porosity are fixed values depending on soil types.

iv) 2-dimensional diagnostics

The 2-dimensional diagnostics (fcst_phy2m) include diagnostics from the atmospheric model forecast and prescribed boundary conditions on the Gaussian grid. Variables are calculated as an average over the 6-hour interval ending at the time or instantaneous values at the time (UTC) indicated in the file name. COBE SST and sea ice are included.

v) 3-dimensional diagnostics

The 3-dimensional diagnostics (fcst_phy3m) include diagnostics from the atmospheric model integration and prescribed boundary conditions on the Gaussian grid. Variables are calculated as the same way as for the 2-dimensional diagnostics.

(5) Secondary products

For the convenience of users, additional products are derived from the primary fields.

i) Additional variables for the pressure level analysis

The above-mentioned pressure level analysis in (4) i) does not include sufficient variables for users. Vorticity, divergence, velocity potential, stream function, vertical pressure velocity (ω), and surface pressure are available on a 1.25-degree and 2.5-degree latitude-longitude grid (anl_chipsi and anl_chipsi25) computed from the model-grid analysis.

ii) Isentropic surface analysis

The isentropic surface analysis is a powerful tool for analyzing atmospheric chemical trans-

port and diffusion. From the model grid analysis, vertical interpolation to twenty isentropic surfaces (see (2) in this Appendix) is made. With other basic analysis variables, Ertel's potential vorticity is calculated after the dry convective adjustment to remove possible vertical inversion.

Two categories on T106 Gaussian grid (anl_isentrop) and 2.5-degree latitude-longitude grid (anl_isentrop25) are produced.

iii) Zonal-mean pressure-level analysis

Zonal-mean fields of the atmospheric pressure-level analysis fields (anl_p and anl_p25) are calculated, taking into account the model topography, as anl_z and anl_z25, respectively.

iv) 2.5-degree horizontal interpolation for the Gaussian grid variables

The diagnostics and land analysis are interpolated from the Gaussian grid to a 2.5-degree latitude-longitude grid. These are fcst_phy2m25, fcst_phy3m25 (with vertical pressure-level interpolation), anl_land25, fcst_phyland25 and anl_snow25.

v) Total column ozone

The prescribed 3-dimensional ozone concentration in fcst_phy3m is vertically integrated to provide the total column ozone on a 2.5-degree latitude-longitude grid (o3tot_phy3m25).

(6) Monthly individual layer and variable product

For users requiring only a limited selection of variables, all variables available on the 2.5-degree latitude-longitude grid are separated into individual datasets containing a 6-hourly time series for a period of one month of a single variable at a single layer. The total number of such variables is 517.

Table A3. Parameters defining each hybrid half level: $\text{Phf} = A(i - 1/2) + B(i - 1/2) \times \text{Ps}$, ($i = 1, 40$). Ps is surface pressure and Pf is pressure of each full level when Ps = 1000 hPa.

[illegible]

Table A4. Variables in each category.

Name	Field type [unit]	Number of levels
anl_p, anl_p25		
HGTprs	Geopotential height [gpm]	23
TMPprs	Air temperature [K]	23
SPFHprs	Specific humidity [kg/kg]	12
DEPRsfc	Dew point depression [K]	8
UGRDprs	Zonal wind [m/s]	23
VGRDprs	Meridional wind [m/s]	23
CWATprs	Cloud water content [kg/kg]	12
PRMSLmsl	Pressure reduced to mean sea level [hPa]	1
TMPsfc	Surface (2 m) air temperature [K]	1
SPFHsfc	Surface (2 m) specific humidity [kg/kg]	1
DEPRsfc	Surface (2 m) dew point depression [K]	1
UGRDsfc	Surface (10 m) zonal wind [m/s]	1
VGRDsfc	Surface (10 m) meridional wind [m/s]	1

anl_chipsi, anl_chipsi25		
RELDprs	Relative divergence [$10^{-6}/s$]	23
RELVprs	Relative vorticity [$10^{-6}/s$]	23
STRMprs	Stream function [$10^{-6} \text{ m}^2/s$]	23
VPOTprs	Velocity potential [$10^{-6} \text{ m}^2/s$]	23
VVELprs	Pressure vertical velocity [Pa/s]	23
PRESsfc	Surface pressure [Pa]	1
RELDsfc	Surface relative divergence [$10^{-6}/s$]	1
RELVsfc	Surface relative vorticity [$10^{-6}/s$]	1
STRMsfc	Surface stream function [$10^{-6} \text{ m}^2/s$]	1
VPOTSfc	Surface velocity potential [$10^{-6} \text{ m}^2/s$]	1

anl_mdl		
HGThbl	Geopotential height [gpm]	40
TMPhbl	Air temperature [K]	40
SPFHhbl	Specific humidity [kg/kg]	28
UGRDhbl	Zonal wind [m/s]	40
VGRDhbl	Meridional wind [m/s]	40
VVELhbl	Pressure vertical velocity [Pa/s]	40
CWATHbl	Cloud water content [kg/kg]	40

Table A4 (continued)

DISTsfc	Model surface height [m]	1
PRESsfc	Surface pressure [Pa]	1
TMPsfc	Surface (2 m) air temperature [K]	1
SPFHsfc	Surface (2 m) specific humidity [kg/kg]	1
RHsfc	Surface (2 m) relative humidity [%]	1
UGRDsfc	Surface (10 m) zonal wind [m/s]	1
VGRDsfc	Surface (10 m) meridional wind [m/s]	1
PWATcol	Precipitable water [kg/m ²]	1
UWVcol	Column total of zonal water vapor flux [kg/m/s]	1
VWVcol	Column total of meridional water vapor flux [kg/m/s]	1

anl_z, anl_z25		
HGTprs	Geopotential height [gpm]	23
TMPprs	Air temperature [K]	23
SPFHprs	Specific humidity [kg/kg]	12
CWATprs	Cloud water content [kg/kg]	12
UGRDprs	Zonal wind [m/s]	23
VGRDprs	Meridional wind [m/s]	23
VVELprs	Pressure vertical velocity [Pa/s]	23
PRESsfc	Surface pressure [Pa]	1
PRMSLmsl	Pressure reduced to mean sea level [Pa]	1
TMPsfc	Surface (2 m) air temperature [K]	1
SPFHsfc	Surface (2 m) specific humidity [kg/kg]	1
UGRDsfc	Surface (10 m) zonal wind [m/s]	1
VGRDsfc	Surface (10 m) meridional wind [m/s]	1

anl_isentrop, anl_isentrop25		
BVF2tht	Sqaure of Brunt-Vaisala frequency [1/s ²]	20
HGTtht	Geopotential height [gpm]	20
MNTSFtht	Montgomery stream function [m ² /s ²]	20
POTsfc	Surface potential temperature [K]	1
SPFHtht	Specific humidity [kg/kg]	14
TMPtht	Temperature [K]	20
UGRDtht	Zonal wind [m/s]	20
VGRDtht	Meridional wind [m/s]	20
VVELtht	Pressure vertical velocity [Pa/s]	20
PVORtht	Potential vorticity [PVU = 10 ⁻⁶ m ² /s · K/kg]	20

Table A4 (continued)

anl_land, anl_land25		
TSGsfc	Ground temperature [K]	1
SOILWhbl	Soil wetness at level 1(deep), 2(root) and 3(shallow) [fraction]	3
TSCsfc	Canopy temperature [K]	1
SOILTcol	Soil temperature [K]	1
SNWEsfc	Water equivalent snow depth [m]	1

anl_snow106_md1, anl_snow25		
SNOWD	Surface snow depth [m]	1

fest_phy2m, fest_phy2m25		
CPRATsfc+	6-hourly convective precipitation rate [mm/day]	1
CSDLFsfc*	Clear sky downward long wave flux at surface [W/m^2]	1
CSDSFsfc*	Clear sky downward solar flux at surface [W/m^2]	1
CSULFtoa*	Clear sky upward long wave flux at top [W/m^2]	1
CSUSFsfc*	Clear sky upward solar flux at surface [W/m^2]	1
CSUSFtoa*	Clear sky upward solar flux at top [W/m^2]	1
CWATcol+	Total cloud column water [kg/m^2]	1
DISTsfc	Model Surface height [m]	1
DLWRFsfc*	Downward long wave radiation flux at surface [W/m^2]	1
DSWRFsfc*	Downward solar radiation flux at surface [W/m^2]	1
DSWRFtoa*	Downward solar radiation flux at top [W/m^2]	1
FGLUsfc*	Zonal momentum flux by long gravity wave [N/m^2]	1
FGLVsfc*	Meridional momentum flux by long gravity wave [N/m^2]	1
FGSUsfc*	Zonal momentum flux by short gravity wave [N/m^2]	1
FGSVsfc*	Meridional momentum flux by short gravity wave [N/m^2]	1
FRQCsf*	Frequency of cumulus precipitation [%]	1
FRQPsf*	Frequency of precipitation [%]	1
HCDC*	High level cloud cover [%]	1
ICECsfc*	Ice concentration (ice = 1; no ice = 0) [1/0]	1
LCDC*	Low level cloud cover [%]	1
LHTFLsfc*	Latent heat flux [W/m^2]	1
MCDC*	Mid level cloud cover [%]	1
LPRATsfc+	6-hourly large scale precipitation rate [mm/day]	1
PRESsfc	Surface pressure [Pa]	1
PRMSLmsl*	Mean Surface pressure reduced to mean sea level [Pa]	1

Table A4 (continued)

PRMXsfc	Maximum hourly precipitation during 6 hours [mm/hour]	1
PWATcol	Precipitable water [kg/m ²]	1
SPFHMsfc*	Mean surface specific humidity [kg/kg]	1
RHsfc	Surface relative humidity [%]	1
SFCRsfc	Surface roughness [m]	1
SHTFLsfc*	Sensible heat flux [W/m ²]	1
SPFHsfc	Surface (2 m) specific humidity [kg/kg]	1
SPFHhbl	Specific humidity at the lowest model level [kg/kg]	1
SRWEQsfc+	6-hourly snowfall rate water equivalent [kg/m ² /day]	1
TCDCcol*	Total cloud cover [%]	1
TMAXsfc	Surface (2 m) air maximum temperature during 6 hours [K]	1
TMINsfc	Surface (2 m) air minimum temperature during 6 hours [K]	1
TMPsfc	Surface (2 m) air temperature	1
TMPPhbl	Temperature at the lowest model level [K]	1
TMPMsfc*	Mean surface (2 m) air temperature [K]	1
TTHMcol*	Column total of diabatic heating [W/m ²]	1
UFLXsfc*	Zonal momentum flux by friction [N/m ²]	1
UGRDsfc	Surface (10 m) zonal wind [m/s]	1
UGRDhbl	Zonal wind at lowest model level [m/s]	1
ULWRFsfc*	Upward long wave radiation flux at surface [W/m ²]	1
ULWRFtoa*	Upward long wave radiation flux at top [W/m ²]	1
UGRDMsfc*	Mean surface (10 m) zonal wind [m/s]	1
USWRFsfc*	Upward solar radiation at surface [W/m ²]	1
USWRFtoa*	Upward solar radiation at top [W/m ²]	1
UWVcol*	Column total of zonal water vapor flux [kg/m/s]	1
VFLXsfc*	Meridional momentum flux by friction [N/m ²]	1
VGRDsfc	Surface (10 m) meridional wind [m/s]	1
VGRDhbl	Meridional wind at lowest model level [m/s]	1
VGRDMsfc*	Mean surface (10 m) meridional wind [m/s]	1
VTUcol*	Column total of covariance between temperature and zonal wind [K*Pa*m/s]	1
VTVcol*	Column total of covariance between temperature and meridional wind [K*Pa*m/s]	1
VWVcol*	Column total of meridional water vapor flux [kg/m/s]	1
WSMXsfc	Maximum surface wind during 6 hours [m/s]	1
WSMXhbl	Maximum surface wind at the lowest model level during 6 hours [m/s]	1
WTMPsfc	Sea surface temperature [K]	1

Table A4 (continued)

fcst_phy3m, fcst_phy3m25		Gaus	LL25
ADVHRhbl*	Advective heating rate [K/day]	40	23
ADVMRhbl*	Advective moistening rate [kg/kg/day]	40	23
ADVUAhbl*	Advective zonal acceleration [m/s/day]	40	23
ADVVAhbl*	Advective meridional acceleration [m/s/day]	40	23
CNVHRhbl*	Convective heating rate [K/day]	40	23
CNVMRhbl*	Convective moistening rate [kg/kg/day]	40	23
CNVUAhbl*	Convective zonal acceleration [m/s/day]	40	23
CNVVAhbl*	Convective meridional acceleration [m/s/day]	40	23
CWATHbl*	Cloud water content [kg/kg]	40	23
CWORKhbl*	Cloud work function [J/kg]	40	23
GWDUAhbl*	Gravity wave zonal acceleration [m/s/day]	40	23
GWDVAhbl*	Gravity wave meridional acceleration [m/s/day]	40	23
HGThbl*	Mean geopotential height [gpm]	40	23
LRGHRhbl*	Large scale condensation heating rate [K/day]	40	23
LRGMRhbl*	Large scale moistening rate [kg/kg/day]	40	23
LWHRhbl*	Longwave radiative heating rate [K/day]	40	23
MFLUXhbl*	Upward mass flux [kg/m ² /s]	40	23
MFLXBhbl*	Upward mass flux at cloud base [kg/m ² /s]	40	23
OZONEhbl	Ozone mixing ratio [ppmv]	40	23
PRESsfc	Surface pressure [Pa]	1	1
PRESMsfc*	Mean Surface pressure [Pa]	1	1
SPFHMhbl*	Mean specific humidity [kg/kg]	40	23
SWHRhbl*	Solar radiative heating rate [K/day]	40	23
TCDChbl*	Cloud cover [%]	40	23
TMPMhbl*	Mean temperature [K]	40	23
UGRDMhbl*	Mean zonal wind [m/s]	40	23
VDFHRhbl*	Vertical diffusion heating rate [K/day]	40	23
VDFMRhbl*	Vertical diffusion moistening rate [kg/kg/day]	40	23
VDFUAhbl*	Vertical diffusion zonal acceleration [m/s/day]	40	23
VDFVAhbl*	Vertical diffusion meridional acceleration [m/s/day]	40	23
VGRDMhbl*	Mean meridional wind [m/s]	40	23
VVELMhbl*	Mean pressure vertical velocity [Pa/s]	40	23
STDZhbl*	Standard deviation of geopotential height [gpm]	40	23
STDUhbl*	Standard deviation of zonal wind [m/s]	40	23

Table A4 (continued)

STDVhbl*	Standard deviation of meridional wind [m/s]	40	23
STDQhbl*	Standard deviation of specific humidity [kg/kg]	40	23
STDThbl*	Standard deviation of temperature [K]	40	23
CBUWhbl*	Covariance between zonal wind and vertical velocity [m/s*Pa/s]	40	23
CBVWhbl*	Covariance between meridional wind and vertical velocity [m/s*Pa/s]	40	23
CBUQhbl*	Covariance between zonal wind and specific humidity [m/s*gm/gm]	40	23
CBVQhbl*	Covariance between meridional wind and specific humidity [m/s*gm/gm]	40	23
CBTWhbl*	Covariance between temperature and vertical velocity [K*Pa/s]	40	23
CBQWhbl*	Covariance between specific humidity and vertical velocity [gm/gm*Pa/s]	40	23
CBUVhbl*	Covariance between zonal wind and meridional wind [m ² /s ²]	40	23
CBUTHbl*	Covariance between zonal wind and temperature [K*m/s]	40	23
CBVThbl*	Covariance between meridional wind and temperature [K*m/s]	40	23
STDWhbl*	Standard deviation of pressure vertical velocity [Pa/s]	40	23

o3tot_phy3m25

O3TOTcol	Total column ozone [DU]	1
----------	-------------------------	---

fest_phyland, fest_phyland25

TSCsfc*	Canopy temperature [K]	1
TSGsfc*	Ground temperature [K]	1
SoilTcol*	Soil temperature [K]	1
GFLXsfc*	Ground heat flux [W/m ²]	1
MSGsfc*	Moisture storage on ground/cover [m]	1
MSCsfc*	Moisture storage on canopy [m]	1
SoilWhbl*	Soil water content [mm]	1
LTRSsfc*	Evapotranspiration [W/m ²]	1
LINTsfc*	Interception loss [W/m ²]	1
ROFsfc*	Surface runoff [mm/day]	1

ges_p, ges_p25

HGTprs	Geopotential height [gpm]	23
TMPprs	Air temperature [K]	23
SPFHprs	Specific humidity [kg/kg]	12
UGRDprs	Zonal wind [m/s]	23
VGRDprs	Meridional wind [m/s]	23
VVELprs	Pressure vertical velocity [Pa/s]	23

Table A4 (continued)

CWATprs	Cloud water content [kg/kg]	12
PRMSLmsl	Pressure reduced to mean sea level [Pa]	1
TMPsfc	Surface (2 m) air temperature [K]	1
DEPRprs	Dew point depression [K]	8
DEPRsfc	Surface (2 m) dew point depression [K]	1
SPFHsfc	Surface (2 m) specific humidity [kg/kg]	1
UGRDsfc	Surface (10 m) zonal wind [m/s]	1
VGRDsfc	Surface (10 m) meridional wind [m/s]	1

ges_mdl		
HGThbl	Geopotential height [gpm]	40
TMP_hbl	Air temperature [K]	40
SPFH_hbl	Specific humidity [kg/kg]	40
RH_hbl	Relative humidity [fraction]	40
UGRD_hbl	Zonal wind [m/s]	40
VGRD_hbl	Meridional wind [m/s]	40
VVEL_hbl	Pressure vertical velocity [Pa/s]	40
CWATHbl	Cloud water content [kg/kg]	40
DISTsfc	Model surface height [m]	1
PRESsfc	Surface pressure [Pa]	1
PRMSLmsl	Pressure reduced to mean sea level [Pa]	1
TMPsfc	Surface (2 m) air temperature [K]	1
SPFHsfc	Surface (2 m) specific humidity [kg/kg]	1
RHsfc	Surface (2 m) relative humidity [fraction]	1
UGRDsfc	Surface (10 m) zonal wind [m/s]	1
VGRDsfc	Surface (10 m) meridional wind [m/s]	1

lfeg_topo.gr (Gaus)		
TOPO	Topography [m]	1

lfpl_topo.gr (LL25)		
TOPO	Topography [m]	1

Table A4 (continued)

typr.dat		
TYPE	Surface type index [integer] Land-sea mask for Gaussian grid	1
	Index	
	0	ocean
	1	evergreen broadleaf trees
	2	broadleaf deciduous trees
	3	broadleaf and needle leaf trees
	4	evergreen needle leaf trees
	5	deciduous needle leaf trees
	6	broadleaf trees with groundcover
	7	groundcover
	8	broadleaf shrubs with groundcover
	9	broadleaf shrubs with bare soil
	10	dwarf trees and shrubs
	11	bare soil
	12	cultivated land
	13	ice cap and glacier
mask25.jma_t106.gr (LL25)		
LS	Land-sea mask (land:1 sea:0)	1
soil.t106		
PRS	Soil porosity [0–1]	1
ZDP1	Surface soil layer [m]	1
ZDP2	Middle soil layer [m]	1
ZDP3	Deep soil layer [m]	1

Appendix B**Acronyms**

		ATOVS	Advanced TOVS
		CDAS	Climate Data Assimilation System
1D-Var	One-dimensional variational method	CLASS	Comprehensive Large Array-data Stewardship System
3D-Var	Three-dimensional variational method	CMAP	CPC Merged Analysis of Precipitation
AAPP	ATOVS and AVHRR processing package	COBE	Centennial in-situ Observation-Based Estimates of variability of SST and marine meteorological variables
AMI	Active Microwave Instrument		
AMSU	Advanced MSU		
AMV	Atmospheric Motion Vector	CPC	Climate Prediction Center

CRIEPI	Central Research Institute of Electric Power Industry	JMA	Japan Meteorological Agency
CRU	Climate Research Unit	JRA-25	Japanese 25-year Reanalysis
CTM	Chemical Transport Model	METEOSAT	Meteorological Satellite
DAO	Data Assimilation Office of NASA	MEXT	Ministry of Education and Technology
DOE	Department of Energy	MODIS	Moderate Resolution Imaging Spectroradiometer
DMSP	Defense Meteorological Satellite Program	MRI	Meteorological Research Institute of JMA
ECMWF	European Centre for Medium-Range Weather Forecast	MSC	Meteorological Satellite Center of JMA
ENSO	El Nino/Southern Oscillation	MSU	Microwave Sounding Unit
ERA-15	ECMWF 15-year Reanalysis	NASA	National Aeronautics and Space Administration
ERA-40	ECMWF 40-year Reanalysis	NCAR	National Center for Atmospheric Research
ERS	European Remote-sensing Satellite	NCDC	National Climate Data Center
ESA	European Space Agency	NCEP	National Center for Environmental Prediction
EUMETSAT	European Organisation for the Exploitation of Meteorological Satellites	NESDIS	National Environmental Satellite Data, and Information Service
FGGE	First GARP Global Experiment	NIMBUS	Project Name of Atmospheric Research Satellite of NASA/USA (not an abbreviation)
GAME	GEWEX Asia Monsoon Experiment	NOAA	National Oceanic and Atmospheric Administration
GARP	Global Atmospheric Research Program	OI	Optimal Interpolation
GCOS	Global Climate Observation System	OLR	Outgoing Long wave Radiation
GEOS	Goddard Earth Observing System	OSE	Observation System Experiment
GEWEX	Global Energy and Water Cycle Experiment	PCMDI/LLNL	Program for Climate Model Diagnosis and Intercomparison/Laurence Livermore National Laboratory
GMAO	Global Modeling and Assimilation Office of NASA	PW	Precipitable Water
GMS	Geostationary Meteorological Satellites of JMA	QBO	Quasi-Biennial Oscillation
GPCP	Global Precipitation Climatology Project	QC	Quality Control
GPV	Grid Point Value	QI	Quality Indicator
GSM	Global Spectral Model	RTTOV	The fast Radiative Transfer model for TOVS
GTS	Global Telecommunication System	RMSE	Root Mean Square Error
HIRS	High resolution Infrared Radiation Sounder	SAO	Semi-Annual Oscillation
IAU	Incremental Analysis Update	SiB	Simple Biosphere
ICODAS	International Comprehensive Ocean-Atmosphere Data Set	SPARC	Stratospheric Processes and their Role in Climate
IFOV	Instantaneous Field Of View	SSM/I	Special Sensor of Microwave Imager
ISCCP	International Satellite Cloud Climatology Project	SMMR	Scanning Multichannel Microwave Radiometer
ITCZ	InterTropical Convergence Zone	SST	Sea Surface Temperature
JCDAS	JMA Climate Data Assimilation System	SSU	Stratospheric Sounding Unit
		SSW	Stratospheric Sudden Warming

SYNOP	surface SYNOptic observations (data format)
TBB	Black Body Temperature
TCR	Wind profile retrievals surrounding tropical cyclones
TIROS	Television and InfraRed Observation Satellite
TOVS	TIROS Operational Vertical Sounder
UKMO	United Kingdom Meteorological Office
USGS	United States Geological Survey
WARM	Water and Atmospheric Resources Monitoring Program

References

- Adler, R.F., G.J. Huffman, A. Chang, R. Ferraro, P. Xie, J. Janowiak, B. Rudolf, U. Schneider, S. Curtis, D. Bolvin, A. Gruber, J. Susskind, and P. Arkin, 2003: The Version 2 Global Precipitation Climatology Project (GPCP) Monthly Precipitation Analysis (1979-Present). *J. Hydrometeorol.*, **4**, 1147–1167.
- Andrae, U., N. Sokka, and K. Onogi, 2004: The radiosonde temperature bias corrections used in ERA-40. ECMWF ERA-40 Project Report Series, **15**, 34 pp.
- Aonashi, K., K. Kuma, and Y. Matsushita, 1997: A Physical Initialization Method for the Economical Prognostic Arakawa-Schubert Scheme. *J. Meteor. Soc. Japan*, **75**, 597–617.
- Arakawa, A. and W.H. Schubert, 1974: Interaction of a cumulus cloud ensemble with the large-scale environment, Part I. *J. Atmos. Sci.*, **31**, 674–701.
- Asselin, R., 1972: Frequency filter for time integrations. *Mon. Wea. Rev.*, **100**, 487–490.
- Basist, A.N. and M. Chelliah, 1997: Comparison of tropospheric temperatures derived from the NCEP/NCAR reanalysis, NCEP operational analysis, and the Microwave Sounding Unit. *Bull. Amer. Meteor. Soc.*, **78**, 1431–1447.
- Beljaars, A.C.M., 1995: The parameterization of surface fluxes in large-scale models under free convection. *Quart. J. Roy. Meteor. Soc.*, **121**, 255–270.
- Bengtsson, L. and J. Shukla, 1988: Integration of space and in situ observations to study global climate change. *Bull. Amer. Meteor. Soc.*, **69**, 1130–1143.
- Bengtsson, L., K.I. Hodges, and S. Hagemann, 2004a: Sensitivity of large-scale atmospheric analyses to humidity observations and its impact on the global water cycle and tropical and extratropical weather systems in ERA40. *Tellus*, **56A**, 202–217.
- Bengtsson, L., K.I. Hodges, and S. Hagemann, 2004b: Sensitivity of re-analyses to the observing system: Determination of the global atmospheric circulation from reduced observations. *Tellus*, **56A**, 456–471.
- Bengtsson, L., S. Hagemann, and K.I. Hodges, 2004c: Can climate trends be calculated from reanalysis data? *J. Geophys. Res.*, **109**, D11111, doi:10.1029/2004JD004536.
- Betts, A.K. and P. Viterbo, 2004: Land-surface, boundary layer and cloud-field coupling over the south-western Amazon in ERA-40. ECMWF ERA-40 Project Report Series, **25**, 22 pp.
- Betts, A.K., J.H. Ball, P. Viterbo, A. Dai, and J. Marengo, 2005: Hydrometeorology of the Amazon in ERA-40. *J. Hydrometeorology*, **6**, 764–774.
- Briegleb, B.P., 1992: Delta Eddington Approximation for Solar Radiation in the NCAR Community Climate Model. *J. Geophys. Res.*, **97**, 7603–7612.
- Cavalieri, D.J., P. Gloersen, and W.J. Campbell, 1984: Determination of Sea Ice Parameters from NIMBUS-7 SMMR. *J. Geophys. Res.*, **89**, 5355–5369.
- Cavalieri, D.J., C.L. Parkinson, P. Gloersen, J.C. Comiso, and H.J. Zwally, 1999: Deriving long-term time series of sea ice cover from satellite passive microwave multisensor data sets. *J. Geophys. Res.*, **104**, 15,803–15,814.
- Charnock, H., 1955: Wind stress on a water surface. *Quart. J. Roy. Meteor. Soc.*, **81**, 639–640.
- Christy, J.R., R.W. Spencer, W.B. Norris, W.D. Braswell, and D.E. Parker, 2003: Error estimates of version 5.0 of MSU-AMSU bulk atmospheric temperatures. *J. Atmos. Oceanic Technol.*, **20**, 613–629.
- Coakley, J.A., R.D. Cess, and F.B. Yurevich, 1983: The effect of tropospheric aerosols on the earth's radiation budget: a parameterization for climate models. *J. Atmos. Sci.*, **40**, 116–138.
- Courtier, P., J.-N. Thepaut, and A. Hollingworth, 1994: A strategy for operational implementation of 4D-Var, using an incremental approach. *Quart. J. Roy. Meteor. Soc.*, **120**, 1367–1388.
- Darnell, W.L., W.F. Staylor, S.K. Gupta, and F.M. Denn, 1988: Estimation of surface insolation using Sun-synchronous satellite data. *J. Climate*, **1**, 820–835.
- Dee, D.P., 2005: Bias and data assimilation. *Quart. J. Roy. Meteor. Soc.*, **131**, 3323–3344.
- Dorman, J. and P.J. Sellers, 1989: A global climatology of albedo, roughness length and stomatal resistances for atmospheric general circulation models as represented by the Simple Biosphere model (SiB). *J. Appl. Meteor.*, **28**, 833–855.

- Doty, B.E. and J.L. Kinter III, 1995: Geophysical Data Analysis and Visualization using GrADS. *Visualization Techniques in Space and Atmospheric Sciences*, eds. E.P. Szuszcwicz and J.H. Bredekamp, NASA, Washington, D.C., 209–219.
- Fiorino, M., 2002: Analysis and forecasts of tropical cyclones in the ECMWF 40-year reanalysis (ERA-40). Extended abstract of 25th Conference on Hurricanes and Tropical Meteorology, 261–264.
- Fujita, T., 2004: Revision of the Background Error Covariance in the Global 3D-Var. WMO CAS/JSC WGNE Research Activities in Atmospheric and Oceanic Modelling, [4–11].
- Gibson, J.K., P. Källberg, S. Uppala, A. Hernandez, A. Nomura, and E. Serrano, 1997: ERA Description. *ECMWF ERA-15 Project Report Series*, **1**, 71 pp.
- Hagemann, S., K. Arpe, and L. Bengtsson, 2005: Validation of the hydrological cycle of ERA-40. *ERA-40 Project Report Series*, **24**, 42 pp.
- Haimberger, L., 2005: Homogenization of radiosonde temperature time series using ERA-40 analysis feedback information. *ECMWF ERA-40 Project Report Series*, **23**, 68 pp.
- Haimberger, L., 2006: Homogenization of radiosonde temperature time series using innovation statistics. *J. Climate*, **20**, 1377–1403.
- Hatsushika, H., J. Tsutsui, M. Fiorino, and K. Onogi, 2006: Impact of Wind Profile Retrievals on the Analysis of Tropical Cyclones in the JRA-25 Reanalysis. *J. Meteor. Soc. Japan*, **84**, 891–905.
- Hawkins, F.H. and D.T. Rubsam, 1968: Hurricane Hilda, 1964 II. Structure and Budgets of the Hurricane on October 1, 1964. *Mon. Wea. Rev.*, **96**, 617–636.
- Hollinger, J.P., G.A. Poe, L.A. Rose, R.H. Baldwin, J.W. Deaver, D.K. Conway, R.W. Conway, M.A. Craft, N.L. Leist, E.M. Overton, D.J. Spangler, L.A. Walker, J.L. Peirce, R.C. Savage, J.C. Alishouse, J.C. Wilkerson, S. Snyder, J. Vongsathorn, R. Ferraro, C.T. Swift, M. Goodberlet, K.H. Hsueh, F. Wentz, M.J. McFarland, M. Batchelor, Robert Miller, J. Miller, Richard Miller, S. Steinberg, C.M.U. Neale, R.O. Ramseier, K. Asmus, and I.G. Rubinstein, 1989, 1991: DMSP Special Sensor Microwave/Imager, Calibration/Validation. Final Report. Vol. 1 (1989), Vol. 2 (1991), Naval Research Laboratory.
- Hollinger, S.E. and S.A. Isard, 1994: A soil moisture climatology of Illinois. *J. Climate*, **7**, 822–833.
- Holmlund, K., 1998: the utilization of statistical properties of satellite-derived atmospheric motion vectors to derive quality indicators. *Weather and Forecasting*, **13**, 1093–1104.
- Ishii, M., A. Shouji, S. Sugimoto, and T. Matsumoto, 2005: Objective Analyses of Sea-Surface Temperature and Marine Meteorological Variables for the 20th Century Using ICOADS and the KOBE Collection. *Intl. J. Climatol.*, **25**, 865–879.
- Iwasaki, T., S. Yamada, and K. Tada, 1989a: A parameterization scheme of orographic gravity wave drag with the different vertical partitionings, Part I: Impact on medium range forecasts. *J. Meteor. Soc. Japan*, **67**, 11–27.
- Iwasaki, T., S. Yamada, and K. Tada, 1989b: A parameterization scheme of orographic gravity wave drag with the different vertical partitionings, Part II: Zonally averaged budget analyses based on transformed Eulerian-mean method. *J. Meteor. Soc. Japan*, **67**, 29–41.
- Japan Meteorological Agency, 2002: Outline of the operational numerical weather prediction at the Japan Meteorological Agency. Appendix to WMO Numerical Weather Prediction Progress Report, 158 pp.
- Jarraud, M., C. Girard, and J.F. Geleyn, 1982: Note on a possible linearization of the vorticity equation in a primitive spectral model. Research Activities in Atmospheric and Ocean Modelling. Rep. No. 3.
- Jones, P.D. and A. Moberg, 2003: Hemispheric and large-scale surface air temperature variations: An extensive revision and update to 2001. *J. Climate*, **16**, 206–223.
- Joseph, J.H., W.J. Wiscombe, and J.A. Weinman, 1976: The delta-Eddington approximation for radiative flux transfer. *J. Atmos. Sci.*, **33**, 2452–2459.
- Kalnay, E., M. Kanamitsu, R. Kistler, W. Collins, D. Deaven, L. Gandin, M. Iredell, S. Saha, G. White, J. Woollen, Y. Zhu, M. Chelliah, W. Ebisuzaki, W. Higgins, J. Janowiak, K.C. Mo, C. Ropelewski, J. Wang, A. Leetmaa, R. Reynolds, R. Jenne, and D. Joseph 1996: The NCEP/NCAR 40-year reanalysis project. *Bull. Amer. Meteor. Soc.*, **77**, 437–471.
- Kanamitsu, M., W. Ebisuzaki, J. Woollen, S.-K. Yang, J.J. Hnilo, M. Fiorino, and G.L. Potter, 2002: NCEP-DOE AMIP-II Reanalysis (R-2). *Bull. Amer. Meteor. Soc.*, **83**, 1631–1643.
- Kawai, H. and T. Inoue, 2006: A simple parameterization scheme for subtropical marine stratocumulus. *SOLA*, **2**, 17–20.
- Kawai, H., 2003: Impact of a Cloud Ice Fall Scheme Based on an Analytically Integrated Solution. WMO CAS/JSC WGNE Research Activities in Atmospheric and Oceanic Modelling, [4–11].
- Kazumori, M., K. Fukuda, and H. Owada, 2005: Assimilation of ATOVS level-1c radiance at JMA. WMO CAS/JSC WGNE Research Activ-

- ities in Atmospheric and Oceanic Modelling, [1–21].
- Kazumori, M. and Y. Nakamura, 2005: MODIS polar winds assimilation at JMA. WMO CAS/JSC WGNE Research Activities in Atmospheric and Oceanic Modelling, [1–23].
- Kistler, R., E. Kalnay, W. Collins, S. Saha, G. White, J. Woollen, M. Chelliah, W. Ebisuzaki, M. Kanamitsu, V. Kousky, H. van den Dool, R. Jenne, and M. Fiorino, 2001: The NCEP-NCAR 50-year reanalysis: Monthly means CD-Rom and documentation. *Bull. Amer. Meteor. Soc.*, **82**, 247–267.
- Koide, H., K. Onogi, T. Yasunari, K. Masuda, W. Ohfuchi, R. Krishnan, A. Yatagai, H. Kanamaru, 2000: Report on the Second International Conference on Reanalysis. *Tenki*, **47**, 267–276 (in Japanese).
- Komura, K. and T. Uwai, 1992: The collection of historical ships' data in Kobe Marine Observatory. *Bulletin of Kobe Marine Observatory*, **211**, 19–30.
- Kumabe, R., 2004: Renewal of Operational AMV Extraction System in JMA. Seventh International Winds Workshop, Session I: Current Systems to Derive Atmospheric Motion Vectors (AMVs). June 14–17, 2004, hosted by EUMETSAT.
- Kurino, T., 2001a: A Statistical Approach to Passive Microwave Snow Depth Retrieval. The 4th International GEWEX conference, Institute Pierre Simon Laplace, Collège de France.
- Kurino, T., 2001b: Development of an algorithm of retrieving snow depth from microwave radiances and use for JMA operational seasonal forecast. JMA seasonal forecast textbook 2001, 27–34 (in Japanese).
- Limpasuvan, V., D.W. Thompson, and D.L. Hartmann, 2004: The life cycle of the northern hemisphere sudden stratospheric warmings. *J. Climate*, **17**, 2584–2596.
- Liu, D.C. and J. Nocedal, 1989: On the limited memory BFGS method for large scale optimization. *Math. Programming*, **45**, 503–528.
- Manabe, T., 1999: The digitized Kobe Collection, phase I; historical surface marine meteorological observations in the archive of the Japan Meteorological Agency. *Bull. Amer. Meteor. Soc.*, **80**, 2703–2715.
- Matsumoto, T.M., Ishii, Y. Fukuda, and S. Hirahara, 2006: Sea Ice Data Derived from Microwave Radiometer for Climate Monitoring. 14th Conference on Satellite Meteorology and Oceanography, AMS 14th Conference on Satellite Meteorology and Oceanography, P2.21.
- Matsuno, T., 1971: A dynamical model of the stratospheric sudden warming. *J. Atmos. Sci.*, **28**, 1479–1494.
- McMillin, L.M. and C. Dean, 1982: Evaluation of a New Operational Technique for Producing Clear Radiances. *J. Appl. Meteor.*, **21**, 1005–1014.
- Mears, C.A., M.C. Schabel, and F.J. Wentz, 2003: A reanalysis of the MSU channel 2 tropospheric temperature record. *J. Climate*, **16**, 3650–3664.
- Mellor, G.L. and T. Yamada, 1982: Development of a turbulence closure model for geophysical fluid problems. *Rev. Geophys. Space Phys.*, **20**, 851–875.
- Moorthi, S. and M.J. Suarez, 1992: Relaxed Arakawa-Schubert: A parameterization of moist convection for general circulation models. *Mon. Wea. Rev.* **120**, 978–1002.
- Murai, S., S. Yabu, and H. Kitagawa, 2005: Development of a new radiation scheme for the global atmospheric NWP model. Proceeding of 21st Conference on Weather Analysis and Forecasting/17th Conference on Numerical Weather Prediction, Aug 1–5, 2005, P1.66.
- Nakagawa, M. and A. Shimpo, 2004: Development of a Cumulus Parameterization Scheme for the Operational Global Model at JMA. RSMC Tokyo-Typhoon Center Technical Review, **7**, 10–15.
- Neumann, C.J., 1993: Global overview. Global guide to tropical cyclone forecasting, G.J. Holland, Ed., chapter 1, World Meteorological Organization, Rep. TCP-31, WMO/TD-560, Geneva, Switzerland.
- Newman, M., P.D. Sardeshmukh, and J.W. Bergman, 2000: An assessment of the NCEP, NASA, and ECMWF reanalyses over the tropical west Pacific warm pool. *Bull. Amer. Meteor. Soc.*, **81**, 41–48.
- Nomura, A. and Y. Tahara, 1997: The use of wind scatterometer data in operational data assimilation at JMA. CAS/JSC WGNE Research Activities in Atmospheric and Oceanic Modelling, **25**, 1.49.
- Okamoto, K., M. Kazumori, and H. Owada, 2005: The Assimilation of ATOVS Radiances in the JMA Global Analysis System. *J. Meteor. Soc. Japan*, **83**, 201–217.
- Okamoto, N., M.D. Yamanaka, S.-Y. Ogino, H. Hashiguchi, N. Nishi, T. Sribimawati, and A. Numaguti, 2003: Seasonal variation of tropospheric wind over Indonesia: Comparison between collected operational rawinsonde data and NCEP reanalysis for 1992–99. *J. Meteor. Soc. Japan*, **81**, 829–850.
- Onogi, K., 1998: A Data Quality Control Method Using Forecasted Horizontal Gradient and Tendency in a NWP System: Dynamic QC. *J. Meteor. Soc. Japan*, **76**, 497–516.

- Onogi, K., 2000: The long-term performance of the radiosonde observing system to be used in ERA-40. *ECMWF ERA-40 Project Report Series*, **2**, 77 pp.
- Onogi, K., H. Koide, M. Sakamoto, S. Kobayashi, J. Tsutsui, H. Hatsushika, T. Matsumoto, N. Yamazaki, H. Kamahori, K. Takahashi, K. Kato, T. Ose, S. Kadokura, and K. Wada, 2005: JRA-25; Japanese 25-year Reanalysis—progress and status—. *Quart. J. Roy. Meteor. Soc.*, **131**, 3259–3268.
- Oyama, R., 2007: Characteristics and effectiveness of Atmospheric Motion Vector product (AMV) in Japanese long-term Reanalysis project (JRA-25). Meteorological Satellite Center technical note, **48**, Meteorological Satellite Center of Japan Meteorological Agency, 1–36.
- Palmer, T.N., G.J. Shutts, and R. Swinbank, 1986: Alleviation of a systematic westerly bias in general circulation and numerical weather prediction models through an orographic gravity wave drag parametrization. *Quart. J. Roy. Meteor. Soc.*, **112**, 1001–1039.
- Parrish, D. and J. Derber, 1992: The National Meteorological Center's spectral statistical interpolation analysis system. *Mon. Wea. Rev.*, **120**, 1747–1763.
- Rattenborg, M., 1998: Status and development of operational METEOSAT wind products. Proc. of 'Fourth International Wind Workshop,' EU-METSAT, 49–59.
- Randall, D. and D.-M. Pan, 1993: Implementation of the Arakawa-Schubert cumulus parameterization with a prognostic closure. Meteorological Monograph/The representation of cumulus convection in numerical models. *J. Atmos. Sci.*, **46**, 137–144.
- Rayner, N.A., D.E. Parker, E.B. Horton, C.K. Folland, L.V. Alexander, D.P. Rowell, E.C. Kent, and A. Kaplan, 2003: Global analyses of sea surface temperature, sea ice, and night marine air temperature since the late nineteenth century. *J. Geophys. Res.*, **108**(D14): 4407. doi:10.1029/2002JD002670.
- Robinson, D., K. Dewey, and R. Heim, 1993: Global snow cover monitoring: an update. *Bull. Amer. Meteor. Soc.*, **74**(9), 1689–1696.
- Rossow, W.B., A.W. Walker, D.E. Beusichel, and M.D. Roiter, 1996: International Satellite Cloud Climatology Project (ISCCP) Documentation of New Cloud Datasets. WMO/TD-No. **737**, World Meteorological Organization, 115 pp.
- Sakamoto, M., S. Kobayashi, K. Kato, T. Matsumoto, H. Koide, K. Onogi, T. Ose, and H. Hatsushika, 2005: Ongoing Japanese Long-term Reanalysis Project (JRA-25); Assimilation of NOAA Polar-orbiter Satellite Sounder Data. Proceeding of the 85th American Meteorological Society annual meeting, Ninth Symposium on Integrated Observing and Assimilation Systems for Atmosphere, Oceans, and Land Surface, Jan 8–14, 2005, P1.10.
- Sakamoto, M., K. Okamoto, and Y. Yoshizaki, 2006: A follow-up study of the TOVS application for the Japanese Climatic Reanalysis: JRA-25. Proceeding of ITSC-15, Oct. 4–10, 2006, Maratea, Italy.
- Santer, B.D., T.M.L. Wigley, A.J. Simmons, P.W. Källberg, G.A. Kelly, S.M. Uppala, C. Ammann, J.S. Boyle, W. Bruggemann, C. Doutriaux, M. Fiorino, C. Mears, G.A. Meehl, R. Sausen, K.E. Taylor, W.M. Washington, M.F. Wehner, and F.J. Wentz, 2004: Identification of anthropogenic climate change using a second-generation reanalysis. *J. Geophys. Res.*, **109**, D21104, doi:10.1029/2004JD005075.
- Santer, B.D., T.M.L. Wigley, C. Mears, F.J. Wentz, S.A. Klein, D.J. Seidel, K.E. Taylor, P.W. Thorne, M.F. Wehner, P.J. Gleckler, J.S. Boyle, W.D. Collins, K.W. Dixon, C. Doutriaux, M. Free, Q. Fu, J.E. Hansen, G.S. Jones, R. Ruedy, T.R. Karl, J.R. Lanzante, G.A. Meehl, V. Ramaswamy, G. Russell, and G.A. Schmidt, 2005: Amplification of surface temperature trends and variability in the tropical atmosphere. *Science*, **309**, 1551–1556.
- Sato, N., P. J. Sellers, D.A. Randall, E.K. Schneider, J. Shukla, J.L. Kinter III, Y.-T. Hou, and E. Albertazzi, 1989: Effects of implementing the simple biosphere model (SiB) in a general circulation model. *J. Atmos. Sci.*, **46**, 2757–2782.
- Saunders, R.W., M. Matricardi, and P. Brunel, 1999: An improved fast radiative transfer model for assimilation of satellite radiance observations. *Quart. J. Roy. Meteor. Soc.*, **125**, 1407–1425.
- Saunders, R.W., 2000: RTTOV-6 Science and Validation Report. <http://www.metoffice.com/research/interproj/nwpsaf/rtm/d81svr.pdf>
- Saunders, R.W., 2002: RTTOV-7 Science and Validation Report. http://www.metoffice.com/research/interproj/nwpsaf/rtm/rttov7_svr.html
- Schubert, S.D., R. Rood, and J. Pfaendner, 1993: An assimilated data set for earth sciences applications. *Bull. Amer. Meteor. Soc.*, **74**, 2331–2342.
- Sellers, P.J., Y. Mintz, Y.C. Sud, and A. Dalcher, 1986: A simple biosphere model (SiB) for use within general circulation models. *J. Atmos. Sci.*, **43**, 505–531.
- Shibata, K., M. Deushi, T.T. Sekiyama, and H. Yoshimura, 2005: Development of an MRI chemical transport model for the study of strato-

- spheric chemistry. *Papers in Meteorology and Geophysics*, **55**, 75–119.
- Simmons, A.J. and D.M. Burridge, 1981: An energy and angular momentum conserving vertical finite difference scheme and hybrid vertical coordinates. *Mon. Wea. Rev.*, **109**, 758–766.
- Simmons, A.J., P.D. Jones, V. da Costa Bechtold, A.C.M. Beljaars, P.W. Kållberg, S. Saarinen, S.M. Uppala, P. Viterbo, and N. Wedi, 2004: Comparison of trends and low-frequency variability in CRU, ERA-40, and NCEP/NCAR analyses of surface air temperature. *J. Geophys. Res.*, **109**, D24115, doi:10.1029/2004JD005306.
- SPARC, 2002: SPARC Intercomparison of Middle Atmosphere Climatologies. SPARC Report No. 3, Edited by W. Randel, M.-L. Chanin and C. Michaut, 96 pp.
- Sugi, M., K. Kuma, K. Tada, K. Tamiya, N. Hasegawa, T. Iwasaki, S. Yamada, and T. Kitade, 1990: Description and performance of the JMA operational global spectral model (JMA GSM88). *Geophys. Mag.*, **43**, 105–130.
- Sundqvist, H., 1988: Parameterization of condensation and associated clouds in models for weather prediction and general circulation simulation. *Physically-Based Modelling and Simulation of Climate and Climatic Change*, M.E. Schlesinger, Ed., Reidel, 433–461.
- Tada, H., 2000: Atmospheric Analysis. Numerical Prediction Division Report No. **47**, 13–16, Forecast Department, Japan Meteorological Agency (in Japanese).
- Takahashi, K., N. Yamazaki, and H. Kamahori, 2006: Trends of Heavy Precipitation Events in Global Observation and Reanalysis Datasets. *SOLA*, **2**, 96–99.
- Takeuchi, Y., 2002: Algorithm theoretical basis document (ATBD) of the algorithm to derive total water vapor content from ADEOS-II AMSR. *EORC Bull.*, **9**, 3–7.
- Takeuchi, Y. and T. Tsuyuki, 2002: The operational 3D-Var assimilation system of JMA for the Global Spectrum Model and the Typhoon Model. CAS/JSC WGNE Research Activities in Atmospheric and Oceanic Modelling, **32**, 0159–0160.
- Tauchi, T., Y. Takeuchi, and Y. Sato, 2004: Assimilation of SSM/I and TMI total column precipitable water data into the JMA global 3D-Var assimilation system. CAS/JSC WGNE Research Activities in Atmospheric and Oceanic Modelling, **34**, 0135–0136.
- Teixeira, J. and T.F. Hogan, 2002: Boundary layer clouds in a global atmospheric model: simple cloud cover parameterizations. *J. Climate*, **15**, 1261–1276.
- Trenberth, K. and J. Olson, 1988: An evaluation and intercomparison of global analyses from the National Meteorological Center and the European Centre for Medium Range Weather Forecasts. *Bull. Amer. Meteor. Soc.*, **69**, 1047–1057.
- Tokuhiro, T., 2002: Validation of Land Surface Parameters from the JMA-SIB using ERA15 Atmospheric Forcing Data. Proceeding of the 27th Annual Climate Diagnostics and Prediction Workshop, October 21–25, 2002, hosted by George Mason University and COLA, 2 pp.
- Uppala, S.M., P.W. Kållberg, A.J. Simmons, U. Andrae, V. da Costa Bechtold, M. Fiorino, J.K. Gibson, J. Haseler, A. Hernandez, G.A. Kelly, X. Li, K. Onogi, S. Saarinen, N. Sokka, R.P. Allan, E. Andersson, K. Arpe, M.A. Balmaseda, A.C.M. Beljaars, L. van de Berg, J. Bidlot, N. Bormann, S. Caires, F. Chevallier, A. Dethof, M. Dragosavac, M. Fisher, M. Fuentes, S. Hagemann, E. Hólm, B.J. Hoskins, L. Isaksen, P.A.E.M. Janssen, R. Jenne, A.P. McNally, J.-F. Mahfouf, J.-J. Morcrette, N.A. Rayner, R.W. Saunders, P. Simon, A. Sterl, K.E. Trenberth, A. Untch, D. Vasiljevic, P. Viterbo, and J. Woollen, 2005: The ERA-40 re-analysis. *Quart. J. Roy. Meteor. Soc.*, **131**, 2961–3012.
- Uppala, S., P. Kållberg, A. Hernandez, S. Saarinen, M. Fiorino, X. Li, K. Onogi, N. Sokka, U. Andrae, and V. da Costa Bechtold, 2004: ERA-40: ECMWF 45-year reanalysis of the global atmosphere and surface conditions 1957–2002. *ECMWF Newsletter*, **101**, 2–21.
- van Noije, T.P.C. van, H.J. Eskes, M. van Weele, and P.F.J. van Velthoven, 2004: Implications of the enhanced Brewer-Dobson circulation in ERA-40 for the stratosphere-troposphere exchange of ozone in global chemistry-transport models. *J. Geophys. Res.*, **109**, D19308, doi:10.1029/2004JD004586.
- Wang, B. and Z. Fan, 1999: Choice of South Asian summer monsoon indices. *Bull. Amer. Meteor. Soc.*, **80**, 629–638.
- Wentz, F.J., 1991: User's Manual SSM/I Antenna Temperature Tapes Revision 1. RSS Technical Report 120191, Dec. 1, 1991, Remote Sensing System, Santa Rosa.
- Wentz, F.J., 1993: User's Manual SSM/I Antenna Temperature Tapes Revision 1. RSS Technical Report 120193, Dec. 1, 1993, Remote Sensing System, Santa Rosa.
- Werbowetzki, A. 1981: Atmospheric Sounding User's Guide. *NOAA Technical Report NESS*, **83**, April 1981.
- Woodruff, S.D., H.F. Diaz, J.D. Elms, and S.J. Worley, 1998: COADS Release 2 Data and

Metadata Enhancements for Improvements of Marine Surface Flux Fields. *Physics and Chemistry of the Earth*, **23**, 517–526.

Xie, P. and P.A. Arkin, 1997: Global Precipitation: A

17-year monthly analysis based on gauge observations, satellite estimates, and numerical model outputs. *Bull. Amer. Meteor. Soc.*, **78**, 2539–2558.